A preliminary investigation into the growth of the Sisters scoria cone complex, Ascension Island.

WINSTANLEY, REBECCA

A Preliminary Investigation into the Growth of the Sisters Scoria Cone Complex, Ascension Island.

Rebecca Winstanley

MSc by Research (Volcanology)

Department of Earth Sciences

University of Durham

2020

Durham University

Earth Sciences

Ascension Island, located in the South Atlantic Ocean, is an active ocean island volcano and a British Overseas Territory with strategically important UK and USA military infrastructure. The most recent eruption occurred from the Sisters scoria cone complex (SSCC) in the north of the island, which is composed of at least 4 scoria cones, tephra fall deposits and lavas. Here I present a textural study of the Unit 3 tephra fall deposit from two locations, as well as tephra dispersal analysis. Petrographic analysis of a further three tephra fall deposits and nine lava samples from the Sisters scoria cone complex was also undertaken in an attempt to correlate the lava flows and tephra falls. Three distinct types of pyroclasts were identified: type 1, which are equant and platy shaped with a dull, wrinkly skin that is adhered with ash fragments, lithic clasts, Pele's hair, spherical lava droplets and mineral precipitates. Their interiors are moderately-highly vesicular with a moderate microlite content; type 2, which are elongate and fluidal shaped with a black, glassy skin. Their interiors range from poorly-highly vesicular with a moderate microlite content; type 3, which range from elongate and fluidal to equant and sub-angular with a golden brown, glassy skin. Their interiors are highly vesicular with a poor microlite content. The Unit 3 eruption began with locally dispersed Hawaiian lava fountaining, before transitioning to Strombolian explosions that were more widely dispersed. As the eruption continued Strombolian explosions became dominant. Towards the end of the eruption, the magma came into contact with a limited volume of groundwater, which led to a series of small-scale, weak phreatomagmatic explosions, separated by magmatic phases. The Unit 3 eruption covered >24 km^2 of the island and a similar eruption in the future would have a 50% chance of ash accumulation up to 2.5 cm (10 kg/m^2) thick over Georgetown. The other eruptions that contributed to the Sisters scoria cone complex are inferred to have been broadly similar to that which produced Unit 3.

Table of Contents

List of Tables

List of Figures

Statement of Copyright

Acknowledgments

I would like to thank my supervisors Dr Rich Brown, Dr Kate Dobson and Dr Charlotte Vye-Brown for all their support and wisdom during the undertaking of the project. I would also like to thank Dr Julia Crummy for allowing me to work with her on tephra dispersal modelling at the British Geological Survey and Mr Leon Bowen for his guidance on the SEM. Further thanks go to Dr Ed Llewellin for creating the volume of the cone MATLAB script and all in the Durham University Volcanology group and the Ascension Island Volcanology group for lots of useful discussion around the project. Final thanks go to my friends who have provided entertainment and fun throughout the past academic year.

1. Introduction

The aim of this study is to provide a preliminary interpretation of recent basaltic volcanic activity at SSCC, Ascension Island, and to investigate eruption styles, attempt to correlate lava flows and to understand the growth of the complex. The specific objectives associated with the project include:

- Develop an understanding of the growth of the Sisters scoria cone complex (SSCC).
- Reconstruct a recent eruption from the volcano using grainsize, pyroclast textures and componentry studies of its tephra fall deposit.
- Reconstruct the dispersal of tephra and estimate key eruption parameters to aid in the development of volcanic hazard assessment on the island.

The tephra deposits were texturally characterised based on surface features, vesicularity and crystallinity and then imaged under the petrological microscope and the scanning electron microscope. Petrographic analysis was also carried out on the lava flows and separate tephra units in order to help correlate the deposits. Tephra dispersal was investigated by using field data, mathematical methods and the modelling software TephraProb (Biass et al, 2016) and Tephra2 (Connor and Connor, 2016), in order to create tephra dispersal maps for the eruptions.

Very little work has been undertaken on the products of the SSCC, and tephra dispersal maps for the island have never been published. Therefore, the results of this study will contribute to the wider study on the eruptions and hazards from basaltic eruptions on Ascension Island and aid in the development of volcanic hazard assessments.

2. Background

2.1 Ascension Island

The island is located in the South Atlantic Ocean, 100 km west of the Mid-Atlantic Ridge (MAR) **(figure 2.1)** and 50 km south of the Ascension Fracture Zone (AFZ). The island covers 93km^2, but the base, at 3000 m below sea level, covers >2000km^2 (Brozena, 1986). The visible part of the island is ~1% of the area of the entire edifice (Hobson, 2001), and the highest point on the island, Green Mountain, is 859 m asl (Jicha et al, 2013; Chamberlain et al, 2016). Ascension Island has been undergoing subsidence since ~2.5 Ma at a rate of 0.3 km/Myr and has a growth rate of 0.4 km/Myr since ~3.4 Ma, implying that the volcanic edifice is older than what is suggested by the surface samples (Minshull et al, 2010).

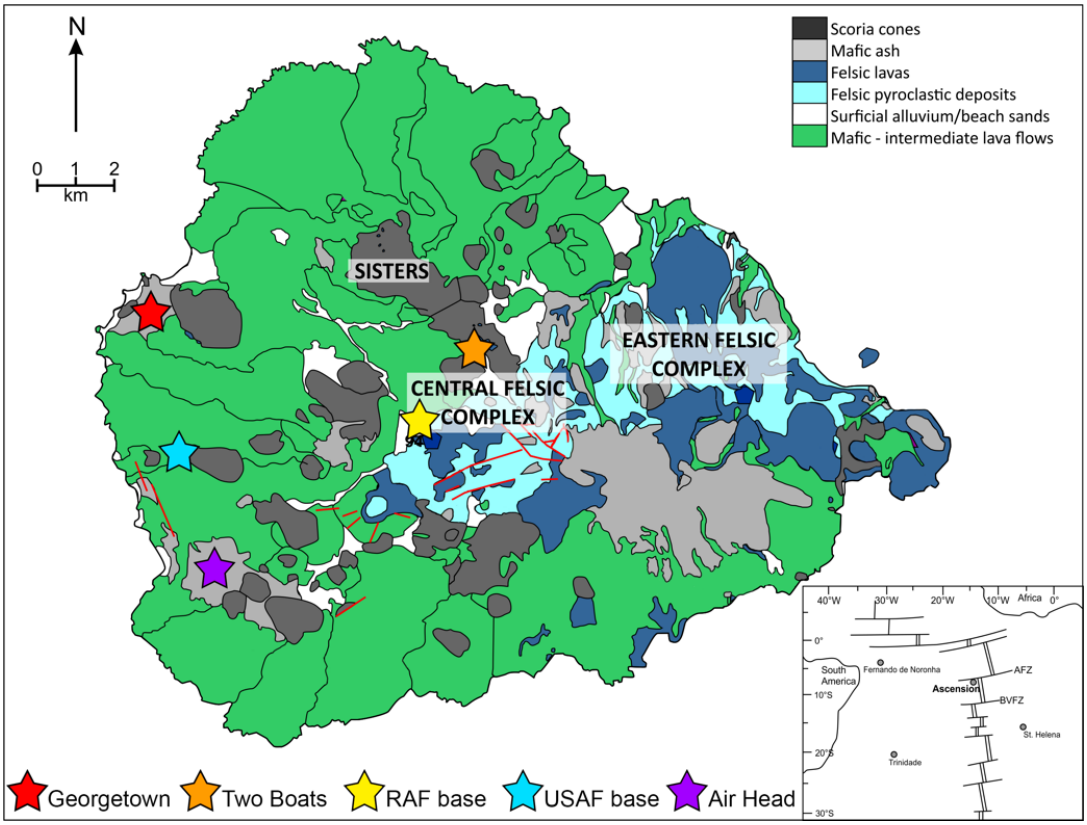

Figure 2.1: *Geological map of Ascension Island. The SSCC is identified and key localities are marked. The inset shows the location of Ascension Island relative to the MAR. (Modified from Chamberlain et al, 2016).*

The maximum crustal thickness under Ascension is 13 km (Klingelhofer et al, 2001) and there is an area of anomalous high velocity within the mid-crustal region, which is inferred to be the crystallised remains of a relict magma chamber (Chamberlain et al, 2019).

There are four principle fault orientations on the island: northwest, northeast, north-south and east-west (Nielson and Sibbett, 1996). The faults developed from uplift, caused by the intrusion of melt beneath the island and are one of the main controls on the location of eruptions (Nielson and Sibbett, 1996).

The origin of the magmatic source for Ascension is heavily debated. The island is aligned with two unnamed seamounts, which are parallel and west of the AFZ but do not demonstrate consistency with a fixed hotspot plume track (Ammon et al, 2009).

Two competing models have been proposed to explain the presence of magma under Ascension Island. The first suggests that the drift of the Mid-Atlantic Ridge axis away from the Ascension plume led to an asthenospheric flow towards the westward migrating ridge axis (Schilling et al, 1985). However, if this model is correct there is no plume directly under the Ascension Island. Evidence for this model comes from the chemistry of the basalts, where the Pb isotope variations in MORB's indicate the plume is located under the Circe Seamount (Jicha et al, 2013). The second model suggests that Ascension Island is the product of a flow of hot material, originating from an off-axis plume and moving towards the spreading axis and ridge crest of the AFZ (Brozena, 1986). In this model, the older and thicker lithosphere acts as barrier and diverts the flow, leading to the formation of the two seamounts and plate movement over a fixed hotspot does not occur.

Isotopic analysis of Ascension Island basalts indicates that the plume's melt source came from the same mantle source region as the plume that formed St Helena (Kar, 1997).

2.1.1 Volcanic History

Ascension Island is predominantly composed of volcanic deposits **(figure 2.1)**: 57% of the island is mafic and felsic lava flows and domes, 43% is pyroclastic material (Daly, 1925; Harris, 1983; Weaver et al, 1996; Chamberlain et al, 2016) and there are small quantities of guano and beach rock (Harris, 1983). The volcanic rocks show a compositional range of basalt-hawaiite-mugearite-benmoreite-trachyte-rhyolite which represents fractional crystallisation of alkali basalt magmas (Nielson and Sibbett, 1996; Karr et al, 1998; Ammon et al, 2009, Chamberlain et al, 2016). Mafic Hawaiian and Strombolian eruptions are the dominant eruption style, whilst Sub-Plinian eruptions are localised to two main areas. These areas are the Central Felsic Complex and the Eastern Felsic Complex (Nielson and Stiger, 1996; Nielson and Sibbett, 1996; Karr et al, 1998).

Volcanism on Ascension Island has been ongoing for ~6-7 Ma (Harris, 1983; Chamberlain et al, 2016) and the subaerial portion of the island was formed in the last 1 Ma (Weaver et al, 1996; Jicha et al, 2013; Chamberlain et al, 2016). Trachytic volcanism began in the Central Felsic Complex (Middleton Ridge and Green Mountain), with the oldest exposed rocks on the island ranging from 1094-719 ka (Karr et al, 1998; Jicha et al, 2013). It consists of trachytic, rhyolitic and benmoreitic lavas and trachytic pyroclastic rocks (Jicha et al, 2013).

Trachytic volcanism continued in the northern half of the island from 829-652 ka (Jicha et al, 2013), and overlapped the production of the first mafic lavas (758-705 ka),

which are located east of Cross Hill and west of Devil's Riding school (Jicha et al, 2013). The final stage of the ~500 kyr silicic volcanism is located at Ragged Hill and on the south-west slope of Green Mountain (Karr et al, 1998). They are composed of trachytic lavas with an age of 637-602 ka (Jicha et al, 2013).

Mafic lavas, found on the southern half of the island, were produced after the Central Felsic Complex and have an age of 589-298 ka (Jicha et al, 2013). This eruptive period includes a mafic lava from South Gannett Hill with an age of 534 ± 18 ka (Jicha et al, 2013) and a mafic lava from the southeast of the Green Mountain Peak with an age of 350 ± 3 ka (Harris et al, 1982).

The second felsic centre is the Eastern Felsic Complex and has an age of 169-52 ka (Jicha et al, 2013) and is composed of trachytic and rhyolitic domes and lavas, and mafic lavas and scoria cones (Nielson and Sibbett, 1996; Karr et al, 1998; Jicha et al, 2013).

Mafic volcanic products dominate the north-west of the island and range in age from 38-0.51 ka (Nielson and Sibbett, 1996; Jicha et al, 2013; Preece et al, 2018). The eruptions produced predominantly hawaiite lavas (Weaver et al, 1996, Nielson and Sibbett, 1996), and scoria cones (Nielson and Sibbett, 1996). The flows exhibit variable volume and areal extent, ranging from small flow lobes to aerially extensive flows up to 4 km long (Weaver et al, 1996).

2.1.2 Geochemistry

Ocean island basalts (OIB's) are derived from chemically anomalous mantle sources (Weaver et al, 1987). The small-scale heterogeneity seen within ocean island erupted products is due to the convective dispersal of the mantle material (Weaver, 1991).

The source for melt genesis under Ascension Island is an ancient subducted slab that contained a large volume of sedimentary rocks (Faneros and Arnold, 2003). Major and minor element trends within the rocks and xenoliths show that basaltic magmas evolved towards intermediate and silicic compositions by low pressure fractional crystallisation of the parent melt in a closed system (Webster and Rebbert, 2001; Chamberlain et al, 2016; Chamberlain et al, 2019). Ascension Island magma exhibits two varieties of alkaline, silicic magma (Webster and Rebbert, 2001). The first is enriched in Li and F, contains more Na relative to K and more alkaline. The second is depleted in F and Li, contains more K relative to Na and is less enriched in alkalis.

The mafic magmas have been characterised into three groups based on their Zr/Nb ratios **(figure 2.1)** (Weaver et al, 1996; Kar, 1997; Chamberlain et al, 2016). The south-west of the island consists of intermediate aged hawaiite lavas which have a Zr/Nb ratio of 4.1, placing it in the low Zr/Nb group. The south-east of the island consists of the oldest mafic lavas and pyroclastic deposits which have a ratio of 6.0, placing it in the high Zr/Nb

group. The rest of the island, and the youngest lavas, have a ratio of 5.0, placing them in the intermediate Zr/Nb group (Weaver et al, 1996; Kar, 1997). The slightly wider variation in Zr/Nb can be due to many factors: (1) crystal fractionation involving clinopyroxene and Fe-Ti oxide fractionation; (2) low degrees of partial melting of the mantle source of mafic magmas; (3) magma tapped from mantle sources which have different Zr/Nb ratios and alternate undergoing source mixing; (4) a combination of all the processes described above (Kar, 1997). The Sisters lava flows can be placed into the intermediate Zr/Nb group (Ammon et al, 2009).

The mafic lavas on Ascension Island are aphyric, sparsely phyric or rarely porphyritic with assemblages of plagioclase feldspar and olivine as the dominant phenocryst phase, clinopyroxene, and titanomagnetite (Atkins et al, 1964; Weaver et al, 1996; Nielson and Sibbett, 1996).

2.1.3 Sisters scoria cone complex

The SSCC is located in the north of the island **(figure 2.1)**. It consists of four scoria cones with the largest (~413m asl) being the second largest scoria cone on the island (Karr, 1997). The complex has erupted predominantly hawaiite lavas (Weaver et al, 1996; Nielson and Sibbett, 1996). The lava flows around SSCC preceded the scoria cone eruptions and were erupted synchronously from several different locations, controlled by north-west trending faults (Nielson and Sibbett, 1996). The last eruption at SSCC has been dated at 0.51 ± 0.18 ka (Preece et al, 2018) and is the youngest known eruption on the island (Atkins, 1964).

2.2 Basaltic Volcanism

Monogenetic basaltic eruptions predominantly produce scoria cones, built up by the accumulation of scoria and pyroclastic debris around vents (Sutawidjaja and Sukhyar, 2009), and small volume pyroclastic fall deposits and lava flows (Houghton and Hackett, 1984). Factors that affect the influence, style and distribution of basaltic volcanism, include; (1) rate of rise of magma, (2) rate of rise and the depth of formation of gas bubbles, (3) depth of fragmentation, (4) vent geometry, (5) interaction with of external water, (6) wind velocity, (7) eruption rate (Houghton and Hackett, 1984).

Pyroclasts from basaltic eruptions are unique recorders of the styles of eruptions. The textures these pyroclasts exhibit, (i.e. vesicularity, vesicle size and shape and crystallinity) give an important insight into eruption processes. These processes include fragmentation, vesiculation, phreatomagmatic interactions and post depositional processes.

Crystallisation during magma ascent can increase the magma viscosity and lead to fragmentation (Arzilli et al, 2019). However, crystallisation in basaltic magmas has previously been though to take place over a longer period of time than that required for magma to ascend to the surface (Arzilli et al, 2019; Moitra et al, 2018). Basaltic Plinian scoria have very large microlite crystallinities, compared with those of Hawaiian and Strombolian ejecta (e.g. Sable et al, 2006; Houghton and Wilson, 2008; Arzilli et al, 2019).

2.2.1 Hawaiian and Strombolian Eruptions

Hawaiian eruptions result from a gas-magma mixture that fragments before reaching the surface and generates lava fountains and lava flows (Parfitt and Wilson, 1995; Parfitt, 2004). These eruptions have low mass discharge rates that can be sustained over long periods of time (Gurioli et al, 2008). The major factors that control lava fountain heights, temperatures and accumulation rates are the exsolved magma-gas content and volume flux (Head and Wilson, 1989). The range of vesicle sizes is smaller in scoria clasts that originate from lava fountains, compared to those that originate from Strombolian explosions, due to the shorter residence time in the conduit (Parchetta et al, 2013). Higher fountains provide longer periods of insulation for the clasts, transport clasts to higher elevations, and allow continuous vesiculation and post-fragmentation expansion (Stovall et al, 2012).

Strombolian eruptions are characterised by small volume and short-lived explosions (Gurioli et al, 2008; Taddeucci et al, 2015). The erupted material is cooler and more fluidal prior to eruption, and cools and solidifies further during transportation from the vent (Parfitt, 2004). This leads to the accumulation of tephra as fall deposits or scoria cones (Walker, 1973; Parfitt, 2004). Strombolian scoria displays a population of large vesicles with irregular shapes, implying extensive coalescence and possible readjustments around phenocrysts (Polacci et al, 2006). The scoria ejected from mild-moderate Strombolian activity shows a high inter-connectivity and complex vesicle shapes (Gurioli et al, 2008).

2.2.2 Eruption Mechanisms

The primary controlling factor of eruption style is magma ascent rate. Fast rise speeds lead to Hawaiian style eruptions, whilst slow rise speeds lead to Strombolian eruptions (Parfitt and Wilson, 1995). The Rise Speed Dependent Model (RSD) **(figure 2.2)** (Parfitt, 2004), demonstrates that if the rise speed is high, bubbles are unable to rise far through the overlying magma before it is erupted. The model assumes that two different fluid phases, magma (liquid) and gas, are present but act as single, combined gas-magma phase where bubbles grow and ascend until the bubble volume is large enough for fragmentation to initiate (Sparks, 1978; Houghton and Gonnerman, 2008). After fragmentation, there is less friction exerted on the conduit walls, allowing rapid acceleration

and eruptions to occur (Blackburn et al, 1976; Parfitt, 2004). However, if the rise speed is low, gas bubbles rise up through the overlying magma and segregate due to a greater bubble coalescence depleting the gas-magma mixture, which leads to lower fountaining heights (Parfitt and Wilson, 1995). The rise speed of bubbles depends mostly on size, with larger bubbles rising faster and overtaking smaller bubbles or occasionally forming a gas slug (Parfitt, 2004). For Strombolian eruptions, the RSD assumes gas segregation is progressive and therefore can be applied to any open system. For Hawaiian eruptions the RSD assumes a homogenous gas-magma flow and different driving gases, but the model is only successful if H_2O is the main gas (Parfitt, 2004).

The Collapsing Foam Model (CF) **(figure 2.2)** (Vergniolle and Jaupart, 1986; Parfitt, 2004) assumes that magma is stored within the chamber at depths where gases can exsolve. The gas bubbles rise and accumulate at the top of the storage region, packing into a foam layer. As the foam reaches its critical thickness, it becomes unstable and collapses, allowing the bubbles to coalesce and form gas pockets, otherwise known as gas slugs. These slugs rise faster than the surrounding magma, migrate up an open vent system and are erupted (Parfitt, 2004; Burton et al, 2007). A slower frequency of arriving gas slugs to the surface allows the melts to outgas and become more viscous due to rheological stiffening, creating a more explosive eruption (Lautze and Houghton, 2005).

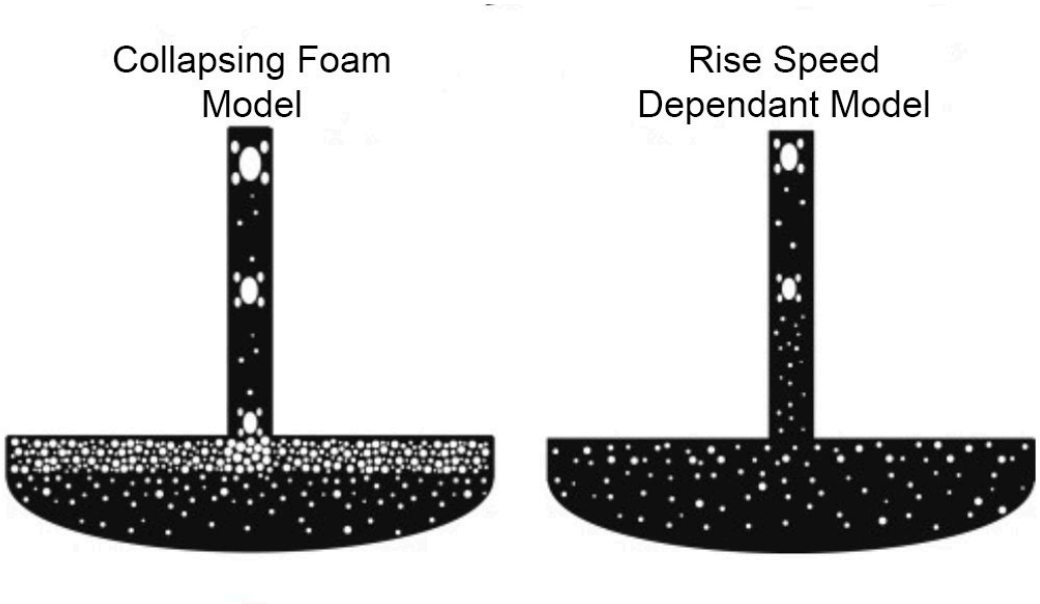

Figure 2.2: *Diagram showing the collapsing foam model of Vergniolle and Jaupart (1986) and the Rise Speed Dependant Model of Parfitt (2004) (Houghton and Gonnerman, 2008).*

In the CF model, Strombolian eruptions represent accumulation and bursting of gas slugs at shallow depths and hence requires specific vent conditions, whilst Hawaiian eruptions imply instantaneous foam collapse and the dependence on CO_2 as the driving gas (Parfitt, 2004).

2.2.3 Role of Volatiles

Volatiles are extremely important because exsolved gases are less dense than the melt, which creates a buoyancy and allows the magma rise to the surface and erupt (Parfitt et al, 1993; Woods and Cardoso, 1997; Houghton and Gonnerman, 2008). There are four main processes that allow the magma to gain buoyancy. The first is ascent driven compression lowering volatile solubility and resulting in volatile exsolution and bubble nucleation at the exsolution surface (Sparks, 1978; Gonnerman and Manga, 2007; Houghton and Gonnerman, 2008). The second is crystallisation enriching the melt fractions in the volatiles and leading to volatile exsolution (Houghton and Gonnerman, 2008). The third is ascent driven decompression resulting in volume expansion of the exsolved volatiles (Sparks, 1978; Houghton and Gonnerman, 2008). The fourth is buoyantly ascending decoupled bubbles that can rise and/or accumulate somewhere else in the conduit (Vergniolle and Jaupart, 1986; Parfitt and Wilson, 1995; Parfitt, 2004; Houghton and Gonnerman, 2008).

Volatiles can impact the eruptive behaviour of basaltic magmas through: (1) closed system ascent of melt and bubbles resulting in rapid decompressive bubble growth above the exsolution surface or, build-up of pressure and magmatic fragmentation (Gonnerman and Manga, 2007; Houghton and Gonnerman, 2008); (2) feedbacks between eruptions, decompression melting, magma crystallisation, and magma rheology leading to more explosive eruptions (Sparks and Pinkerton, 1978; Metrich et al, 2001; Del Carlo and Popilio, 2004; Houghton and Gonnerman, 2008); (3) open-system gas loss at depth, leaving volatile depleted magma with decreased potential for explosivity (Melnick and Sparks, 2002; Houghton and Gonnerman, 2008); (4) open-system accumulation of volatiles, resulting in the formation of gas slugs and Strombolian eruptions (Andronico et al, 2005; Houghton and Gonnerman, 2008); (5) development of permeable pathways, allowing open-system gas loss and a decrease in explosivity due to varying locations of fragmentation (Melnik and Sparks, 2002; Houghton and Gonnerman, 2008; Namiki and Manga, 2008; Polacci et al, 2008). Increasing the volatile content in the magma column leads to a decrease in local mean density within the bubble-rich magma layer and leads to a more efficient convection of large bubbles and gas slugs (Colo et al, 2010).

2.2.4 Hawaiian – Strombolian Eruption Style Transitions

Monogenetic basaltic eruptions can exhibit both Hawaiian and Strombolian phases (Parfitt, 2004). The transitions between the two styles reflects degassing patterns controlled by magma rise rates within the conduit, rather than the geometry of the conduit or magma storage body, and the gas content and viscosity of the magma (Parfitt and Wilson, 1995; Houghton et al, 1999, Houghton and Gonnerman, 2008).

The transition from Strombolian to Hawaiian activity occurs when bubble coalescence produces a magma foam (Polacci et al, 2006). This collapses and rises through the conduit as a core of gas, surrounded by a moderately vesiculating magma, before erupting as a fountain (Polacci et al, 2006). In contrast, transitions from Hawaiian to Strombolian activity require decreasing magma rise speed and lower gas contents in order to reduce the amount of bubble coalescence (Parfitt and Wilson, 1995; Polacci et al, 2006). Changing the gas volume only, does not lead to a transition but pushes the current activity towards either end member (Parfitt and Wilson, 1995).

2.2.5 Fragmentation

Fragmentation converts magmas from a continuous liquid phase with gas bubbles and crystals to a gas phase with pyroclasts. Fragmentation by rapid acceleration begins when a fresh input of magma is inputted into the shallow magma chamber, changing the internal pressure and causing bubbles to begin to nucleate and force the magma upwards (Cashman and Scheu, 2015).

Basaltic magma is fragmentated via inertial fragmentation, driven by rapid vesiculation (Lui et al, 2017), where the expansion of gas bubbles during decompression leads to stretching and break up (Mangan and Cashman, 1996; Houghton and Gonnerman, 2008; Namiki and Manga, 2008; Mangan et al, 2014). In opposition to silicic eruptions, the viscosity of basaltic eruptions is believed to be too low to reach the conditions where brittle fragmentation occurs (Moitra et al, 2018). However, basaltic magmas that have crystallised on ascent can increase the viscosity of the magma, triggering brittle fragmentation (e.g. Arzilli et al, 2019; Moitra et al, 2018; Zimanowski et al, 1997).

If fragmentation is controlled by bursting of vesicles, then magma would only fragment as it exceeds the threshold vesicularity, due to the instability of thin bubble walls (Houghton and Gonnerman, 2008). This mode of fragmentation would develop a uniform, highly vesicular (75-83 vol %) clast population (Houghton and Wilson, 1989). However, this process is only successful when the rise rate of magma is significantly faster than the rise velocity of the bubbles in the magma (Houghton and Wilson, 1989). If bubbles grow faster than they rise, the magma will carry on accelerating and fragment. However, if the gas escapes before reaching the surface, it prevents fragmentation and the magma is erupted as lava (Cashman and Scheu, 2015).

2.2.6 Quenching

Quenching on fragmentation or during cooling can interrupt vesiculation, which leads to the vesicle diversity identified in scoria clasts (Namiki and Manga, 2008; Moitra et al, 2013; Parcheta et al, 2013). If magma resides in the vent, there is more time for rising bubbles to

grow and coalesce before eruption. Similarly, if ascent is fast, the bubble residence time is shorter and there is less time for growth and coalescence (Houghton and Gonnerman, 2008; Parcheta et al, 2013). If clasts are representative samples of fragmentation surfaces, then vesicle characteristics can provide information on the extent of non-explosive degassing of the magma involved in 'dry' magmatic eruptions (Houghton and Wilson, 1989).

2.3 Phreatomagmatic Eruptions

Phreatomagmatic eruptions occur when rising magma encounters ground or surface water and heats it rapidly, causing an explosion (Heiken, 1972). The process begins when two fluids, water and magma, with one above the boiling point of the other, establish a direct contact across an interfacial surface by a shockwave (Pardo et al, 2014). A small volume of water is vaporised after making contact with the magma and the vaporisation energy causes the magma to fragment, increasing the surface area of the contact between magma and water and stimulating further vaporisation of water (Sheridan and Wohletz, 1983). Once the total vaporisation energy exceeds the limit of containment, the system erupts (Sheridan and Wohletz, 1983).

Magma-water interaction is controlled by several factors: (1) geometry and location of the contact between magma and water; (2) the process by which thermal energy is transferred from the magma to the water; (3) the degree of which the magma and water mix prior to eruption; (4) the thermodynamic equation of state for mixtures of magma fragments and water; (5) the dynamic metastability of superheated water; (6) the propagation of shock waves through the system (Wohletz, 1986).

The eruptions can consist of single explosions or as pulses that are interspersed with magmatic activity (Sheridan and Wohletz, 1983). Many eruptions exhibit transitional styles from magmatic to phreatomagmatic mechanisms operating in rapid succession (Houghton and Schmincke, 1986). Simultaneous, discrete phreatomagmatic and Strombolian activity from a single vent have been recorded in numerous basaltic eruptions (Houghton and Schmincke, 1986; Houghton et al, 1999).

Phreatomagmatic activity is characterised by greater fragmentation efficiencies than magmatic fragmentation (Lui et al, 2017). Fragmentation during water interaction leads to brittle breakage in response to high rates of thermal to mechanical energy transfer (Sheridan and Wohletz, 1983; Kósik et al, 2016; Lui et al, 2017). Typical features associated with phreatomagmatic eruptions include tuff rings and maars, cohesive 'wet' ash, accretionary lapilli, base surge deposits with bomb impact sags and fine grained, poorly sorted, ash and lithic rich beds (Walker, 1973; Barberi et al, 1989; Bertagnini et al, 1991; Kósik et al, 2016; Swanson and Houghton, 2018).

2.4 Inferring Eruption Styles from Textural Studies

The exterior and interior of pyroclasts provide important insights into the processes that occur prior, during and after an eruption (Sparks, 1978; Shea et al, 2010). The physical changes occurring in magma in shallow conduits result from two processes (Lautze and Houghton, 2007). The first is continuing vesiculation in the intervals between passage of bubble slugs and the second is mingling and mixing of high and low-density magma during passage/behind the bubble slugs (Lautze and Houghton, 2007). Strombolian eruptions involve more viscous magmas and produce ragged looking pyroclasts, whilst Hawaiian eruptions involve less viscous magmas and produce fluidal pyroclasts (Houghton et al, 2016). However even after classifying the deposits based on textural characteristics, it can be difficult to fully distinguish the two eruption types just by studying the eruptive material **(table 2.1)** (Houghton et al, 2016).

Hawaiian Eruptions	**Strombolian Eruptions**	**Phreatomagmatic Eruptions**
- Smooth skinned and fluidal shape[a,c] - Spherical lava droplets and Pele's hair[b] - Mean vesicularity of 60-70%, spherical – slightly ovoid shaped[e,f] - Produces mainly sideromelane glass[f]	- Equant grains[b] - Surfaces are rough with botryoidal fractures and dykitaxitic textures[f] - Mean vesicularity of 55-67% and ovoid-spherical shaped vesicles[b,e] - Low proportion of lithics[c] - Produces angular sideromelane and blocky tachylite glass[f]	- Blocky and equant grains[f] - Plate like shapes[f] - Flat and smooth fractures[a] - Smooth or stepped surfaces[b] - Vesicles are rare but spherical[b] - Rich in lithic fragments[d]

Table 2.1: *summary of the differences in glass, groundmass, surface textures and vesicularity of tephra from Hawaiian, Strombolian and Phreatomagmatic eruptions. [a]Heiken, 1972, [b]Schmitch et al 2017, [c]Guilbard et al, 2009, [d]Risso et al, 2008, [e]Ross and White, 2012, [f]Heiken and Wohletz, 1992.*

2.4.1 Juvenile Clasts

Juvenile clasts form from the explosive disintegration of erupting magma. The morphology and shape of juvenile clasts are strongly influenced by the viscosity of the melt and vesicle content during fragmentation (Houghton and Gonnerman, 2008). They record the texture and chemical composition of pre- and syn-eruptive magma changes (D'oriano et al, 2014).

The shapes of juvenile clasts **(figure 2.3)** are related to melt rheology at fragmentation and during transport: angular and blocky scoria with planar or curvi-planar surfaces imply brittle failure of magma that was cooler and more viscous (Houghton and Carey, 2015), whilst fluidal and elongate surfaces imply the magma was still molten after fragmentation (Jutzeler et al, 2016).

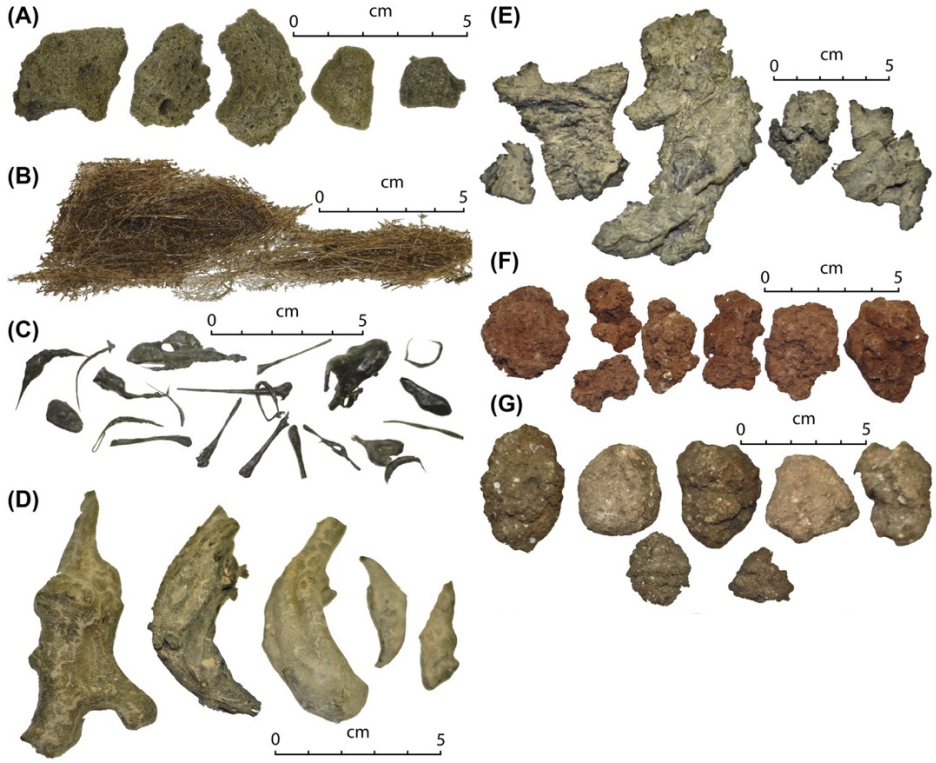

Figure 2.3: *Examples of juvenile basaltic tephra.* ***A)*** *Reticulite,* ***B)*** *Pele's hair,* ***C)*** *Achneliths,* ***D)*** *Fusiform clasts,* ***E)*** *Transitional lapilli,* ***F)*** *Red weathered scoria,* ***G)*** *Sub-rounded, dense lapilli clasts (Houghton and Carey, 2015).*

2.4.2 Glass

Tachylite glass is a product of crystallisation at a micrometer scale which is controlled by local enrichment and depletion of elements that are induced and rejected by the adjacent, precipitating minerals (Taddeucci et al, 2004). Sideromelane represents the bulk magma batch (Taddeucci et al, 2004) and dominates in Strombolian and Hawaiian products (Taddeucci et al, 2015). **Table 2.2** shows the physical characteristics of sideromelane and tachylite.

Microlites found in sideromelane and tachylite have a euhedral shape. Plagioclase is tabular with skeletal tails, olivine and Ti-magnetite are blocky or sub-rounded and pyroxenes are prismatic and have iron rich rims (Taddeucci et al, 2004). The higher content of small microlites and low vesicularity in tachylite is the product of longer residence times within the conduit (Taddeucci et al, 2004).

2.4.4 Groundmass

Groundmass textures can be massive and pervasive, with nucleation of fine grained microlites implying fast growth and high degrees of cooling (Cox et al, 1976; D'oriano et al, 2014). Slow cooling and degassing can lead to skeletal faceted microlites (D'oriano et al, 2014). Microlite groundmasses are also related to degassing induced crystallisation of magma prior to fragmentation (D'oriano et al, 2014). Oxide microlites on pre-existing

interfaces (both surfaces and contacts) are related to heterogeneous nucleation and growth which indicates the process of recycling (D'oriano et al, 2014). Minerals that are rimmed by oxides of iron rich laths form in the reheated clasts by heterogeneous nucleation under high oxidising conditions (D'oriano et al, 2014).

It is assumed that crystal growth and nucleation results from quenching. However, when a reasonable quench rate of 20°k/s is applied for fine grained material, the fastest feldspar growth rates of 10^{-6} cm/s lead to a net crystal growth of 0.2 μm (D'oriano et al, 2014). This shows that microlites reflect the response to cooling of syn-eruptive degassing during the ascent of magma (D'oriano et al, 2014), and therefore, glass with a high microlite content is associated with a slow rising and crystallising magma, and glass with a low microlite content is associated with a rapid rising and crystallising magma (D'oriano et al, 2014).

	Sideromelane	**Tachylite**
Colour	Light brown[a,b]	Dark brown – black[a,b]
Shape	Irregular and frothy[a]	Angular[a]
Vesicle Properties	Small, round to elongate, smoothly shaped with some coalescence[a] 60-70% vesicularity[b]	15-20% vesicularity[b] Fewer but larger coalesced vesicles[a]
Matrix	Glassy[a] ~ 2-5% un-zoned olivine and 10-20% plagioclase[b]	Devitrified to cryptocrystalline[a] Sparse microlites[a] 0-7% olivine phenocrysts[b]
External Surface	Smooth, curved glass surfaces and tubular textures[a] Highly stretched glass filaments[a]	Irregular glassy surface[a] Sparse-abundant small-scale fractures in parallel sets[a]
Miscellaneous	Small tachylite xenoliths welded to the surface[b]	

Table 2.2: *Comparing the observable characteristics and differences of two types of glass; sideromelane and tachylite. [a] Guilbard et al, 2009. [b] Heiken, 1978.*

2.4.5 Vesicularity

Bubbles develop through stages of nucleation, growth (through diffusion and decompression expansion), (3) bubble interaction and coalescence and collapse/escape of bubbles (Cashman and Mangan, 1994; Lautze and Houghton, 2005, 2007). Each of these stages are continuous, meaning that multiple stages can take place at the same time, and is represented by variations in vesicle size and shape (Lautze and Houghton, 2007). Low vesicularities represent melts that were fragmented later in the vesiculation history and infer the beginning of coalescence and bubble collapse, whilst a high vesicularity infers that

collapse and outgassing were the dominant processes at the time of fragmentation (Lautze and Houghton, 2005).

A magma body becomes more progressively degassed as it rises (Polacci et al, 2006). An infrasound study (Colo et al, 2010) found that approximately 60% of magma degassing occurs under non-equilibrium conditions. The absence of similar sized and equidistant vesicles in scoria suggests that the system is far from equilibrium (Polacci et al, 2009).

Vesicularity is greatly influenced by the relationship of three parameters: (1) rise rates of bubbles through magma; (2) rise rates of magma through conduit (3) discharge rate of magma (Houghton and Wilson, 1989). The shapes of the vesicles reflect the time available, prior to quenching, when bubbles are able to relax from complex shapes into spheres. They also reflect the residence times of the magma in the conduit: longer residence times lead to the growth of larger, irregular shaped vesicles through coalescence, demonstrating that coalescence is occurs at the time of melt quenching, whilst short residence times leads to small, spherical vesicle development (Parcheta et al, 2013). Polacci et al (2009) suggests two processes that account for the distribution of larger vesicles. The first is the steady state vesicle growth through coalescence. The second is the continuous nucleation of new vesicles.

The relationship between the interior and exterior of scoria is important for understanding the diversity of the micro-textures. Rinds that have been quenched rapidly after fragmentation contain a higher population of smaller vesicles and provide a limited opportunity for growth and coalescence (Stoval et al, 2011). It is possible to use the variation between the interior and the rinds to establish the processes that occurred between fragmentation and quenching (Stoval et al, 2011).

3. Methods

The primary aim of this thesis was to undertake a detailed textural study of pyroclasts from a recent eruption from the SSCC. Additionally, petrographic studies were undertaken on lava and tephra samples to attempt to define the products from single eruptions, and simple calculations were made to estimate the volume of the edifices that make up the SSCC. Fieldwork was carried out by the project supervisors, Rich Brown and Charlotte Vye-Brown in 2019 and the samples were returned for the physical and petrographic analysis undertaken in this thesis. Modelling of tephra dispersal was carried out using data collected in the field and in collaboration with Julia Crummy (British Geological Survey).

A textural study was chosen because pyroclast textures are the ideal data source for reconstructing eruption processes; Understanding cone and tephra volumes are beneficial in order to assess the percentage of material erupted explosively in respect to the total erupted volume (lava flow + cone + fall deposits) (Kervyn et al, 2012). Componentry analysis can identify changes within the deposit that may record changes in eruptive activity. Vesicularity is a useful primary indicator of the textural homogeneity or heterogeneity of the magma at the point of fragmentation (Shea et al, 2011). Vesicularity can also infer details about eruption mechanisms, such as quenching and fragmentation. Grain size distribution profiles can determine eruption dynamics, such as pyroclast transport and sedimentation, fluctuations in mass discharge rates and fragmentation efficiency (Houghton and Gonnerman, 2008) and, can be input into tephra dispersal models. Finally, petrography and vesicle textures can identify changes in eruption conditions or activity, for example magmatic vs phreatomagmatic fragmentation and magma viscosity (Houghton and Gonnerman, 2008).

3.1 Fieldwork

Fieldwork on Ascension Island was undertaken by the project supervisors, Rich Brown, where the pyroclastic fall deposit was sampled. The deposit that is the main focus of this study, Unit 2, was measured at >50 sites in the field. At each site pits were dug in the tephra to measure the thickness and log the deposit. Two sites, (localities SIS 6 and 51) were sampled in detail for laboratory analysis (the subject of this thesis). The first site was on the dispersal axis and is referred to in the text as SIS 51. The second is more distal and to the west of the scoria cone complex and is referred to in the text as SIS 6. See **figure 4.6** for the exact localities of the two units in relation to the scoria cone complex. The lava samples were collected over two field seasons by Charlotte Vye-Brown.

3.2 Volume of a cone

The volume of scoria cone 4 was calculated using two methods, in order to assess the percentage of material erupted (Kervyn et al, 2012).The first method calculates the volume of each cone within the complex using equation 1 (Kervyn et al, 2012), where W_{co} and W_{cr} are the width of the cone and crater, D_{cr} is the depth of the crater and H_{co} is the height of the cone. The equation accounts for the fluctuations in the H_{co}/W_{co} and W_{cr}/W_{co} ratios and D_{cr}, and assumes that the cone is either, an axi-symmetric truncated cone on a flat or semi-flat substrate, or is an inverted cone that represents the crater, cone and crater assembly volume (Kervyn et al, 2012).

$$V_{co} = \frac{1}{2}\,\pi\,[\,\frac{W_{co}^3\,H_{co}}{W_{co}-W_{cr}} - W_{cr}^3\,\left(\frac{H_{co}}{W_{co}-W_{cr}} + \frac{D_{cr}}{W_{cr}}\right)\,] \qquad (1)$$

Equation 1 requires average values for W_{co}, W_{cr} and H_{co} which allows it to be used to estimate the volume of an asymmetric cone (Mattsson, 2012). In order to obtain the area of cone 4, without the overlap of the other cones, simple geometric approximation was used based on ellipsoid shapes **(figure 3.1)**. The volume of each shape was subtracted from cone 4's total volume to produce the volume of cone 4 only.

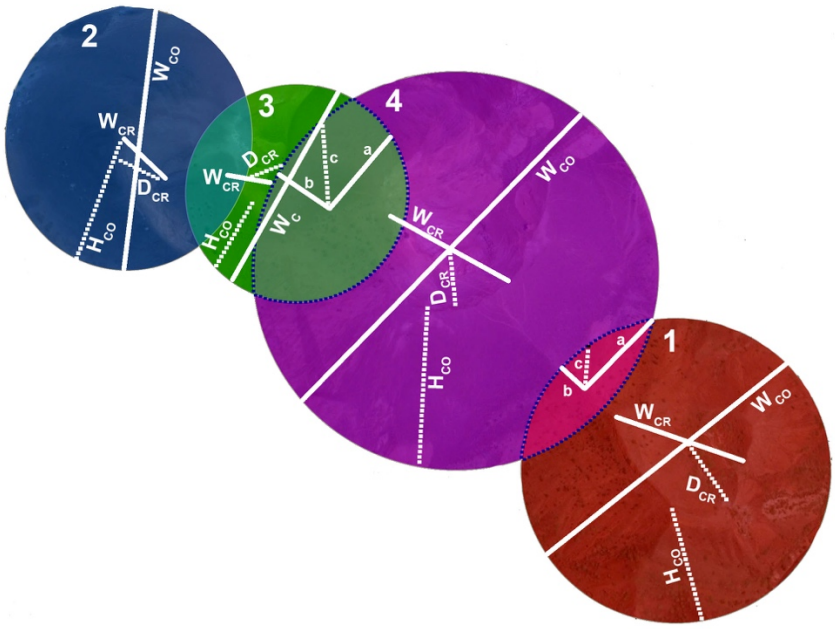

Figure 3.1: *Schematic of the shapes used to calculate the volume of the individual cones and total Unit 2 scoria cone. Ellipsoids are defined by blue dashed lines and cones are labelled (1, 2, 3, 4). W_{cr}, W_{co}, D_{cr}, H_{co} are cone measurements and inputted into equation 1. a, b, c are ellipsoid measurements and are inputted into equation for the volume of an ellipsoid (V_e = ¾ π abc).*

The second calculates the total volume of cone 4 seen on the surface. A MATLAB script, created by E. Llewellin (**figure 3.2)** incorporates the dimensions of the cones within the scoria cone complex and calculates the volume of each, assuming they are truncated cones. It then locates all the pixels present within cone 4 and identifies whether the same

pixel overlaps with another cone, based on its distance from the centre of cone 4. If an overlap is detected, the pixel is dismissed, leaving a volume of only scoria cone 4.

The dimensions of the cones were measured using Google Earth and the ruler tool. However, due to the complicated nature of the complex, the original dimensions of each cone were difficult to establish and so the values presented will have a significant degree of error.

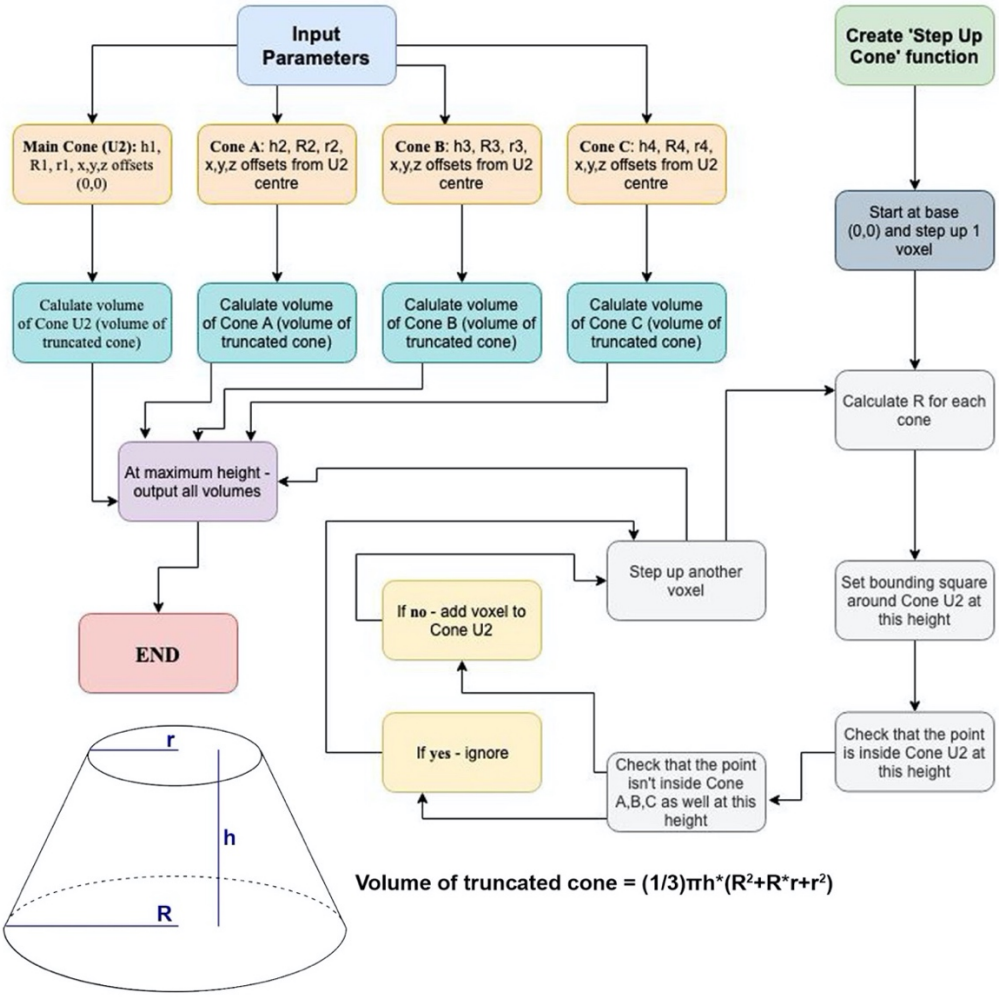

Figure 3.2: *Flow chart showing the process of the MATLAB script created by E. Llewellin. The script includes the input parameters and the setup of the loop. The truncated cone shows the origin of parameters R, r, h and the formula used to calculate the volume of a truncated cone.*

3.3 Componentry and Petrology

Componentry analysis was completed in order to correlate individual beds between the two sampling sites. For each sample, from SIS 51 and SIS 6, 500 clasts were randomly picked from the -4ϕ to -1ϕ size fractions and grouped on their physical characteristics: colour, shape and vesicularity (Eychenne and Pennec, 2012). These groups were: (1) dull and ash coated; (2) dull, grey and vesicular; (3) golden brown and vesicular; (4) glassy skinned and vesicular; (5) glassy skinned and elongate; (6) dense grey lithic clasts. For the

-1ϕ size fraction, the additional category red lithics was added due to the abundance in a dozen subunits.

15 samples from each group where then selected by random from the -2ϕ size fraction for petrographic analysis in order to identify any textures that could suggest changes in eruption conditions or activity.The samples were selected from beds where the groups were most abundant. Due to the fragile conditions of the scoria, they were impregnated in a resin prior to being cut and mounted onto glass slides. They were analysed under a petrological microscope and a Hitachi SU-70 Scanning Electron Microscope. To prepare the samples for the scanning electron microscope (SEM), the thin sections were coated in carbon.

9 samples, from the -3ϕ size fraction, were also selected for 3D analysis in the SEM in order to identify surface features that could also suggest changes in eruption conditions or activity. The samples were as follows: 3x dull and ash coated pyroclast; 3x glassy skinned and elongate pyroclasts; 1x glassy and vesicular pyroclast; 1x dull and vesicular pyroclast; 1x light brown and vesicular pyroclast. 4 additional samples of the dull and ash coated pyroclasts and glassy skinned pyroclasts were washed in the ultrasonic bath for 5 minutes and dried for 7 hours at 160 °C to remove any superficial surface grains and precipitates. The 3D clasts were mounted onto 1 cm discs using silver paint and coated in gold-palladium.

The SEM was used with a voltage of 15.0kV and a working distance of 15.00mm. The 2D images were taken using the backscatter and the 3D images were taking using secondary electrons without the backscatter.

After initial analysis, the groups dull grey and vesicular pyroclasts and glassy skinned and vesicular pyroclasts had the same characteristics as the dull and ash coated pyroclasts and glassy skinned and elongate pyroclasts. Therefore, they were combined to give four final types: (1) dull and ash coated; (2) glassy skinned; (3) golden brown and vesicular; (4) lithic clasts.

9 lava samples from around Sisters scoria cone complex and three tephra samples from Units 1,2 and 4 were also studied under the petrological microscope, in an attempt to link the individual fall deposit units to an associated lava flow(s) and possible cone origin. Images were taken using plain polarised light (PPL) and cross polarised light (XPL).

3.4 Grain Size Analysis

Grain size profiles were conducted at two locations in order to determine eruption dynamics and for application into tephra dispersal models. From the two locations, one was distal, and one was proximal to the vent. The samples were weighed to obtain a wet mass,

dried at 160 °C for 8 hours and reweighed to obtain a dry mass. They were then sieved at whole-phi steps, from -4ϕ to 3ϕ and each size fraction weighed.

Cumulative frequency curves were created from the size fraction wt.% and the parameters Mdϕ (median diameter) and σ_ϕ (standard deviation) were extracted. Mdϕ is the phi value where the curve crosses the 50% line and σ_ϕ is equal to equation 2.

$$\frac{\phi 84 - \phi 16}{2} \quad (2)$$

The values of σ_ϕ and Mdϕ were plotted against each other to show any relationships between the median grain-size and sorting of each subunit.

3.5 Vesicularity

Vesicularity measurements were taken to aid in the understanding of the eruption mechanisms. Vesicularity measurements follow the methodology and terminology of Houghton and Wilson (1989). The difference between the weight of a dry clast and the clast in water is the same as the mass of water displaced. The density of water is 1 g/cm^3, therefore the volume of the water displaced is equal to the mass of water displaced and the volume of water displaced is equal to the volume of the clast (Houghton and Wilson, 1989; Shea et al, 2010).

To set up the experiment, a balance was placed onto a flat surface and a metal ruler placed on top, with plasticine acting as a stabiliser. Wire was then fastened to each side and hung down under the balance, making sure not to touch the sides. The wires connected to a coat hanger which was used as the hook to attach and submerge the scoria, wrapped in parafilm and attached to a ballast of known weight and volume into the water **(figure 3.3)**. The water was monitored to ensure the same amount of the coat hanger was immersed.

To calibrate the equipment, the volume of the ballast was calculated using the formula for a volume of a cylinder. The ballast was weighed on the balance to obtain the dry mass. The ballast was then placed in water and the mass of the ballast + cage was recorded. The mass of the cage was subtracted from the ballast + cage to give the wet ballast mass. This was then subtracted from the dry ballast to give the volume of the ballast. This result was within 1 g of the calculated mass.

Clasts were washed in an ultrasonic bath for 5 minutes and dried in foil containers for 12 hours. 200 clasts were ranked by size order and weighed on a balance to obtain the dry mass (ω_{AIR}). They were then wrapped in parafilm (the exact amounts differed due to size and irregularity of edges). An individual square of parafilm was weighed to be 0.04 g and this value was multiplied by the number of squares used. The film was cut using the grid lines on the roll to ensure the weight had very little variation. When wrapping the clast,

care was taken to reduce the amount of air trapped between clast and film. The wrapped scoria was then placed into the cage and submerged in a beaker of water to obtain the weight in water (ω_{WATER}) and the weight on the scales recorded. Prior to the clast being added, the balance was zeroed.

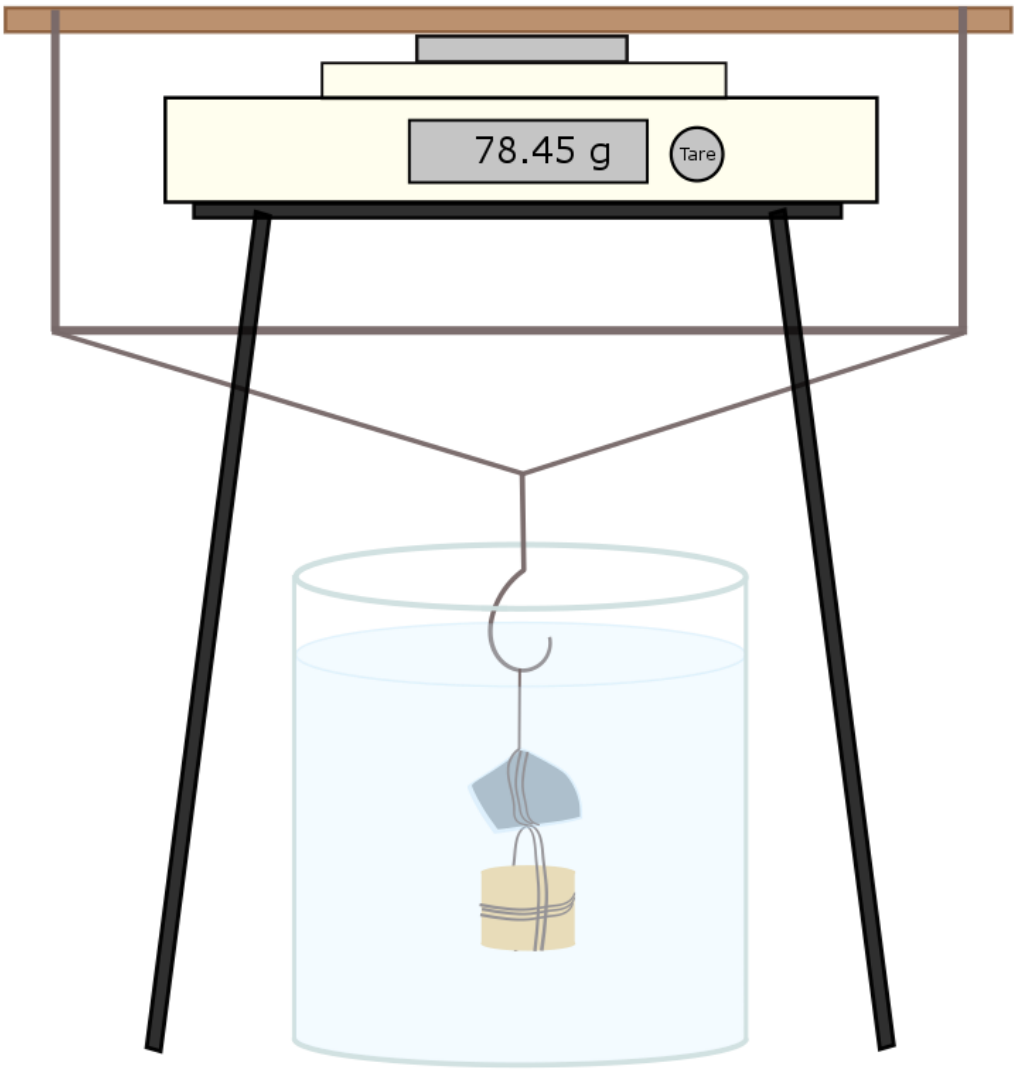

Figure 3.3: *Schematic set up of the apparatus used to collect the density measurements (Davies, personal communications).*

The mass of the parafilm, ballast and cage was measured without the clast, to give the weight of the film and ballast in water (ω_{FILM} and $\omega_{BALLAST}$). These weights were taken every ten clasts to ensure consistency.

In a spreadsheet, downloaded from FOAMS (Shea, 2016) the dry mass, weight in water, weight of film and weight of ballast were recorded. The following equations where then used to calculate the density (equation 3), the porosity (equation 4) and the vesicularity (Φ x 100) of the clasts. ρ_{DRE} is the dense rock equivalent of the clasts. For this study, porosity is not required and therefore the spreadsheet uses only equation 3 and combines both the porosity and vesicularity equation (equation 5) to get a the final vesicularity.

$$\rho_{BULK} = \frac{\omega_{AIR}}{\omega_{AIR}-(\omega_{WATER}-\omega_{FILM}-\omega_{BALLAST})} \quad (3)$$

$$\Phi = \frac{\rho_{DRE} - \rho_{BULK}}{\rho_{BULK}} \quad (4)$$

$$\Phi = \frac{\rho_{DRE} - \rho_{BULK}}{\rho_{BULK}} \, x \, 100 \quad (5)$$

3.6 Tephra Dispersal Maps

Thickness of the Unit 3 deposit from the Sisters scoria cone complex was measured at 32 sample pits. No pits could be created directly in front of the cone due to the covering of younger lava flows and restricted access zones. Each thickness is classed as a minimum thickness, as the top unit has been susceptible to weathering and erosional processes.

The thickness data collected in the field was imported into Google Earth Pro and isopach maps were created in order to understand the dispersal and the relative thicknesses of the deposit. The individual isopachs were processed to obtain the area within the isopach, and the volume of the tephra unit was calculated using the exponential thinning method (Pyle, 1989). This method implies an exponential thinning of the deposit away from the source and uses equations 6, 7 and 8 to calculate the volume of the deposit.

$$\ln(T) = \ln(T_o) - kA^{1/2} \quad (6)$$

$$m = \frac{\ln(2)}{b_t} \quad (7)$$

$$V = 13.08 T_o {b_t}^2 \quad (8)$$

Where, ln(T) is log(thickness), T_o is the maximum thickness, k is the thinning constant, $A^{1/2}$ is the area of deposit, m is $k\sqrt{\pi}$ and b_t is the half thickness. To produce the ln(thickness) plot the ln(T) calculated from equation 6 is plotted against isopach area$^{1/2}$.

For this study, the lack of frontal thickness measurements required the distance that the isopachs extend towards the sea to be inferred, following the general trend of the 50 cm and 20 cm isopach. The most distal isopach from field data was the 5 cm isopach, and the 1 cm isopach was created by extending the trendline from the exponential thinning graph**.**

The thickness data was processed further using TephraProb (Biass et al, 2016). TephraProb is a package that contains a series of MATLAB functions that produces hazard assessments for tephra fallout (Biass et al, 2016). Vent, eruption, wind and grain size distribution data were inputted into the model **(Appendix 1)** and probability and isomass maps were outputted. The inversion code of Tephra2 (Connor and Connor, 2006) was also used. For this code, thickness data with the corresponding GPS localities and wind data were inputted into the model and eruption parameters, such as column height, volume and erupted mass were the output. The inverse approach was taken due to limited data around the front of the crater causing inaccuracies on the output maps from TephraProb.

4. Results

4.1 Cone Morphology

The Sisters Scoria cone complex consists of a minimum of four scoria cones that built up from a base of ~200 m asl to 413 m asl and coalesced during the eruption periods **(figure 4.1).**

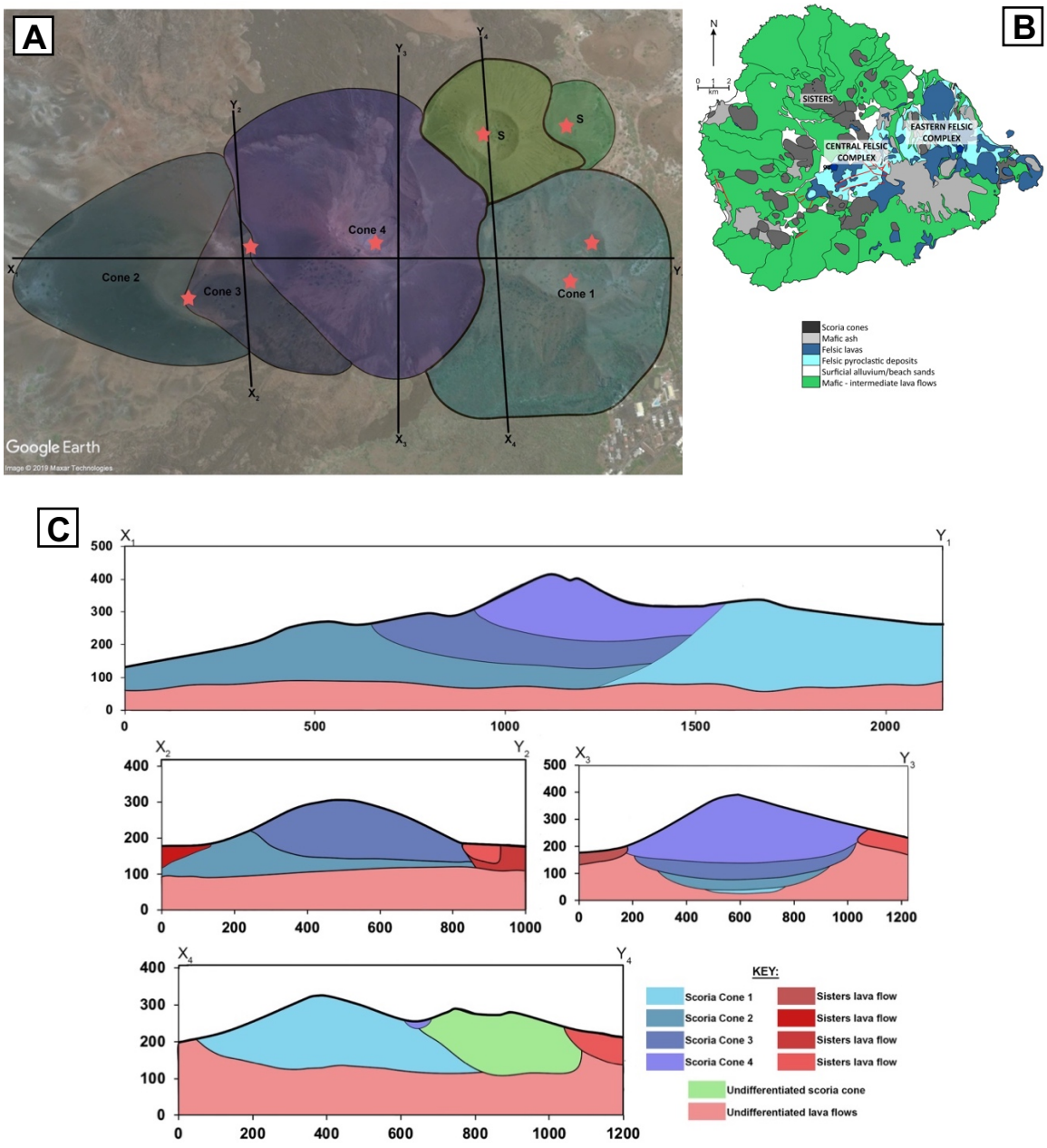

Figure 4.1: A) *Aerial view of the four scoria cones that make up the scoria cone complex. Numbers represent the suspected age of the cones, based on field relations, with 1 being oldest. S: scoria cones where the relationship with Sister's is unknown. Stars represent vent location.* ***B)*** *Map showing the location of the SSCC on the island.* ***C)*** *Schematic topographic cross sections through the Sisters scoria cone complex. Note that the dip of the flanks, depth of the cones and thickness of the lava flow are not true to scale, and the purpose of the schematic is to show the relationships between the different cones.*

Cone 1 is the oldest in the complex. It reaches 336 m asl, with a base height of 207 m and is asymmetrical with a 530 m long ridge that extends to the west and is partially covered by a younger cone. There are two sub-spherical, northern facing craters. The first is ~240 m in diameter with a depth of ~33 m and the second is ~120 m in diameter with a depth of ~20 m. The cone is composed red and orange tephra and has a heavy covering of green vegetation on the flanks and in the crater. The crater is not breached and does not appear to have emitted lava flows.

Cone 2 formed ~800 m from cone 1 (centre of crater to centre of crater). It reaches 298 m asl with a base height of 175 m asl and is asymmetrical, with a 400 m long western flank following the direction of the prevailing winds. The cone has a southern facing, spherical crater with a diameter of ~155 m and a depth of ~12 m. It is composed of black tephra that has an orange/brown coating in the crater. Vegetation is sparse and concentrated on the south and east flanks. The crater isn't breached. Two lava flows extend from the base at either side of the cone and are inferred to be associated with the cone.

Cone 3 grew out of the crater of cone 2 and is marked by oppositely dipping beds on the southern flanks **(figure 4.2)**. The asymmetrical cone reached 304 m asl with a base height of ~177 m asl. However, only a small volume of the cone is visible at the surface. The crater is inferred to be ~105 m in diameter and have a depth of ~6 m. The cone is composed of black/brown tephra with a sheet of red tephra on the northern flank. Vegetation is sparse and seen only on the southern flank. Lava flows on the northern side are inferred to be associated with cone 3.

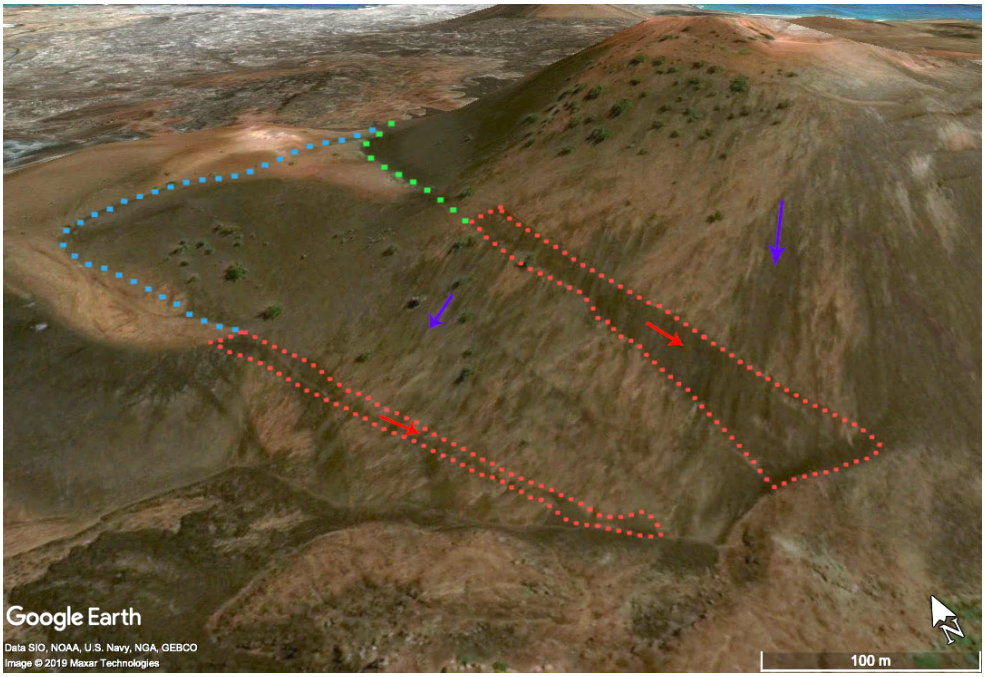

Figure 4.2: *Photograph showing the field relationships between the cones. The dark bands, outlined in red, dip N-S and represent the base of the new cone. The blue arrows indicate the E-W slope direction of the cones. The green dashed line outlines the base of cone 4 and the blue dashed line outlines the base of cone 3.*

Cone 4 is the youngest and grew upwards through cones 1, 2 and 3. A band of oppositely dipping tephra mark the boundary of cone 4 from cone 3 on the southern flank and tephra covers 219 m of the ridge from cone 1. The cone reaches 413 m asl with a base height of ~200 m asl and is symmetrical but breached to the north by a lava flow **(figure 4.3).** The crater is spherical with a diameter of ~300 m and a depth of ~49 m. Two lava flows are associated with the cone; the first breached the cone and the second protrudes from the base of the cone on the southern side. The cone is composed of black tephra with a sheet of red tephra at the peak and in the crater. Vegetation covering is sparse and concentrated on the southern flank.

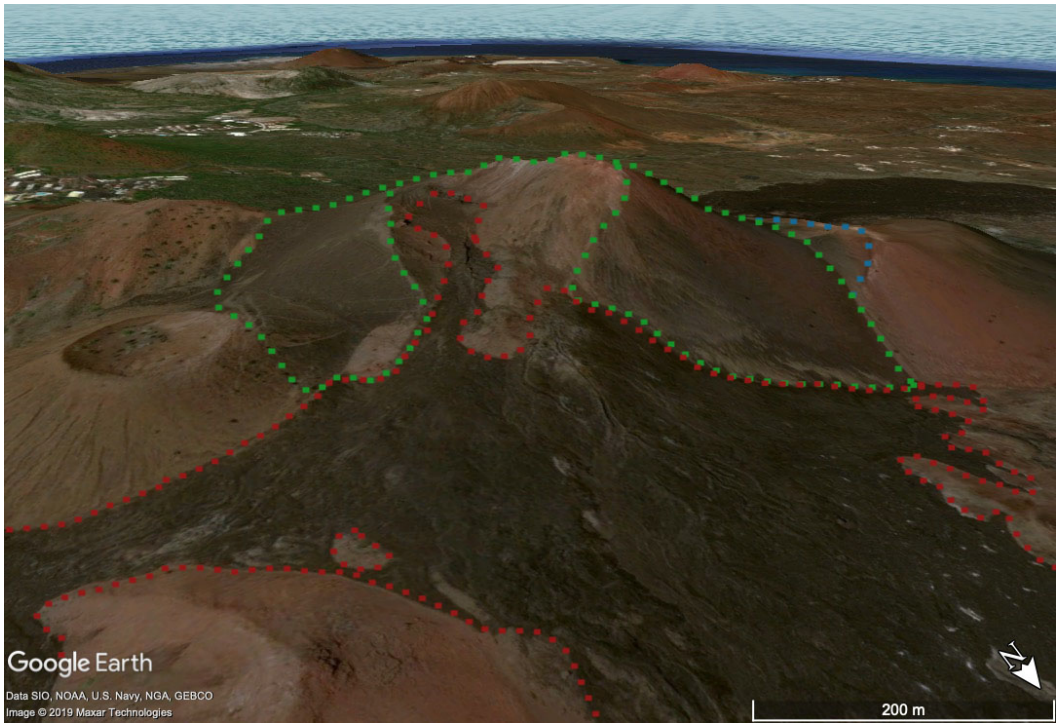

Figure 4.3: *Photograph showing the breached Unit 2 scoria cone. Red dashed lines outline one of the most recent lava flows. Green dashed lines outline the breached cone 4 and the blue dashed line outlines cone 3.*

4.2 Volume of the cone complex

The volume of each cone was calculated using the equation from Kervyn et al (2012) and using a MATLAB script created by E. Llewellin (**table 4.1).** Using the four volumes calculated from the equation and geometric shape volumes for overlap, the DRE volume of scoria cone 4, with no cone overlap, is 5.3 x 10^7 m^3. Using the volumes calculated from the MATLAB script, the DRE volume of scoria cone 4, with no cone overlap, is 7.7 x 10^5 m^3.

The volume calculated by the equation is two orders of magnitude larger than the modelled volume. The first volume assumes that the sections of overlapping cone are geometric shapes (basic truncated cones and ellipsoids) which is highly unlikely, whilst the second volume takes into account the x, y, z points of each scoria cone in relation to cone 4 and uses this to identify the overlapping sections and their volumes. However, neither

take into account the breach seen on cone 4. Therefore, for the purpose of this study, the minimum DRE volume of scoria cone 4 is approximated to be 4.8 x 10^6 m^3.

	W_{co} (m)	W_{cr} (m)	D_{cr} (m)	H_{co} (m)	Volume 1 (m^3)	Volume 2 (m^3)
Cone 1	755	240	33	141	2.8 x 10^7	3.6 x 10^8
Cone 2	805	155	12	125	2.3 x 10^7	1.5 x 10^9
Cone 3	670	105	6	130	1.7 x 10^7	7.7 x 10^8
Cone 4	925	300	44	204	6.0 x 10^7	7.9 x 10^8

Table 4.1: *The dimensions of each scoria cone within the Sister's Scoria Cone Complex (including cone overlap). Dimensions taken from Google Earth. Volume 1 is the DRE volume calculated using the equation from Kervyn et al (2012) and volume 2 is the DRE volume calculated using the MATLAB script created by E. Llewellin.*

4.3 Tephra Fall Deposits

Four tephra fall deposits were identified in the field (Unit 1-4). Unit 1 is the oldest and Unit 4 is the youngest. The deposits were identified north and west of the cones. Detailed work was undertaken on Unit 3 as it was best preserved. Units 2 and 3 have been described at only a few localities: Unit 1 was not preserved well enough to describe the whole sequence. The classification of beds within the fall deposits is based on tephra componentry and visual grain size changes. Each unit has a number of recognisable beds identified within 1 km of the vent.

4.3.1 Unit 2

Unit 2 was described at one locality **(figure 4.4a, b).** Bed 1 has a base that cannot be seen. The layer is composed of a massive, ragged and platy, medium lapilli scoria with a blue iridescence. Bed 2 is a 0.5 cm thick, orange ash layer. Bed 3 is a layer of fine-medium

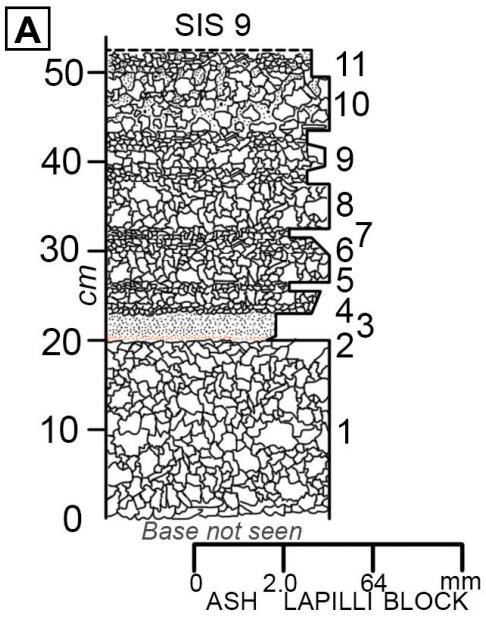

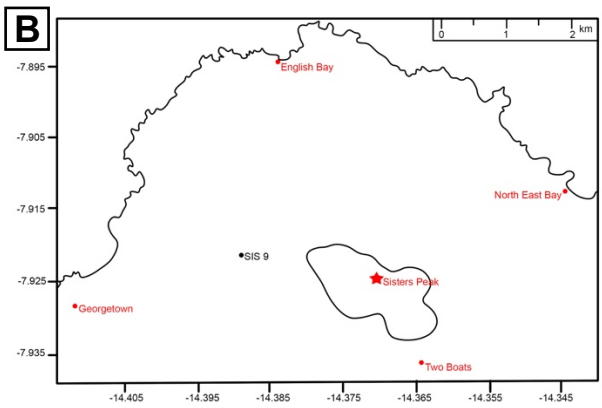

Figure 4.4: A) *Stratigraphic column of the Unit 2 fall sequence. Arrow shows direction away from the vent.* ***B)*** *Location map showing the north-west of Ascension Island, the outline of the Sisters Scoria cone complex and the location of the Unit 2 tephra fall deposit. Key places are marked in red.*

ash. Bed 4 is a normal graded, ragged and spinose, coarse lapilli scoria. Bed 5 is the same as bed 3. Bed 6 is similar to bed 4 but has an abundance of platy scoria. Bed 7 is a layer of dark grey, coarse ash. Bed 8 is a layer of angular, ragged-shaped, spinose and lustrous coarse lapilli scoria that lacks the abundance of ash seen in previous beds. Bed 9 is a layer of mirror graded, stratified, coarse lapilli scoria and abundant medium ash. Bed 10 is a layer of fine lapilli scoria and abundant ash. The lower half of the bed has greater pore space between ash particles due to a lower percentage of fine ash. Bed 11 is a layer of medium lapilli scoria and abundant ash with a strong orange coloured surface.

4.3.2 Unit 4

Unit 4 is the youngest scoria fall deposit from the SSCC and is composed of 15 recognisable beds **(figure 4.5a, b).** Bed 1 overlies a thin, poorly developed paleosol in the top of Unit 2. It is a 0.75 cm thick layer of medium ash containing lithic clasts of dense lava. Bed 2 is a layer of fine lapilli scoria with lithic clasts of dense lava. Bed 3 is the same as bed 1 but 0.5 cm thick. Bed 4 is a layer of massive, inverse-graded, fine lapilli to coarse ash containing dark grey lava lithic clasts. Bed 5 is a 0.5 cm thick layer of fine-medium ash and dense lava lithic clasts. Bed 6 is a layer of inverse to normal graded medium lapilli scoria.

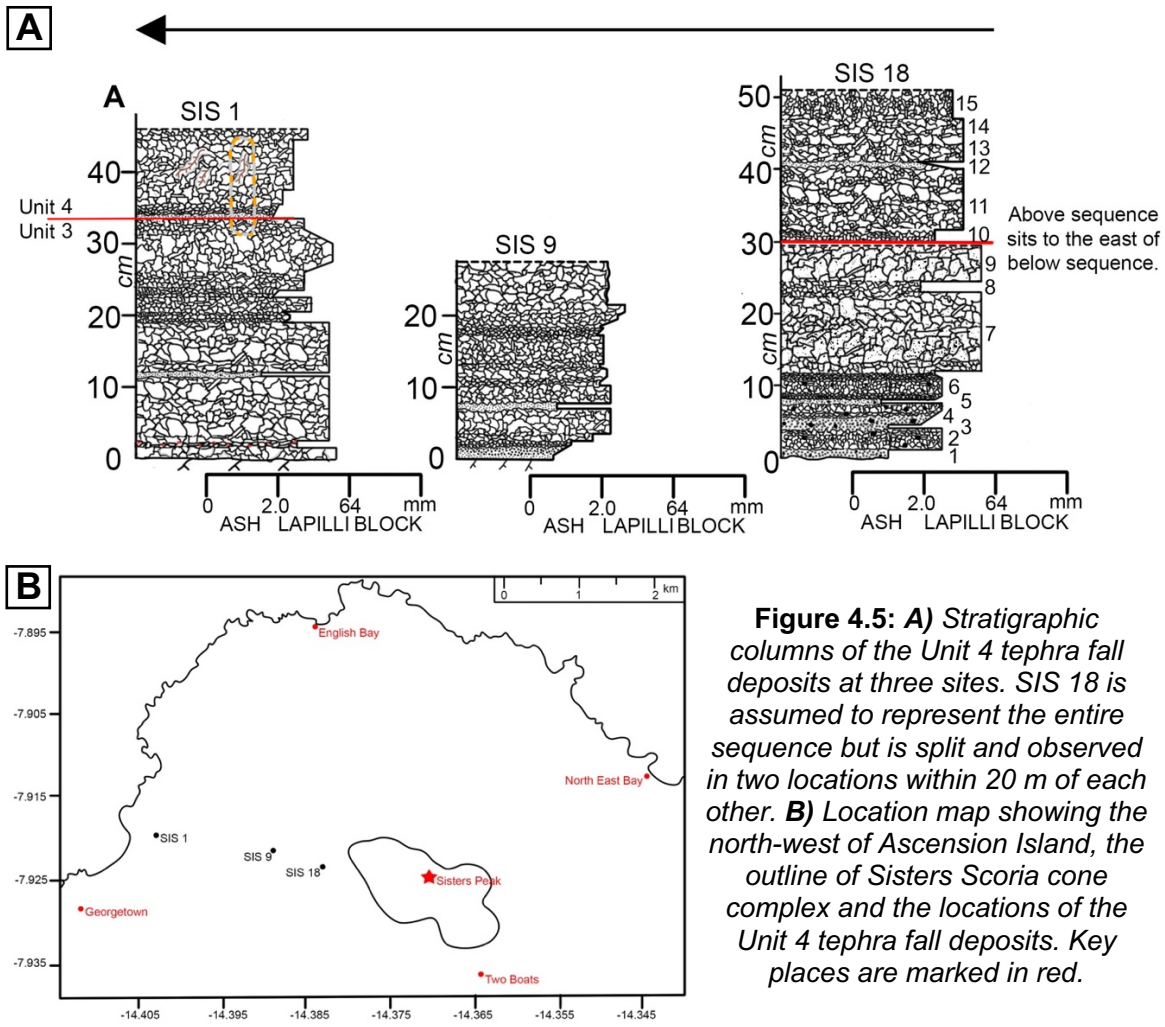

Figure 4.5: ***A)*** *Stratigraphic columns of the Unit 4 tephra fall deposits at three sites. SIS 18 is assumed to represent the entire sequence but is split and observed in two locations within 20 m of each other.* ***B)*** *Location map showing the north-west of Ascension Island, the outline of Sisters Scoria cone complex and the locations of the Unit 4 tephra fall deposits. Key places are marked in red.*

The bed is composed of lustrous black, ragged and vesicular scoria and dark grey lava lithic clasts. Bed 7 is composed of coarse lapilli scoria. The top and bottom scoria layer has yellow/brown staining on the exterior but black centres. The middle layer scoria is black and vesicular. Bed 8 is composed of platy, equant and 'ash coated' scoria. Bed 9 is similar to bed 7 but without the colour bands. Bed 10 is a layer of fine-medium lapilli scoria. Bed 11 is a layer of massive, poorly-sorted, ragged and platy-shaped fine lapilli scoria and abundant coarse ash. At SIS 1 the bed contains abundant fine roots and flakes of white precipitate. Bed 12 is a very thin, 1 cm thick, layer of medium-coarse ash and fine-grained soil. Bed 13 and bed 14 are the same as bed 11. Bed 15 is a layer of ragged and platy, fine-medium lapilli scoria and abundant ash. Angular, dark grey, reworked material is observed towards the top of the bed.

4.3.3 Unit 3

The thickest outcrop (SIS 51) is located in the proximal sector and contains three distinguishable subunits that can be further split into 15 beds **(figure 4.6a, b)**. The lower subunit has a maximum thickness of 182 cm and is composed of 4 beds. The first is a layer of black, red lithic clast poor, massive, coarse lapilli scoria. The second is similar to the first with <1 wt.% yellow scoria lithic clasts and rare red lithic clasts (2-6 mm). The third is also similar, with <1 wt.% red lithic clasts (2-6 mm). The fourth is a 3 cm layer of coarse ash to fine lapilli. The lower subunit is best preserved in outcrops behind and right of the dispersal axis (SIS 27). The middle subunit has a maximum thickness of 92 cm and is composed of **8** beds. The first is a layer of well sorted, weakly bedded, coarse lapilli scoria. The second is the same as the first but composed of medium lapilli scoria. The third is a layer of ragged and vesicular fine lapilli to coarse ash. The fourth is a layer of massive, equant, 'ash-coated', coarse lapilli scoria. The fifth, sixth and seventh are a sequence of a layer of massive, coarse ash, a layer of fine lapilli to coarse ash and a layer of stratified, coarse ash. These beds are defined as marker horizons. The eighth is a layer of medium lapilli scoria with bands of blue, iridescent-coated clasts. Behind and to the right of the dispersal axis, the section is composed of, up to 3, alternating beds of medium lapilli scoria and coarse ash. The upper subunit has a maximum thickness of 80 cm and is composed of 3 beds. The first is a diffusely stratified, poorly sorted, fine-medium lapilli scoria with 1 cm layers alternating between ragged-shaped, black scoria and equant, 'ash-coated' scoria. The second is a 4 cm thick layer of fine-medium lapilli scoria. The third is similar to the first but with well-defined layers. The third section occurs at proximal sector left of the dispersal axis but is absent behind and to the right (SIS 27, SIS 28, SIS 32, SIS 34 and SIS 43).

In the medial sector the thickest sequence is SIS 18 **(figure 4.6a, b)**, located 1.34 km from the vent. The lower subunit has a maximum thickness of 23 cm and is composed of 2 beds with layers of well-sorted, ragged-shaped, coarse lapilli scoria and 5 wt.% red

lithic clasts. Away from SIS 18, the outcrops consist of single beds with layers of massive, well sorted, ragged, medium-coarse lapilli scoria and <3 wt.% red lithic clasts. The single layer of ash fines, then disappears, making it difficult to distinguish the top of section one from the base of section 2. The middle subunit has a maximum thickness of 84 cm and is composed of 7 beds. The first and third are layers of well sorted, vesicular, coarse lapilli scoria, separated by a layer of ragged, coarse ash. The fourth is the marker horizon; a sequence of poorly sorted, fine lapilli – coarse ash, overlain by a layer of fine lapilli scoria. The fifth is a well sorted, equant and 'ash-coated' medium lapilli scoria. Away from SIS 18, the coarse lapilli scoria beds thin to 1 cm thick, and the ash layers taper out. The marker horizon layers are well preserved to the left of the dispersal axis but absent to the right.

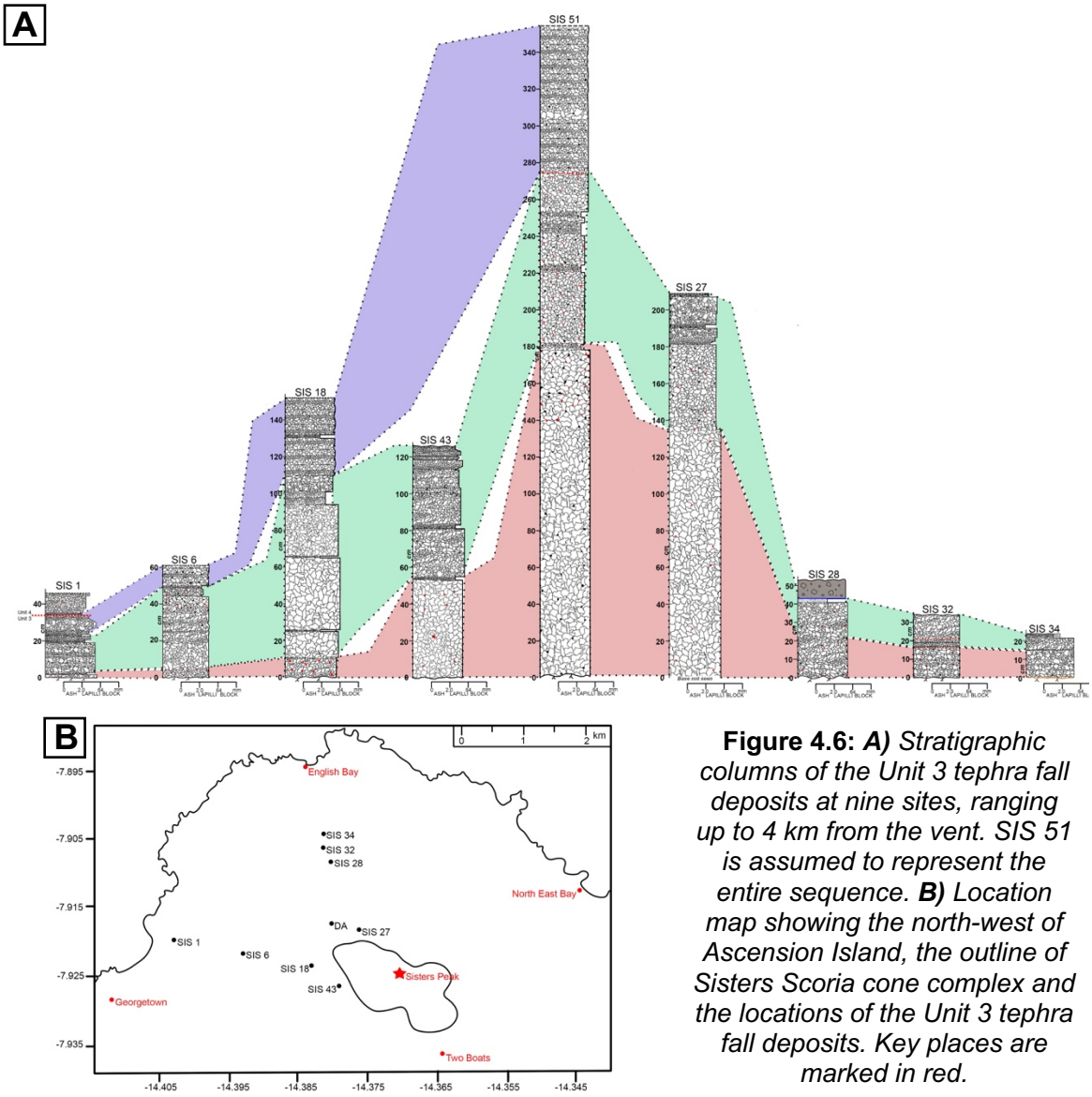

Figure 4.6: ***A)*** *Stratigraphic columns of the Unit 3 tephra fall deposits at nine sites, ranging up to 4 km from the vent. SIS 51 is assumed to represent the entire sequence.* ***B)*** *Location map showing the north-west of Ascension Island, the outline of Sisters Scoria cone complex and the locations of the Unit 3 tephra fall deposits. Key places are marked in red.*

The upper subunit reaches 41.8 cm **(figure 4.6a, b)**. The largest sequence is composed of 3 beds. The first is a layer of diffusely stratified, medium lapilli scoria, with <1 cm bands of coarse ash. The second is a 1.8 cm layer of coarse ash. The third is another

diffusely stratified bed. Away from SIS 18, the diffusely stratified beds and the ash layer are reduced to one stratified bed and then absent.

The lower and upper subunits are absent in the distal sector. The middle subunit is up to 10 cm thick. The single beds are composed of ragged, fine lapilli scoria and coarse ash. The abundance of red lithic clasts varies but are more abundant to the right of the dispersal axis.

4.4 Unit 3 Tephra Fall Deposit

4.4.1 Study Sites

Samples were taken from locality SIS 51 as a proximal deposit and SIS 6 as a medial deposit. These localities were chosen as they best represent the whole of Unit 3. Locality SIS 51 is 1.5 km from the vent and on the dispersal axis **(figure 4.7a)**. Locality SIS 6 is 2.6 km west of the vent **(figure 4.7b)**.

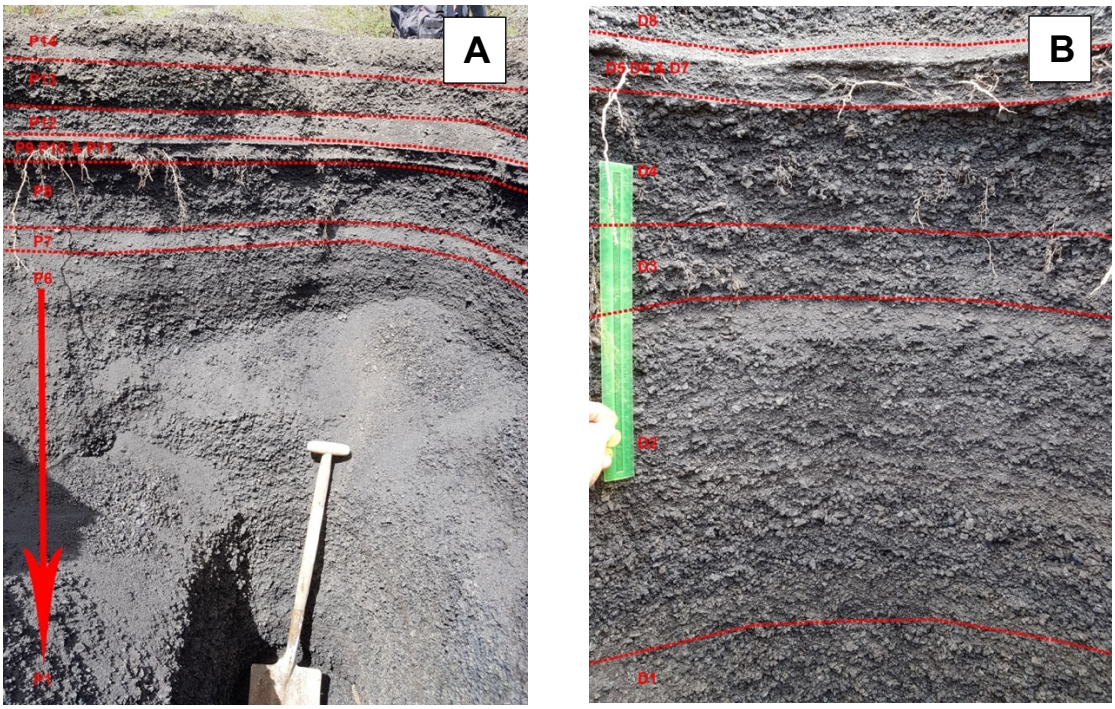

Figure 4.7: ***A)*** *Photograph of the SIS 51 sequence in the field. Shovel for scale* ***B)*** *Photograph of the SIS 6 sequence in the field. Ruler for scale.*

4.4.2 Componentry

Three different types of pyroclasts have been identified in Unit 3 based on the textural criterion, shape, colour and vesicularity (Eychenne and Pennec, 2012). The types represent two distinct end members and a transitional type. Two different types of accidental lithic clasts were also identified.

Type 1 **(figure 4.8a*)*** pyroclasts have a dull grey/brown colour and a granular surface, where clasts of lithics or ash, up to 2 mm, are stuck onto the surfaces. The clasts

are equant and platy and <8 mm in diameter. Their exteriors are often wrinkled or folded. There are <3 vol% vesicles visible to the naked eye.

Type 2 **(figure 4.8b)** pyroclasts are black with a glassy, iridescent skin. The clasts are prolate and fluidal shaped with jagged edges. The skin is spinose and has stretched filaments. In some cases, individual filaments are identifiable but in others the filaments have coalesced. The skin has <2 vol.% vesicles visible to the naked eye.

Type 3 **(figure 4.8c)** pyroclasts have a golden-brown colour with patches of dark brown, and range in shape from fluidal and stretched to equant and sub-angular. These clasts are moderately to highly vesicular.

Lithic clasts **(figure 4.8d)** are dense, mostly lava and range in shape from sub-rounded and equant to angular. They are dark grey and have smooth surfaces. They are incipiently to non-vesicular with <6 vol.% of sub-rounded vesicles or cavities. Feldspar microlites, <0.5 mm long, are seen in the groundmass.

Oxidised lithic clasts **(figure 4.8d)** are sub-rounded and equant clasts. The colour ranges from a pale red to a dark orangey-red and the surfaces are smooth. They are incipiently vesicular with <10 vol.% sub-rounded/sub-elongate vesicles or cavities. The groundmass is aphanitic.

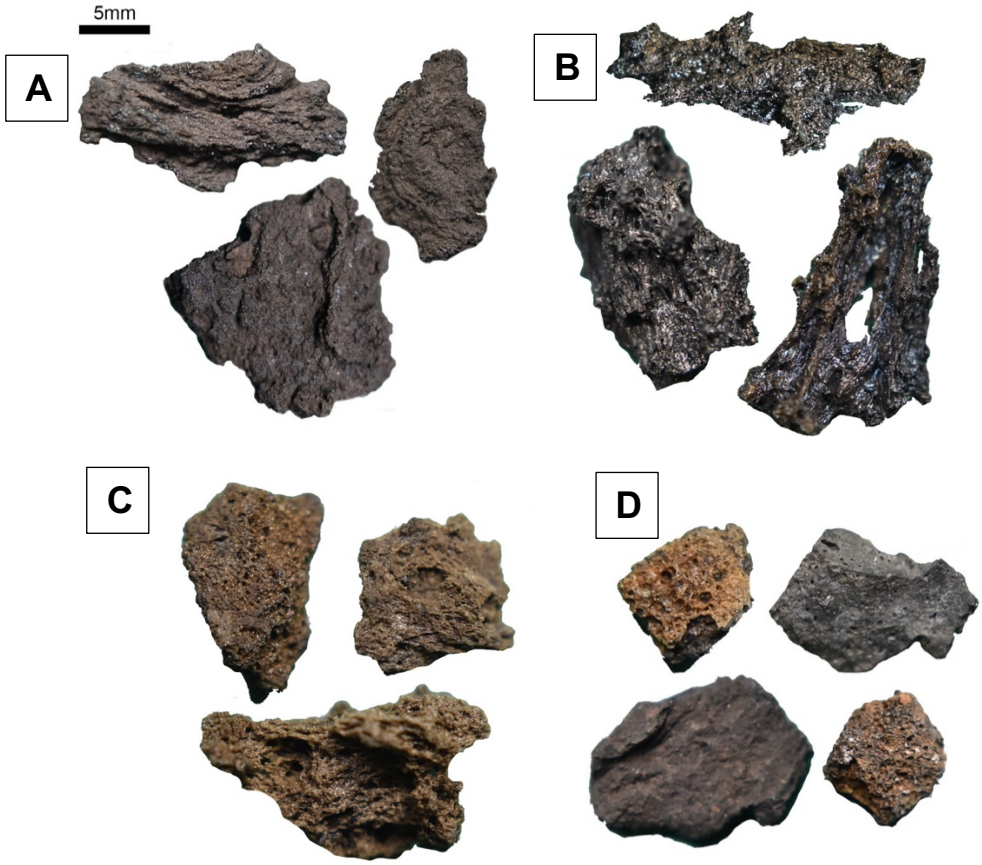

Figure 4.8*: Close up images of the different clast morphologies.* ***A)*** *Type 1.* ***B)*** *Type 2.* ***C)*** *Type 3.* ***D)*** *Lithic clasts and oxidised lithic clasts.*

The abundance of each group varies throughout the beds **(figure 4.9a, b).** Types 1 and 2 are the dominant groups and are identified in all measured size fractions of each bed. Type 2 and 3 are most abundant in the lower beds and as the sequence progresses type 1 increases in abundance. At both locations, the type 2 clasts are the most abundant within the sequence.

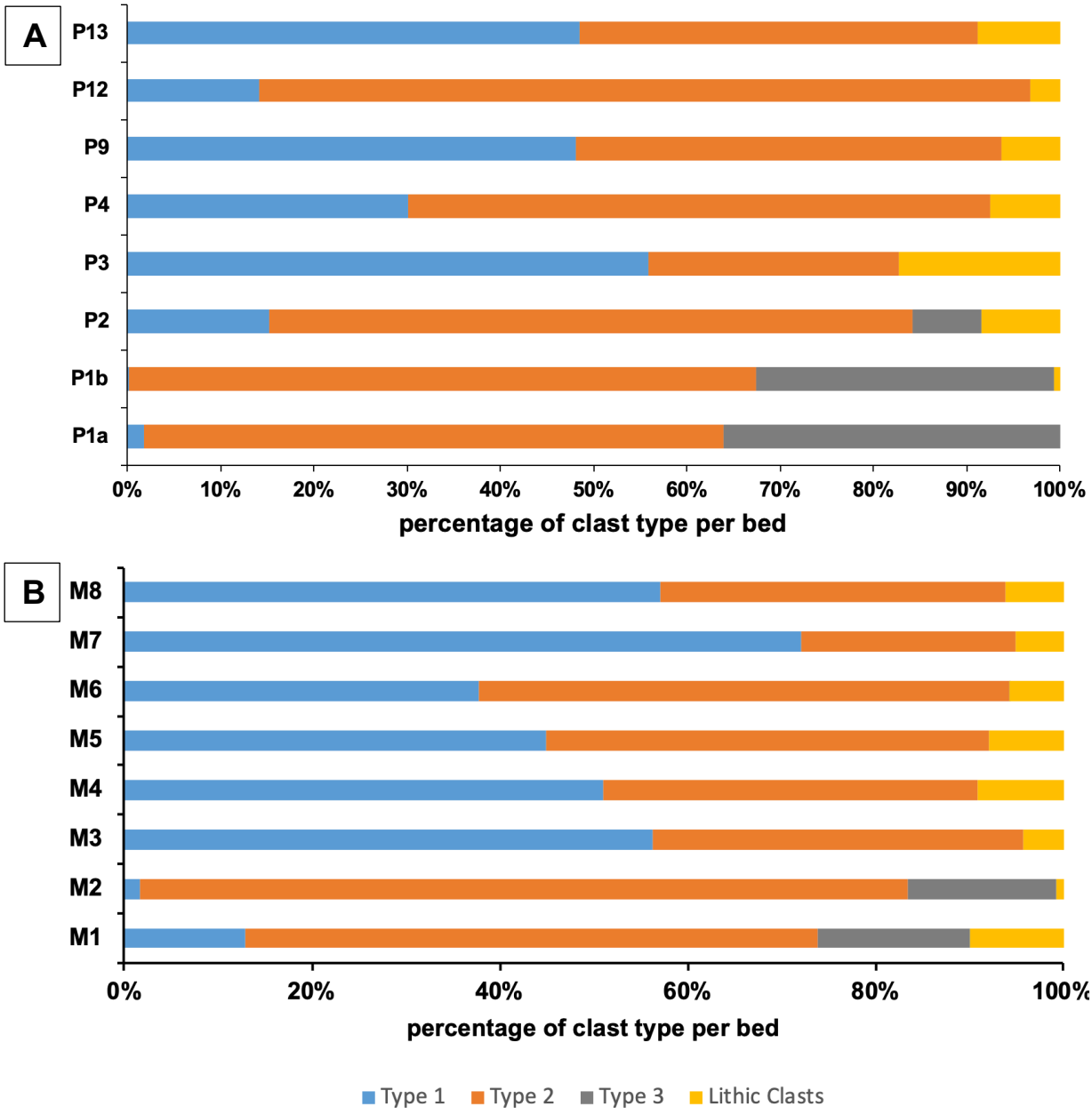

Figure 4.9: *Graphs showing the distribution of clast groups throughout the beds.* ***A)*** *Proximal deposit (SIS 51).* ***B)*** *Distal deposit (SIS 6). n = 500 for each bed.*

4.4.2.1 Proximal Deposit

Type 1 clasts are seen in all beds and size fractions and increase in abundance up sequence from 0.2 wt.% to 55.9 wt.% **(figure 4.10a,b)**. The beds with the greatest abundance are P3 (55.9 wt.%) and P13 (48.5 wt.%). Between P1b and P2 there is a sharp increase in abundance, from 0.2 wt.% to 15.2 wt.% and up sequence the abundance

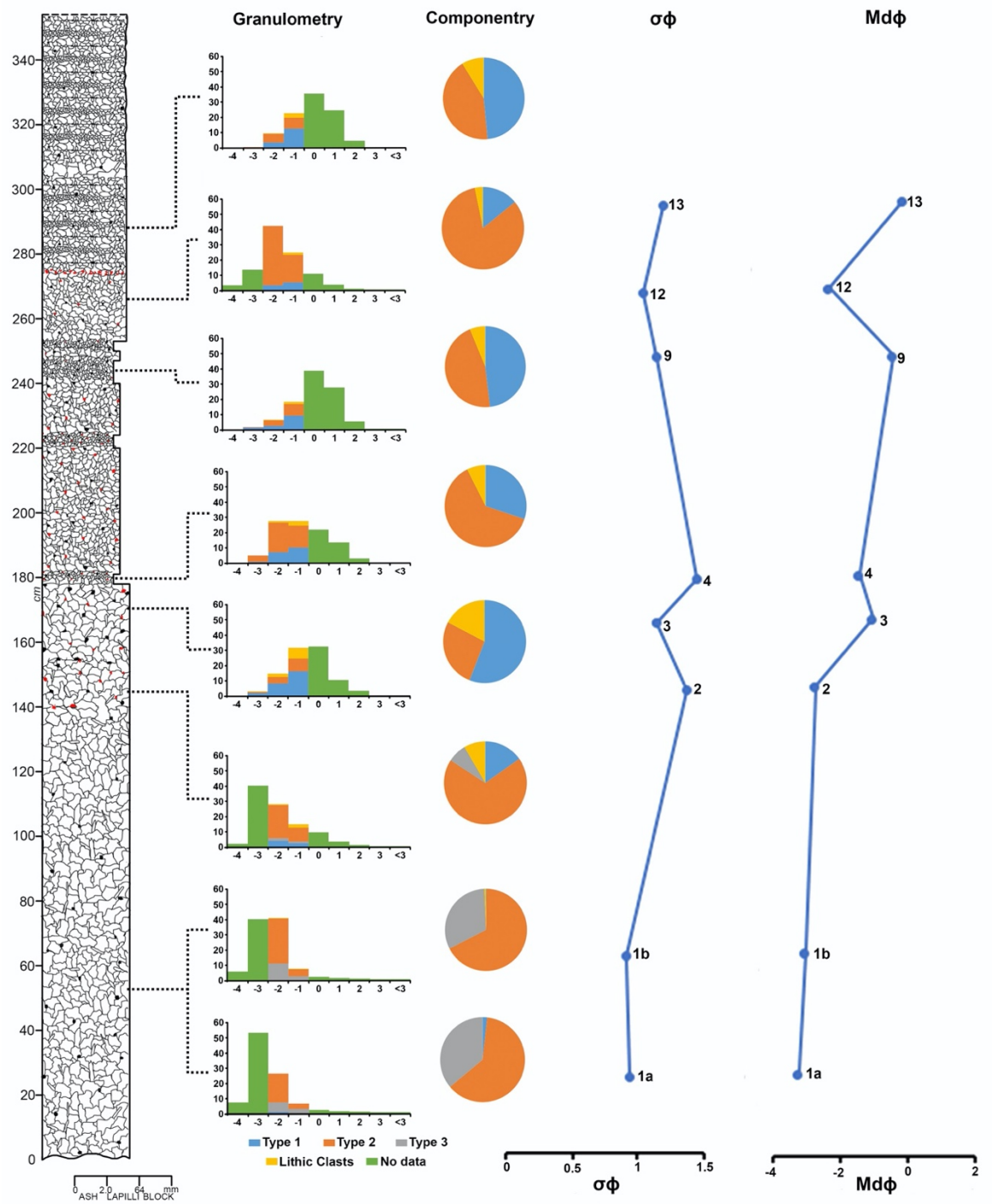

Figure 4.10: A) *Stratigraphic column from locality SIS 51.* ***B)*** *Bar chart shows grain size and percentage of each type per size fraction.* ***C)*** *Pie chart shows the total percentage of each type per bed (n = 500).* ***D)*** *Line graph showing* σ_ϕ. ***E)*** *Line graph showing* Md_ϕ.

fluctuates between 15.2 wt.% (P2) and 55.9 wt.% (P3). Type 2 clasts are also seen in all beds and size fractions, and the abundance fluctuates up sequence from 28.8 wt.% (P3) and 82. 7 wt.% (P12). The most abundant beds are P12 and P2 at 82.7 wt.% and 69.0 wt.%. There is no structure to the distribution of the clasts throughout the sequence but, as the abundance of type 1 clasts increase, the abundance of type 2 clasts decreases. Type 3 clasts are seen in beds P1a, P1b and P2 and size fractions smaller than -3ϕ. The most abundant bed is P1 with the lower section (P1a) having the highest abundance at 36.1 wt.% and P2 has the lowest abundance at 7.4 wt.%. Red and grey lithic clasts are found in all

beds except P1a and in size fractions smaller than 2ϕ. The abundance ranges between 0.6 wt.% (P1b) and 17.3 wt.% (P3). There is a weak correlation between type 1 pyroclasts and lithic clasts: as the abundance of type 1 clasts increase, the abundance of lithic clasts also increases.

4.4.2. Medial Deposit

Type 1 clasts are seen in all the beds and size fractions and increase in abundance up sequence from 1.7 wt.% to 72 wt.% **(figure 4.11a,b)**. The most abundant beds are M7 and M8 at 72.0 wt.% and 57.1 wt.%. At M3 there is a sharp increase in the abundance of type 1 clasts, from 1.7 wt.% to 56.3 wt.% and up sequence the abundance fluctuates between 37.7 wt.% (M6) and 72.0 wt.% (M7). Type 2 clasts are also seen in all the beds and size fractions but decrease in abundance up sequence from 81.7 wt.% to 22.8 wt.%. The most abundant beds are M1 and M2 at 61 wt.% and 81.7 wt.%. At M3 there is a sharp decrease to 39.5 wt.% and up sequence the abundance fluctuations between 22.8 wt.% (M7) and 56.3 wt.% (M6). Type 3 clasts are only seen in beds M1 and M2 and in all size fractions. They show a slight decrease in abundance from 16.2 wt.% to 15.9 wt.%. Lithic clasts are found in each bed and in size fractions smaller than -2ϕ. The abundance ranges from 0.7 wt.% (M2) to 10 wt.% (M1). The lithic clasts exhibit the same weak correlation seen in the proximal deposit.

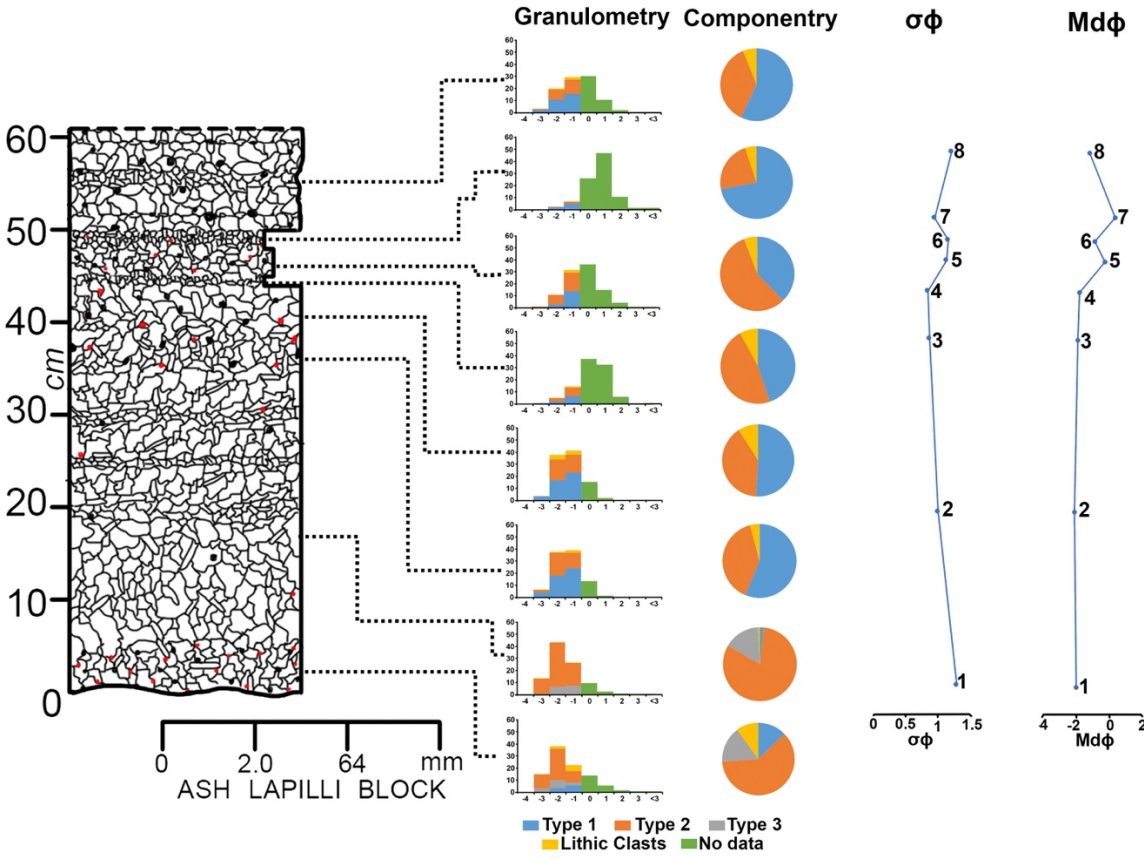

Figure 4.11: A) *Stratigraphic column from locality SIS 51.* ***B)*** *Bar chart shows grain size and percentage of each type per size fraction.* ***C)*** *Pie chart shows the total percentage of each type per bed (n = 500).* ***D)*** *Line graph showing* σ_ϕ. ***E)*** *Line graph showing* Md_ϕ.

4.4.3 Petrography

Pyroclasts – Type 1

The type 1 pyroclasts clasts appear halfway through the sequence and increase in abundance upwards. The clasts are equant and up to 16 mm in diameter, with irregular edges. Their surfaces are characterised by a rough skin, 26 µm thick **(figure 4.12a)**, which covers a vesicular interior. Surface mounds and elongate ridges form over vesicles **(figure 4.12b)**. Individual vesicle walls are not distinguishable.

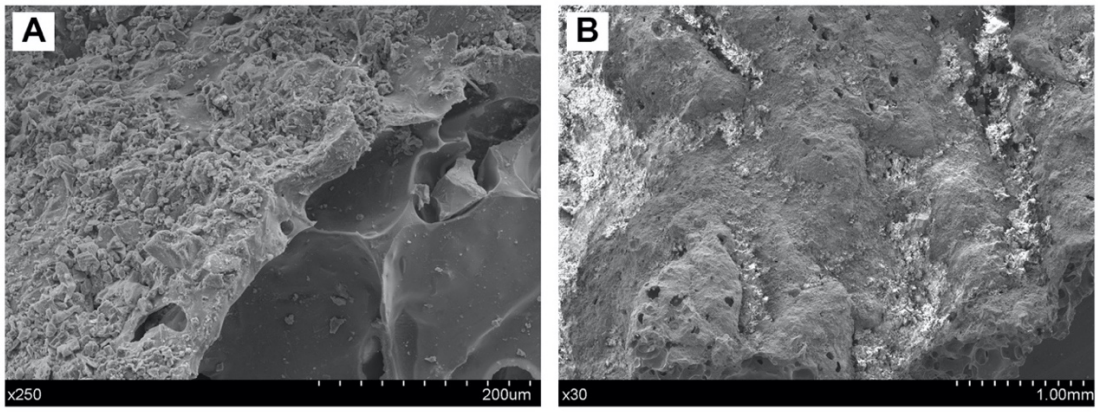

Figure 4.12: *BSE images of the surface features of the Type 1 pyroclasts.* ***A)*** *Rough and irregular skin covering a vesicular interior.* ***B)*** *Surface mounds and ridges.*

Type 1 pyroclasts range from moderately vesicular to highly vesicular (~55-75%) (vesicle classification based on Houghton and Wilson (1989)). Vesicles are randomly distributed, elongate and irregular shaped with the largest vesicles (<1400 µm in diameter) at their centres **(figure 4.13a)**.

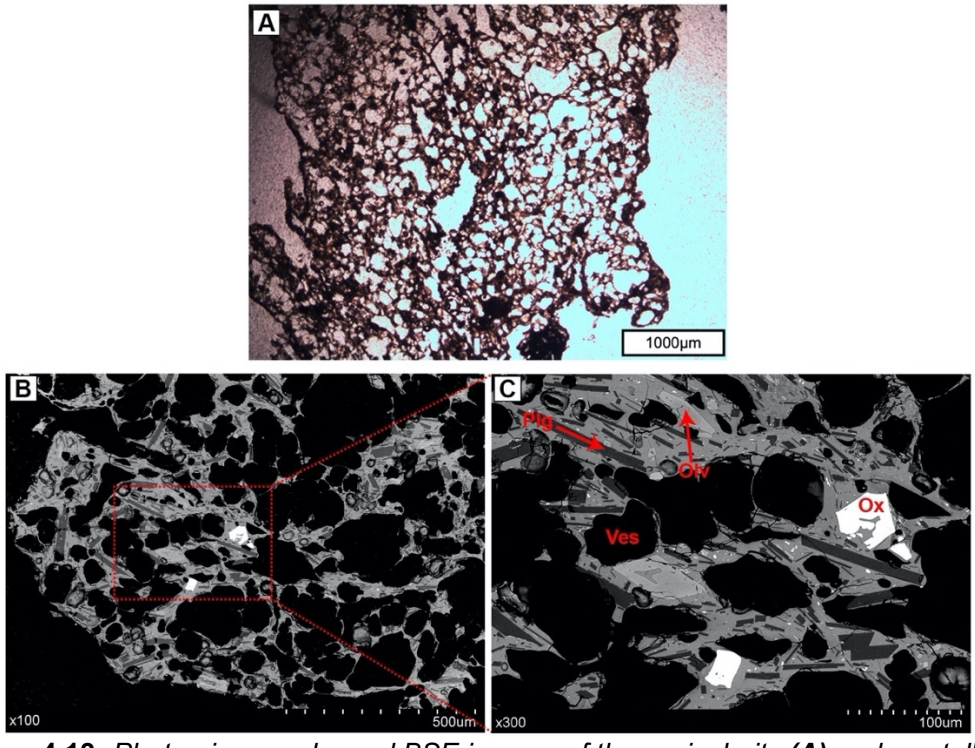

Figure 4.13: *Photomicrographs and BSE images of the vesicularity* ***(A)*** *and crystallinity* ***(B,C)*** *of the Type 1 pyroclasts.*

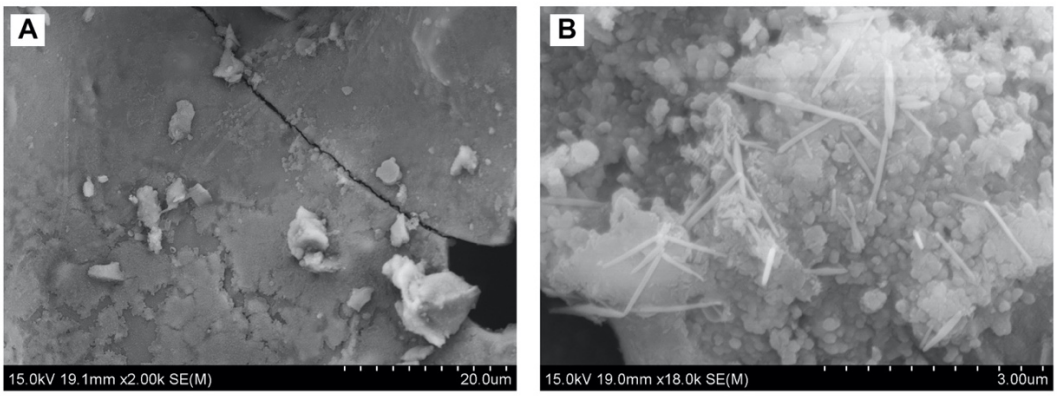

Figure 4.14: *SEM images of the surface precipitates.* ***A)*** *Extremely fine precipitates covering the entire surface of the pyroclasts and larger, individual precipitates.* ***B)*** *Spherical and needle-like precipitates layered on top of each other.*

The surfaces of the clasts are covered in fine (<1 μm in diameter) spherical and sub-spherical precipitates **(figure 4.14a)**. Most stand out from the surface of the clasts, but in some areas, they have been flattened onto the surface. On top of the smaller precipitates are larger (1-10 μm in diameter) spherical or needle-like clusters **(figure 4.14b)**. Larger surface precipitates (10-20 μm in diameter) are angular, platy or spherically shaped.

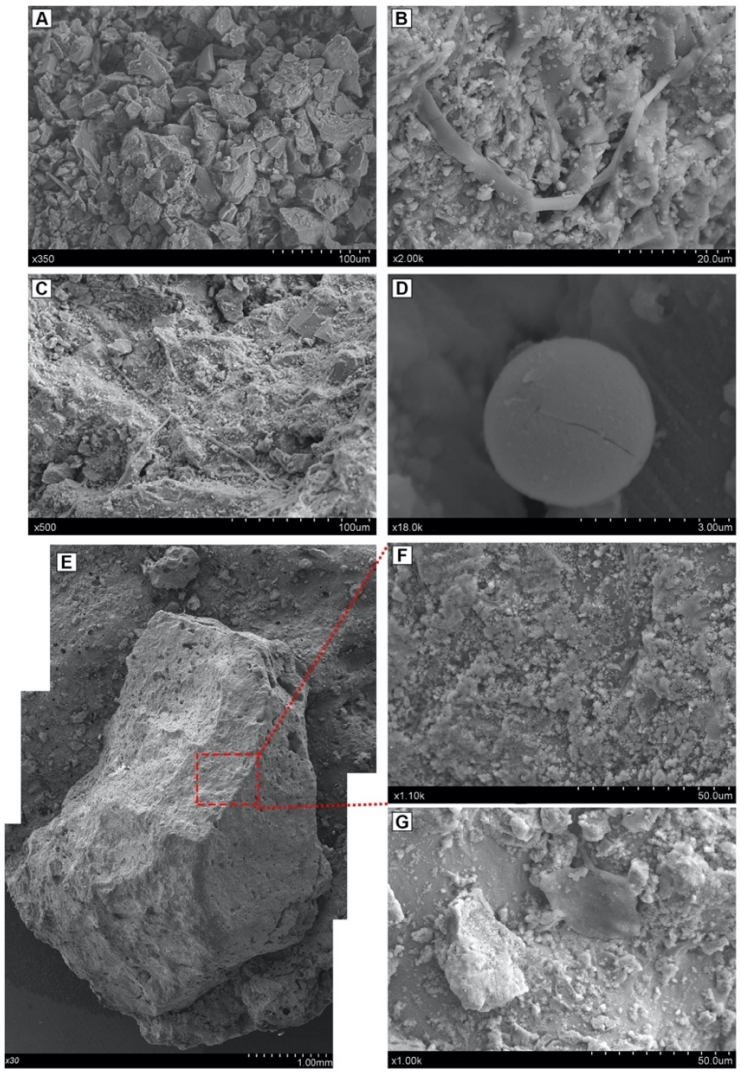

Figure 4.15: *SEM images of the adhered particles on the surface.* ***A)*** *Surface of the clasts heavily covered in ash particles.* ***B, C)*** *Pele's hair, elongate and semi-rigid with multiple branches.* ***D)*** *Spherical lava droplet.* ***E, F)*** *Attached lithic clasts and the precipitate covering on the surface* ***G)*** *Adhered clasts with precipitate coating.*

Particles of glass shards, Pele's hair, lava droplets, lithic clasts and precipitates are accreted to ~90 area% of the surface **(figure 4.15a)**. The glass shards are angular and <60 μm in diameter. The surfaces are irregular with adhered particles. Pele's hair area <150 μm long and <10 μm wide. They range in shape, from cylindrical and thread like to elongate and semi-rigid **(figure 4.15b,c)**. The glass strands form multiple branches, and beads (<5 μm in dimeter) form at intervals along them. The surfaces are smooth with rare adhering precipitates. Spherical droplets are rare and <5 μm. Most are fully intact with smooth surfaces, but few have partially cracked surfaces **(figure 4.15d)**. Clasts of different compositions (up to 5000 μm in diameter) are crystalline and vesicular. These clasts are covered by a thicker precipitate layer with angular and spherical clusters up to 5 μm in diameter **(figure 4.1e,f)**. ~80 area% of the adhered clasts have needle-like and sub-spherical precipitate clusters on their surfaces **(figure 4.15g)**.

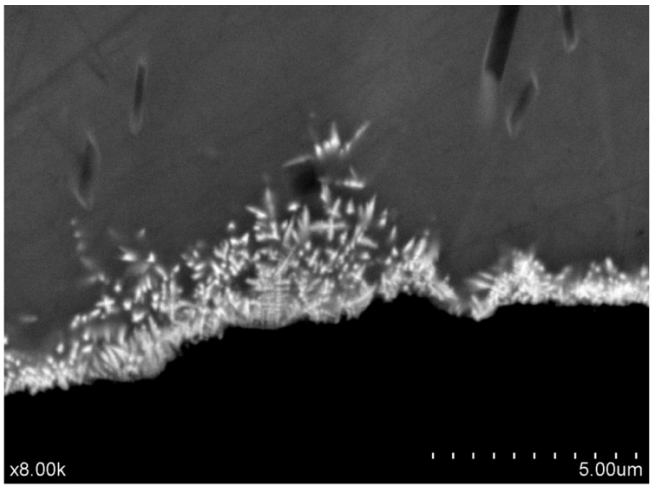

Figure 4.16: *BSE image of dendritic Fe-Ti oxides along the exterior of the clasts.*

Type 1 clasts show two textural domains. In the first, the groundmass is hypocrystalline, medium-dark brown sideromelane glass **(figure 4.13b,c)**. Microlitic crystals range up to 80 μm in diameter and comprise of in order of decreasing abundance, plagioclase, olivine and Fe-Ti oxides. The exteriors of the clasts contain dendritic Fe-Ti oxides <1 μm long **(figure 4.16)**. The second makes up 10-15 area% of the clasts. The groundmass is cryptocrystalline, tachylite-like glass. This domain can be further split into three textural types:

(1) Subhedral skeletal or tabular plagioclase with rare, subhedral olivine crystals and Fe-Ti oxides microphenocrysts. The microcrystalline groundmass consists of plagioclase, olivine, clinopyroxene, and Fe-Ti oxides **(figure 4.17a,b)**.

(2) Subhedral acicular or tabular plagioclase microphenocrysts. The microcrystalline groundmass consists of rare olivine and abundant sub-rounded Fe-Ti oxides **(figure 4.17c,d)**.

(3) Subhedral acicular, tabular or swallow tail plagioclase, rare subhedral microphenocrysts. The microcrystalline groundmass consists of plagioclase, olivine and abundant, dendritic Fe-Ti oxides **(figure 4.17e,f)**.

The contact between the two domains is sharp and defined by Fe-Ti oxide bands, <1 μm in diameter.

The crystal content is ~45 area%. Individual plagioclase crystals are most common (~20 area%), followed by individual olivine crystals (~5 area%). Glomerocrysts of olivine and plagioclase are rare. Both mineral phases contain inclusions of Fe-Ti oxides and/or volcanic glass.

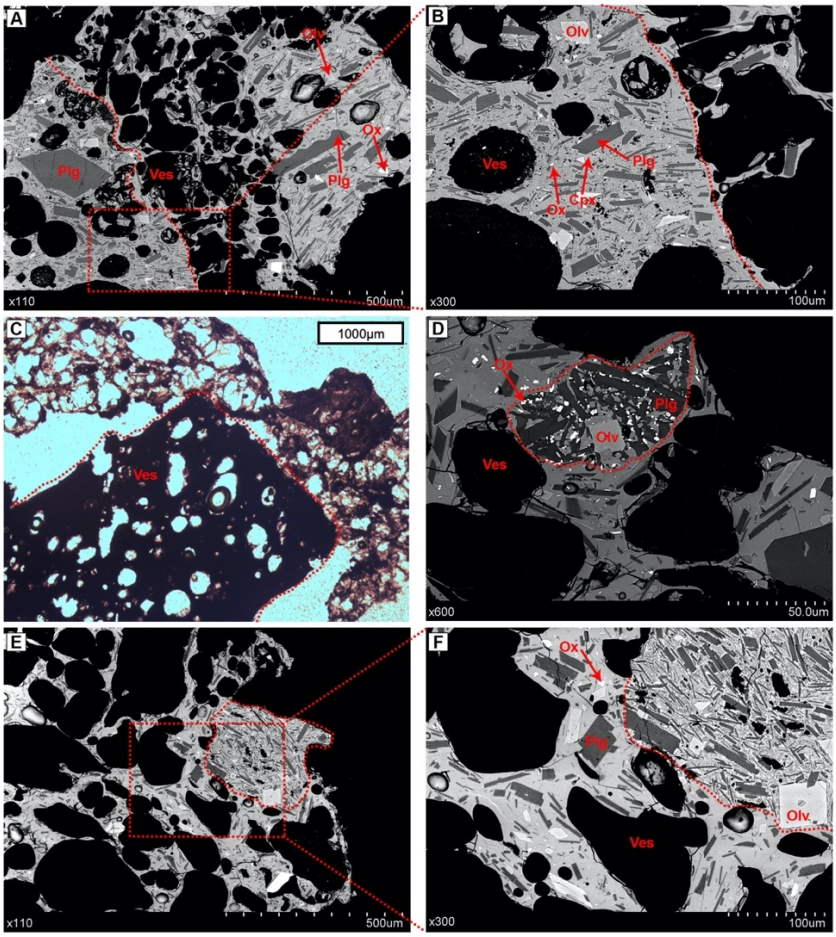

Figure 4.17: *BSE images of the cryptocrystalline domains. Red dashed lines outline the boundary between the cryptocrystalline and hypocrystalline domains **A,B)** Cryptocrystalline domain 1. **C,D)** Cryptocrystalline domain 2. **E,F)** Cryptocrystalline domain 3.*

Pyroclasts – Type 2

The type 2 pyroclasts are found throughout the fall deposit but occur in greater abundance in the lower and middle subunits. The clasts are typically prolate and up to 16 mm long, with ragged edges. Their surfaces are characterised by a fluidal, thin, glassy skin that covers a vesicular interior **(figure 4.18a)**. Surface mounds and elongate ridges form over vesicles **(figure 4.18b)**. Vesicle walls are up to 600 μm thick **(figure 4.18c)**.

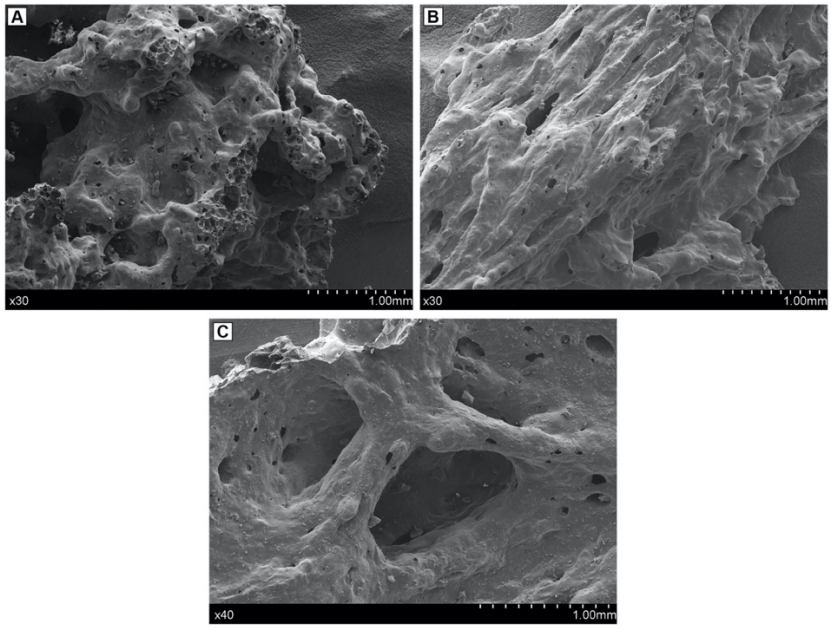

Figure 4.18: *SEM images of the surface features of the type 2 pyroclasts.* ***A)*** *Fluidal, glassy skin.* ***B)*** *Surface mounds and elongate ridges over vesicles.* ***C)*** *Vesicle walls.*

Type 2 pyroclasts range from poorly vesicular to extremely vesicular (~35-85%) **(figure 4.19a-c)**. The highly vesicular clasts show heterogeneous vesicularities with small, sub-rounded vesicles (<500 μm in diameter) in their rims and larger, irregular vesicles

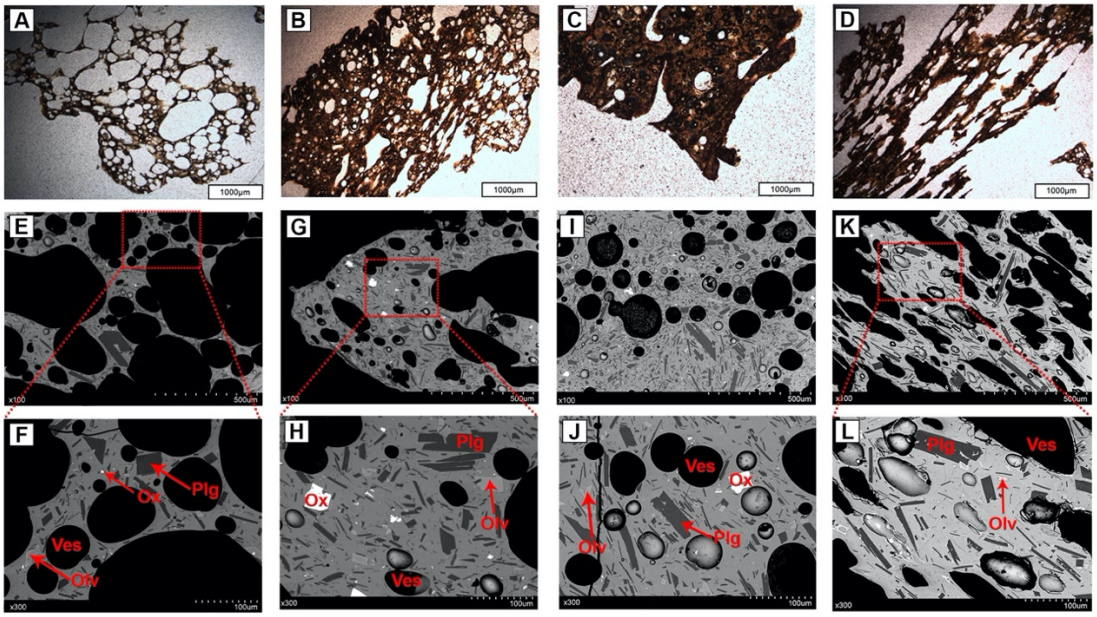

Figure 4.19: *Photomicrographs and BSE images showing vesicularity and crystallinity of type 2 tephra.* ***A)*** *Extremely vesicular clasts.* ***B)*** *Moderately vesicular clasts.* ***C)*** *Poorly vesicular clasts.* ***D)*** *Stretched, elongate vesicle clasts.* ***E, F)*** *Crystal distribution for the extremely vesicular clasts.* ***G, H)*** *Crystal distribution for the moderately vesicular clasts.* ***I, J)*** *Crystal distribution for the poorly vesicular clasts.* ***K, L)*** *Crystal distribution for the stretched vesicle clasts. Red boxes highlight areas representing respective x300 magnification images.*

(<1300 μm in diameter) in their centres. The poorly vesicular clasts also show heterogeneous vesicularities with small, rounded vesicles (<100 μm in diameter) in their

rims and centres with very few, larger, irregular vesicles (<1000 μm in diameter) in their centres. Prolate clasts have stretched vesicles (<500 μm in diameter) towards the centre **(figure 4.19d)**.

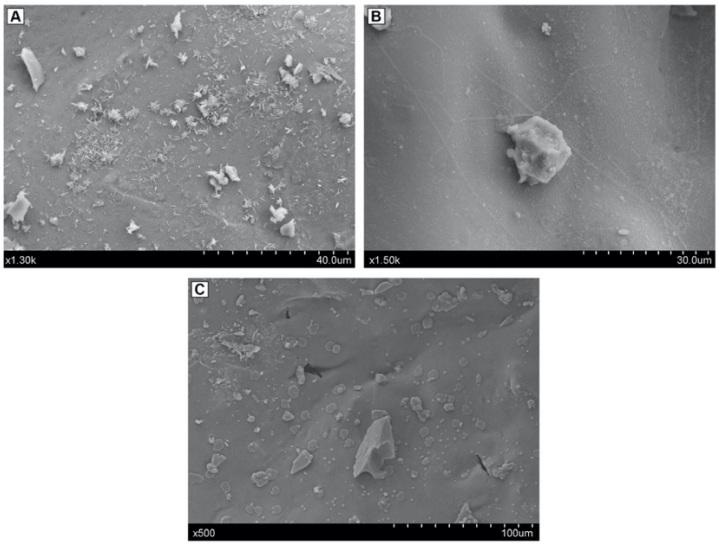

Figure 4.20: *SEM images of the surfaces of the type 2 clasts.* ***A)*** *Spherical and needle-like precipitates* ***B)*** *Spherical precipitate trails* ***C)*** *Angular, platy and spherical droplets attached to the surfaces.*

The surfaces of the clasts are covered in fine (<1-5 μm in diameter) spherical, needle-like clusters and rod-like precipitates **(figure 4.20a)**. Most stand out from the surface of the clasts, but in some areas, they have been flattened onto the surface. Trails of spherical precipitates (up to 2 μm thick) migrate from precipitate rich centres **(figure 4.20b)**. Larger surface precipitates (1-15 μm in diameter) are angular, platy or spherically shaped **(figure 4.20c)**.

Particles of glass shards, Pele's hair, lava droplets and precipitates are accreted to ~25 area% of the surface. The glass shards are angular and <50 μm in diameter. Pele's hair are <100 μm long and <10 μm wide **(figure 4.21a)**. Their surfaces are smooth with few adhering particles. Spherical droplets are rare and <10 μm in diameter with no adhering particles. ~40 area% of the adhered clasts have needle-like and sub-spherical precipitates attached to their surface **(figure 4.21b,c)**. These precipitates differ from those found on the type 1 clast surfaces.

Type 2 clasts show two different textural domains **(figure 4.22)**. In the first, the groundmass is hypocrystalline, pale brown, sideromelane glass**.** Microlitic crystals range up to 100 μm in diameter and comprise of, in order of decreasing abundance, plagioclase, olivine and Fe-Ti oxides. The exteriors of the clasts contain dendritic Fe-Ti oxides, <1 μm long. The second makes up <10 area% of the clasts. The groundmass is cryptocrystalline, dark brown-black, tachylite-like glass. Microlitic crystals range up to 200 μm in diameter and comprise of, in order of decreasing abundance, plagioclase, olivine, clinopyroxene and Fe-

Ti oxides. The contact between the crystalline and hypocrystalline clasts is a narrow, <1 μm, dendritic Fe-Ti oxide bands.

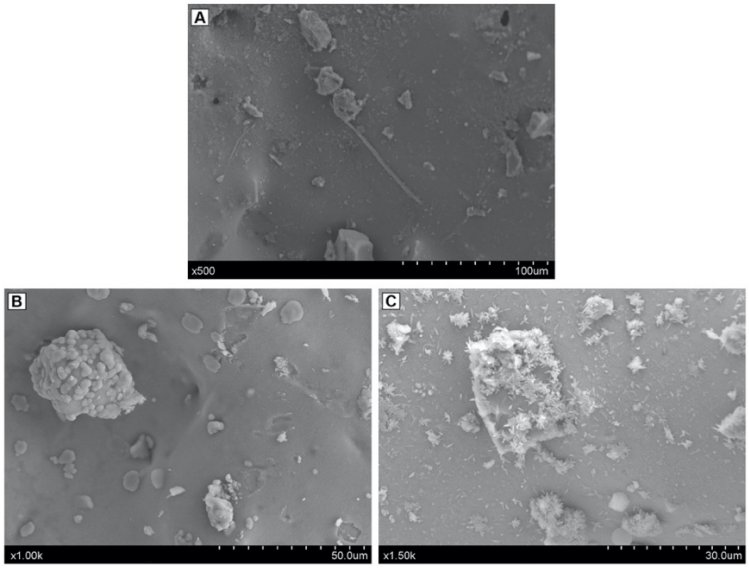

Figure 4.21: *SEM images of the adhered clasts.* ***A)*** *Pele's hair adhered to the surface.* ***B)*** *Precipitates adhered to the surface.* ***C)*** *Adhered ash clast coated in needle-like precipitates.*

The crystal content is ~35 area% **(figure 4.19e-l)**. Individual plagioclase crystals are most common (~15 area%), followed by individual olivine crystals (~3 area%). Glomerocrysts of olivine and plagioclase are rare. Both mineral phases contain inclusions of Fe-Ti oxides and/or volcanic glass.

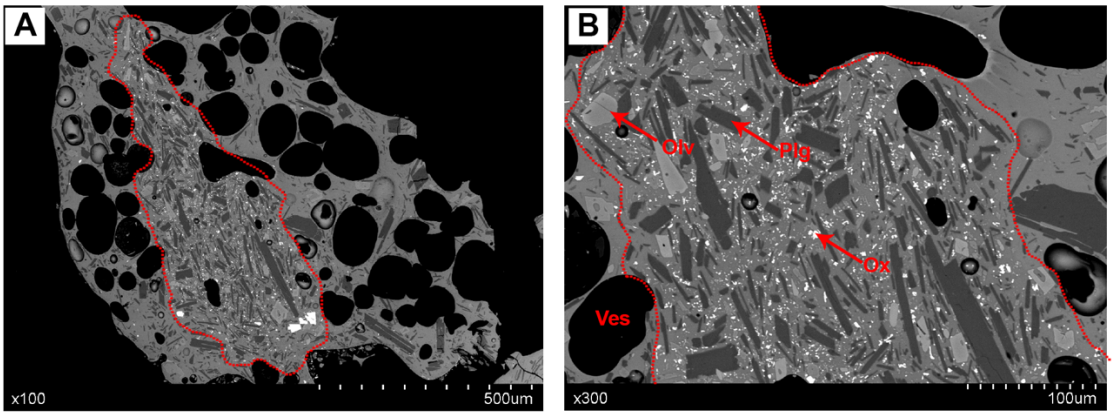

Figure 4.22: *BSE images of the cryptocrystalline and hypocrystalline domains. Red dashed lines outline the boundary between the cryptocrystalline and hypocrystalline domains.*

Pyroclasts - Type 3

The type 3 pyroclasts are found in the basal units where they make up 16-36 wt.% of the beds. The clasts range from prolate to equant with uneven edges and are up to 16

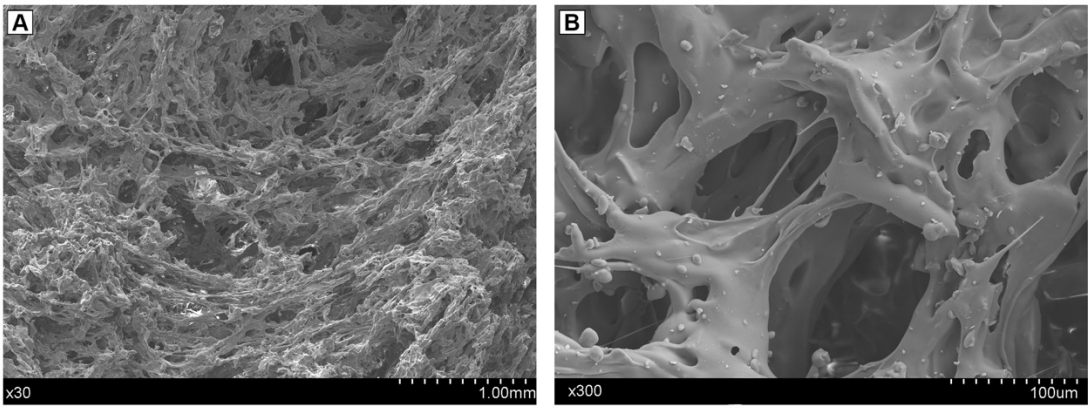

Figure 4.23: *SEM images of the surfaces of the type 3 clasts.* ***A)*** *Complex interior vesicle network.* ***B)*** *Broken vesicle filaments.*

mm long. Their surfaces are characterised by a smooth and fluidal exterior, made up of a complex network of vesicle walls, 5-100 μm thick **(figure 4.23a)**. Surface mounds and elongate ridges form above interior vesicles. Thin glass strands (1-2 μm in diameter) protruding off the surfaces **(figure 4.23b)** are filaments of vesicles that were broken and stretched during fragmentation or transportation.

Type 3 pyroclasts are highly vesicular (~60-80%). Vesicles are mainly rounded to sub-rounded and up to 500 μm in diameter **(figure 4.24a)**. Rare large, irregular shaped vesicles (<3200 μm in diameter) occur towards their centres.

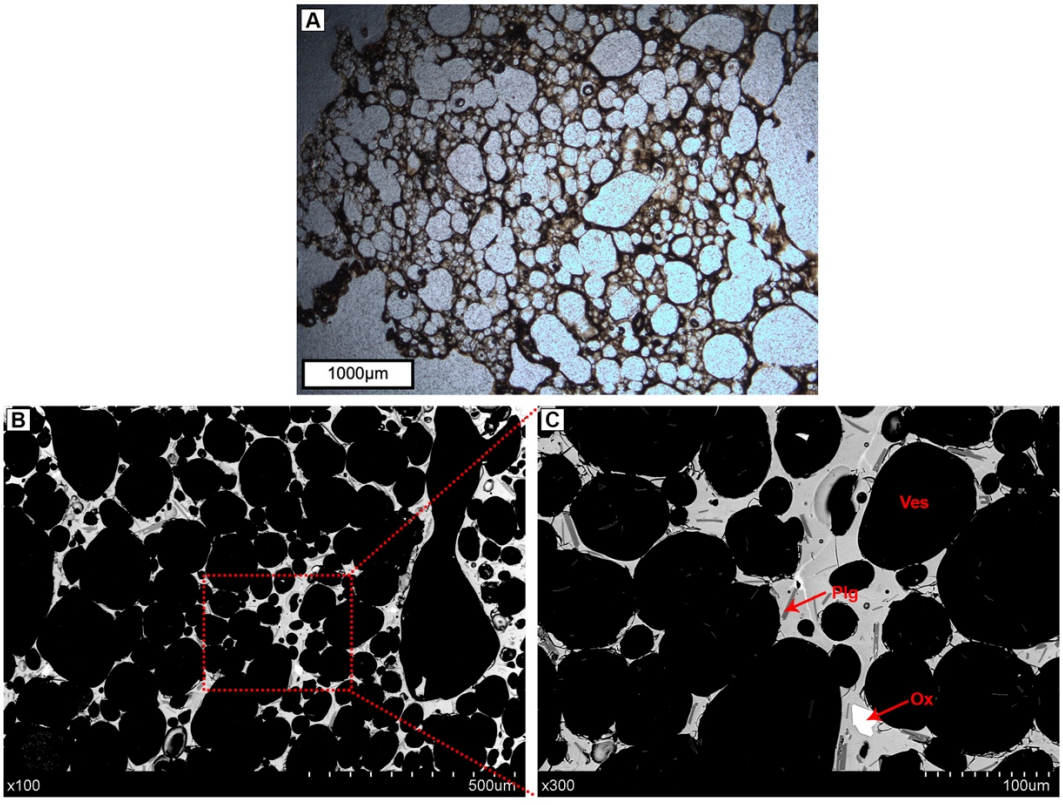

Figure 4.24: *Photomicrographs and BSE images showing vesicularity* ***(A)*** *and crystallinity* ***(B,C)*** *of the type 3 clasts.*

The surface of the clasts are covered by extremely fine (<1 μm in diameter), needle-like precipitates and patches, up to 10 μm in diameter, of sub-spherical and angular precipitates **(figure 4.25a)**. Larger precipitates on the surface (<5 μm in diameter) are blocky, angular or sub-spherical droplets, attached to the surface by fine, needle-like precipitate strands (<1 μm in diameter) **(figure 4.25b)**.

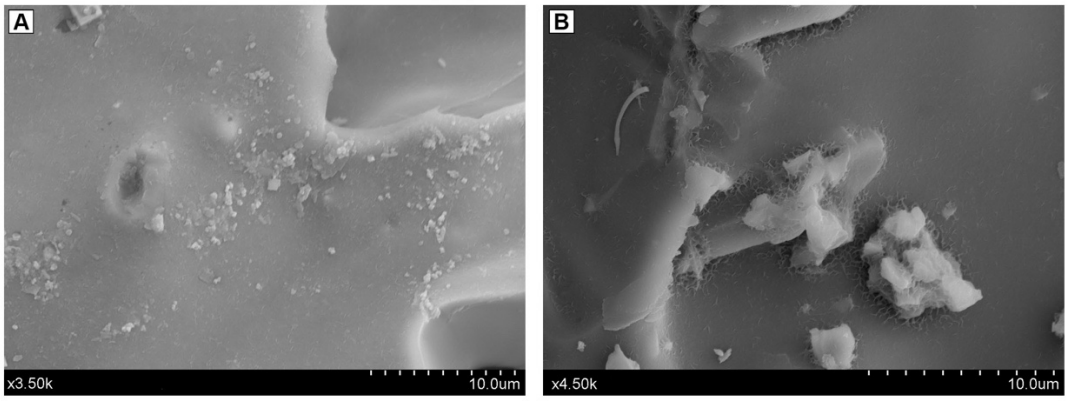

Figure 4.25: *SEM images of the adhered clasts.* ***A)*** *Fine precipitates on the surface of the clasts.* ***B)*** *Larger precipitates attached to the surfaces by needle-like precipitates.*

Particles of glass shards, Pele's hair, and precipitates are accreted to ~10 area% of the surface **(figure 4.26a)**. The glass shards are angular and <50 μm in diameter. Pele's hair are <50 μm long and <2 μm wide. There surfaces are smooth with rare adhering particles. Beads (<4 μm in diameter) form along the Pele's hair **(figure 4.26b)**. <20 area% of the adhered clasts have sub-spherical precipitate droplets on their surface.

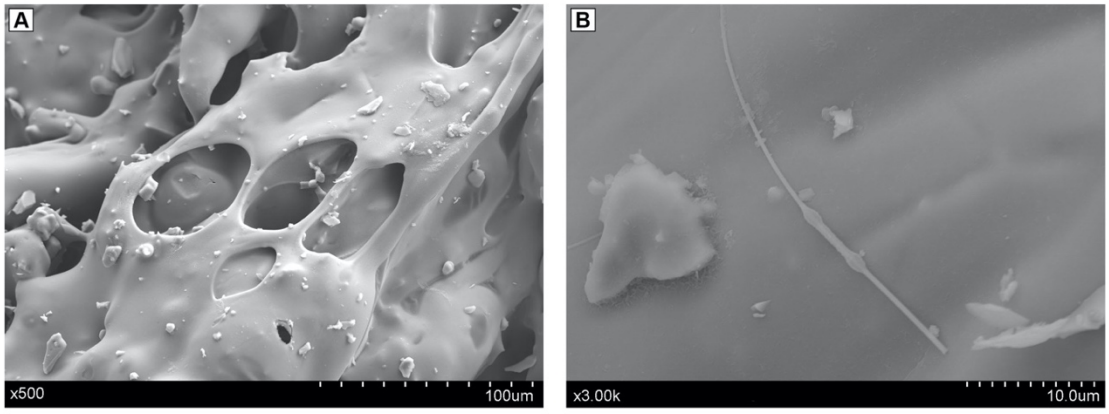

Figure 4.26: *SEM images of the adhered clasts.* ***A)*** *Particles adhered to the surface of the clasts.* ***B)*** *Pele's hair with beads forming.*

Type 3 clasts show two different textural domains **(figure 4.27)**. In the first, the groundmass is hypocrystalline, pale brown, sideromelane glass**.** Microlitic crystals range up to 80 μm in diameter and comprise of, in order of decreasing abundance, plagioclase, olivine and Fe-Ti oxides. The exteriors of the clasts contain dendritic Fe-Ti oxides <1 μm long. The second makes up <5 area% of the clast. The groundmass is hypocrystalline, dark brown-black, tachylite-like glass. Microlitic crystals range up to 100 μm in diameter and

comprise of, in order of decreasing abundance, plagioclase, Fe-Ti oxides and olivine. The contact between the two domains is sharp.

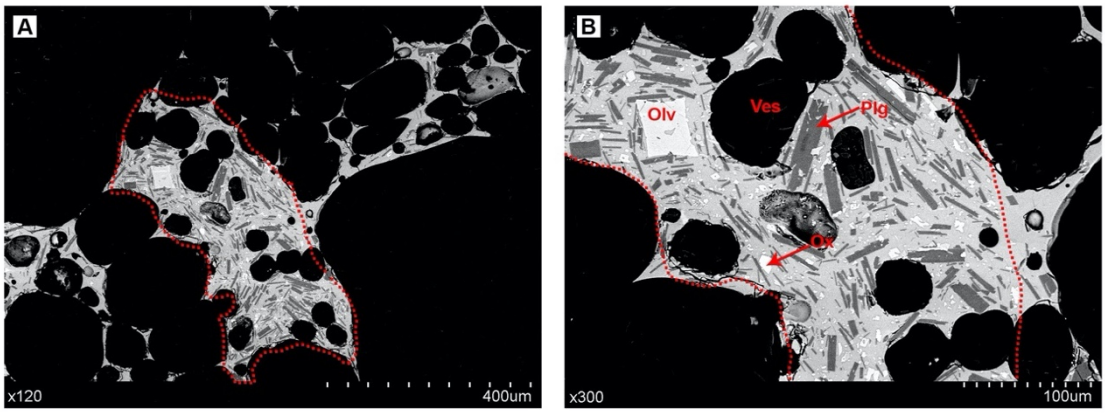

Figure 4.27: *BSE images of the different textural domains. Red dashed lines outline the boundary between the cryptocrystalline and hypocrystalline domains.*

The crystal content is <5 area% **(figure 4.24b,c)**. Individual plagioclase crystals are most common (~2-5 area%), followed by olivine crystals (<2 area%). Both mineral phases contain inclusions of Fe-Ti oxides and/or volcanic glass.

Mineral Phases

Plagioclase

Plagioclase microphenocrysts are most abundant in pyroclast types 1 and 2 and are rare in pyroclast type 3. They are anhedral to subhedral, tabular, acicular, skeletal, and 100-500 μm in diameter **(figure 4.28a)**. ~65 area% exhibit resorbed exteriors **(figure 4.28b)** and ~2 area% exhibit sieve textures **(figure 4.28c)**. Pyroclast types 1 and 2 exhibits ~2 area% reverse and/or normal zoning **(figure 4.28c,d)**. ~55 area% contain elongate, spherical and amoeboid glass and/or Fe-Ti oxide inclusions.

Olivine

Olivine microphenocrysts are largest and most abundant in pyroclasts type 1, followed by type 2, and rare in pyroclasts type 3. They are subhedral to euhedral, equant, tabular and 60-400 μm in diameter **(figure 4.29a)**. ~90 area% have been resorbed **(figure 4.29b)** and ~55 area% are embayed and exhibit hopper forms **(figure 4.29c)**. Crystals have an Mg rich core and contain spherical, elongate and amoeboid glass and/or Fe-Ti oxide inclusions. Glomerocrysts, up to 500 μm in diameter, occur and are composed of tabular, resorbed or acicular plagioclase and Fe-Ti oxides **(figure 4.29d)**. Their structures are open and closed with planar or embedded contacts.

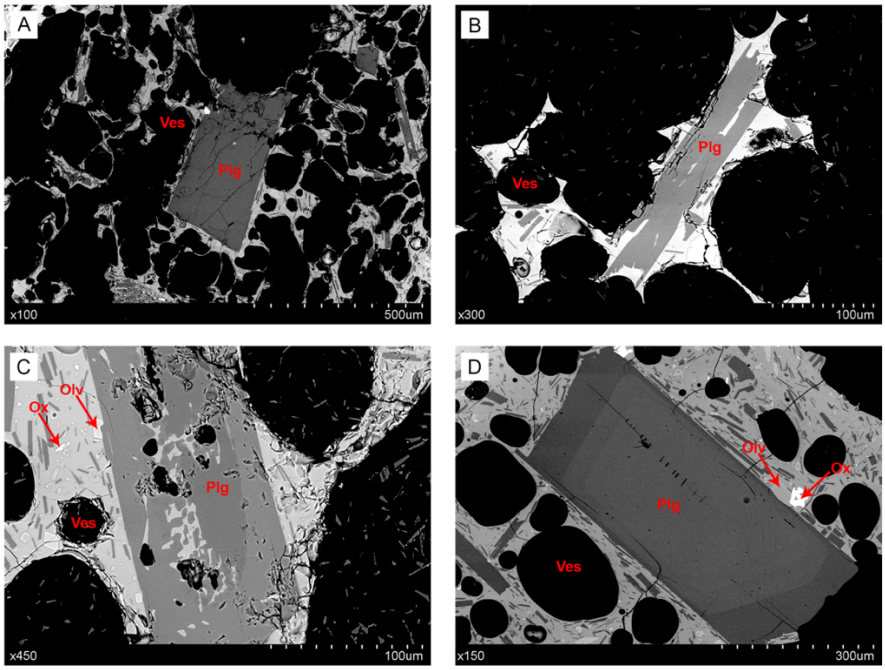

Figure 4.28: *BSE images of plagioclase textures observed in the pyroclasts.* ***A)*** *Subhedral plagioclase crystal in type 1 pyroclasts.* ***B)*** *Plagioclase crystal with resorbed exteriors.* ***C)*** *Plagioclase crystal exhibiting sieve textures and reverse zoning.* ***D)*** *Plagioclase crystal showing normal zoning.*

Fe-Ti oxides

Fe-Ti oxide microphenocrysts occur on pyroclasts type 1 and 2. They are anhedral, blocky, sub-rounded and 50-200 μm in diameter. ~15 area% have been resorbed.

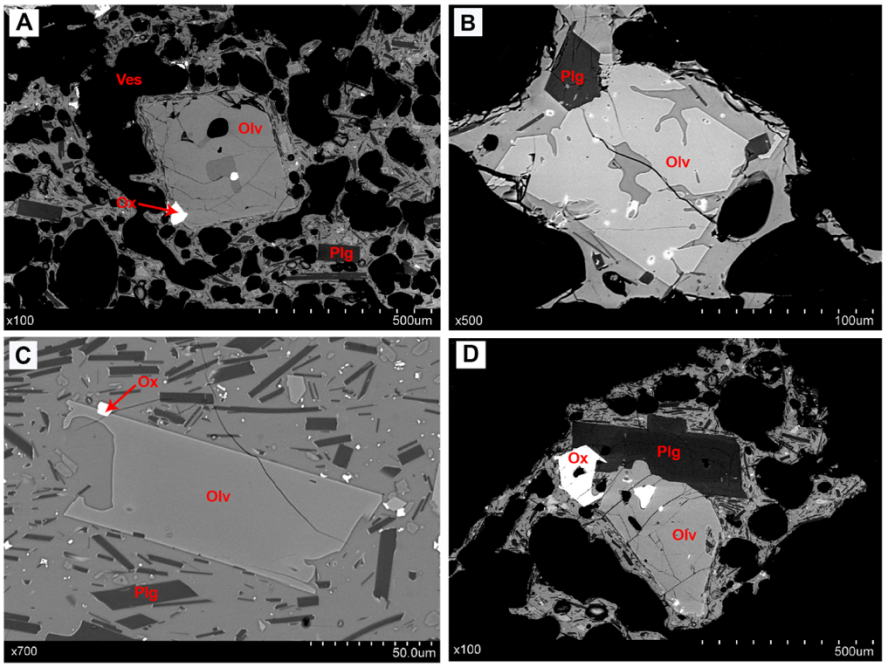

Figure 4.29: *BSE images of olivine textures observed in the pyroclasts.* ***A)*** *Euhedral olivine crystal in type 1 pyroclasts.* ***B)*** *Resorbed olivine crystal.* ***C)*** *Embayed olivine crystal.* ***D)*** *Olivine, plagioclase and Fe-Ti oxide glomerocrysts.*

Groundmass Crystals

The groundmass of the hypocrystalline domains consists of plagioclase (<100 μm in diameter), olivine (<60 μm in diameter) and Fe-Ti oxides (<100 μm in diameter). Plagioclase crystals are subhedral to euhedral, acicular or skeletal. ~15 area% exhibit resorbed exteriors and ~25 area% contain spherical or elongate glass and/or Fe-Ti oxide inclusions. Olivine crystals are solitary, anhedral to euhedral, prismatic and contain single, spherical glass inclusions. Very few exhibit resorbed exteriors. Fe-Ti oxides are sub-rounded and dendritic and form around the rims of ~75 area% of microphenocrysts and vesicles.

The groundmass of the cryptocrystalline domains consists of plagioclase, olivine, clinopyroxene (<10 μm in diameter) and Fe-Ti oxides. Plagioclase crystals are subhedral, acicular or skeletal. ~15 area% exhibit resorbed exteriors and <5 area% contain spherical inclusions of Fe-Ti oxides. Olivine crystals are subhedral, tabular, prismatic and contain spherical inclusions of glass. Clinopyroxene crystals do not occur in all the cryptocrystalline domains. They are anhedral, sub-rounded and do not contain inclusions. Fe-Ti oxide crystals are abundant in the groundmass and are subhedral, sub-rounded and dendritic. They form around the rims of solitary plagioclase and olivine microphenocrysts.

Lithic Clast – Type 1

The first type of lithic clast is dark grey and red, aphanitic and non-vesicular. The groundmass is microcrystalline and consists of plagioclase (<150 μm in diameter), olivine (<90 μm in diameter), clinopyroxene (<50 μm in diameter) and Fe-Ti oxides (<30 μm in diameter) **(figure 4.30a,b)**. Plagioclase crystals are euhedral to subhedral, acicular and not resorbed. <5 area% contain spherical glass and Fe-Ti oxide inclusions. Olivine crystals are subhedral, tabular or needle-like. ~20 area% contain spherical glass inclusions. ~75 area% have been resorbed. Clinopyroxene crystals are subhedral, sub-rounded or tabular. ~25 area% have been resorbed. ~15 area% contain spherical glass inclusions. Fe-Ti oxides are subhedral, blocky, sub-rounded or needle-like. <3 area% contain elongate or amoeboid, volcanic glass inclusions.

The microphenocryst assemblage is dominated by plagioclase (~10 area%), followed by olivine (~3 area%) and Fe-Ti oxides (<2 area%). Clinopyroxene microphenocrysts are not present.

Plagioclase

Plagioclase microphenocrysts are euhedral to subhedral, acicular or tabular and 100-400 μm in diameter. ~55 area% have been resorbed and ~5 area% exhibit sieve textures. ~7 area% exhibit reverse zoning **(figure 4.30c)** and <1area% exhibit normal zoning. <10 area% contain spherical and elongate volcanic glass and Fe-Ti oxide

inclusions. Glomerocrysts, up to 300 µm in diameter, occur and are composed of tabular and acicular plagioclase. Their structures are closed with embedded and planar contacts.

Olivine

Olivine microphenocrysts are anhedral, tabular, prismatic or hopper shaped and 90-500 µm in diameter **(figure 4.30d)**. ~80 area% have been resorbed and ~45 area% embayed. ~85 area% contain spherical and elongate volcanic glass inclusions. Glomerocrysts, up to 300 µm in diameter, occur and are composed of olivine, tabular plagioclase and Fe-Ti oxides. Their structures are closed with planar contacts.

Fe-Ti oxides

Fe-Ti oxide microphenocrysts are subhedral and blocky. ~20 area% contain amoeboid and spherical, volcanic glass inclusions. They are associated with olivine microphenocrysts.

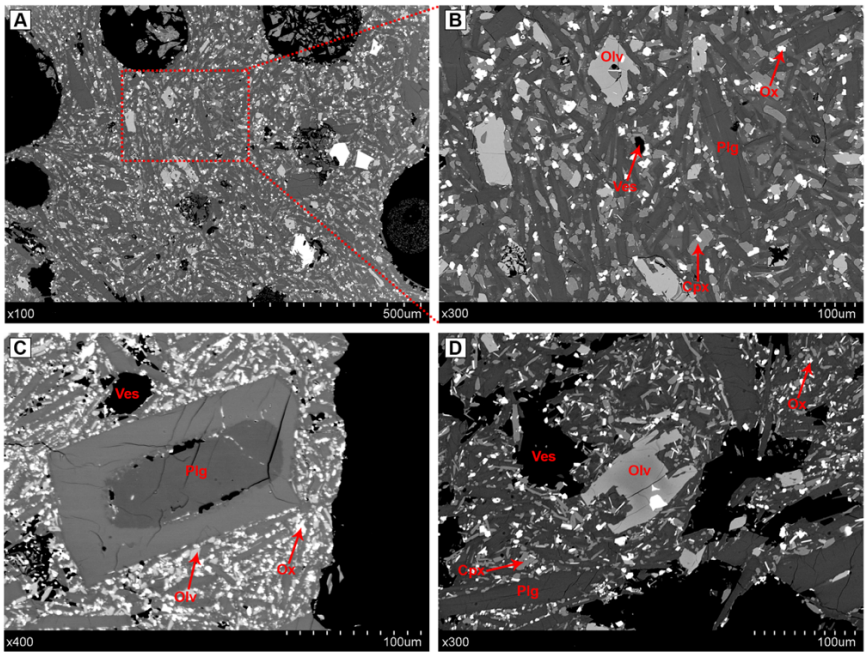

Figure 4.30: *BSE images of **A,B)** Plagioclase, olivine, clinopyroxene and Fe-Ti oxide groundmass in the type 1 lithic clasts. **C)** Reverse zoning in a plagioclase crystal. **D)** Hopper shaped olivine crystal.*

Lithic Clast - Type 2

The second type of lithic clasts are dark grey or red, aphanitic and non-vesicular. The groundmass is microcrystalline and consists of plagioclase (<100 µm in diameter), olivine (<80 µm in diameter), clinopyroxene (<20 µm in diameter) and Fe-Ti oxides (<50 µm in diameter) **(figure 4.31)**. Plagioclase crystals are euhedral to subhedral, tabular, acicular and swallow tailed. <5 area% contain volcanic glass and/or Fe-Ti oxide inclusions and ~15 area% have been resorbed. Olivine crystals are anhedral, tabular and prismatic. ~80 area% have been resorbed and <10 area% contain glass inclusions. Clinopyroxene crystals are anhedral, tabular and needle-like. <3 area% contain glass inclusions and <10 area% have

been resorbed. Fe-Ti oxides are subhedral, blocky, needle-like and dendritic. <5 area% contain spherical glass inclusions.

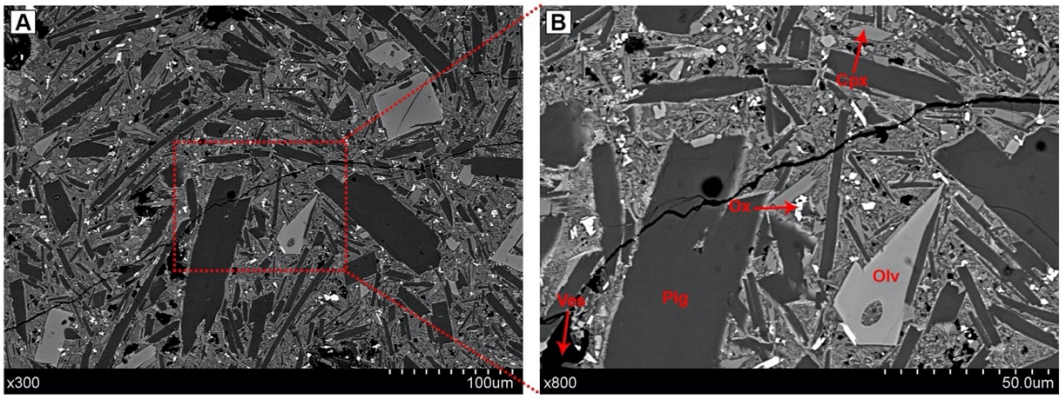

Figure 4.31: *BSE images of the plagioclase, olivine, clinopyroxene and Fe-Ti oxide groundmass in the type 2 lithic clasts.*

The microphenocryst assemblage is dominated by plagioclase (~10 area%), followed by olivine (~5 area%) and Fe-Ti oxides (<3 area%). Clinopyroxene microphenocrysts do not occur.

Plagioclase

Plagioclase microphenocrysts are subhedral, tabular or swallow tailed, and 100-200 µm in diameter. ~20 area% have been resorbed and <1 area% exhibit sieve textures and reverse zoning **(figure 4.32a)**. <5 area% contain spherical or elongate glass and Fe-Ti oxide inclusions.

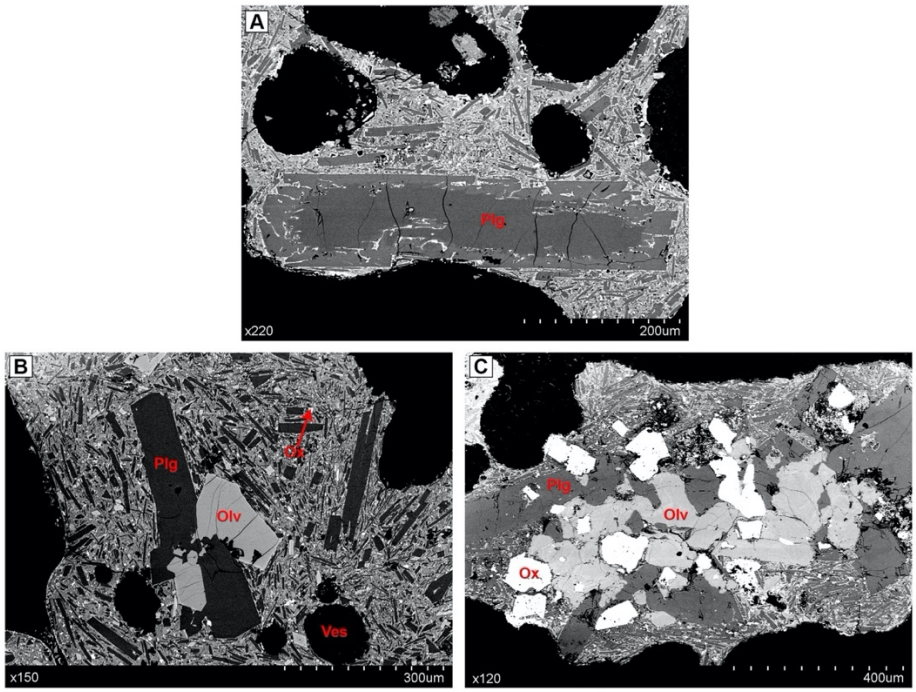

Figure 4.32: *BSE images of **A)** Resorbed plagioclase crystal exhibiting reverse zoning. **B,C)** Olivine, plagioclase and Fe-Ti oxide glomerocrysts.*

Olivine

Olivine microphenocrysts are subhedral to anhedral, tabular or prismatic and 90-200 μm in diameter. ~45 area% have been resorbed and embayed and ~5 area% exhibit normal zoning. ~60 area% contain spherical and elongate glass inclusions. Glomerocrysts, up to 400 μm in diameter, occur and are composed of olivine and tabular plagioclase **(figure 4.32b,c**). Their structures are closed with embedded contacts.

Fe-Ti Oxides

Fe-Ti oxide microphenocrysts are euhedral to subhedral, blocky or tabular and 50-100 μm in diameter. ~20 area% have been resorbed and embayed. ~5 area% contain spherical and elongate glass inclusions.

Lithic Clast - Type 3

The third type of lithic clasts are red/orange, aphanitic and incipiently vesicular. The groundmass is microcrystalline and consists of plagioclase (<100 μm in diameter), olivine (<10 μm in diameter) and Fe-Ti oxides (<10 μm in diameter) **(figure 4.33a,b)**. Plagioclase crystals are euhedral to subhedral, tabular or acicular. <10 area% have been resorbed and ~5 area% contain spherical Fe-Ti oxide inclusions. Olivine crystals are anhedral and tabular. ~10 area% have been resorbed and ~15 area% contain spherical and amoeboid volcanic glass and Fe-Ti oxide inclusions. Fe-Ti oxides are sub-rounded or dendritic and form around the rims of microlites and microphenocrysts.

The microphenocryst assemblage is dominated by plagioclase (~40 area%), followed by olivine (<3 area%) and clinopyroxene (<1 area%).

Plagioclase

Plagioclase microphenocrysts are subhedral, tabular and 100-200 μm in diameter. ~80 area% have been resorbed and ~10 area% exhibit sieve textures. ~5 area% exhibit weak reverse zoning and ~75% contain elongate and spherical, volcanic glass and Fe-Ti oxide inclusions.

Olivine

Olivine microphenocrysts are anhedral, tabular and 30-50 μm in diameter **(figure 4.33c)**. They have been resorbed and embayed and contain elongate and amoeboid, volcanic glass inclusions.

Clinopyroxene

Clinopyroxene microphenocrysts are subhedral to anhedral, equant and 30-50 μm in diameter **(figure 4.33c)**. They have not been resorbed and contain elongate, volcanic glass inclusions.

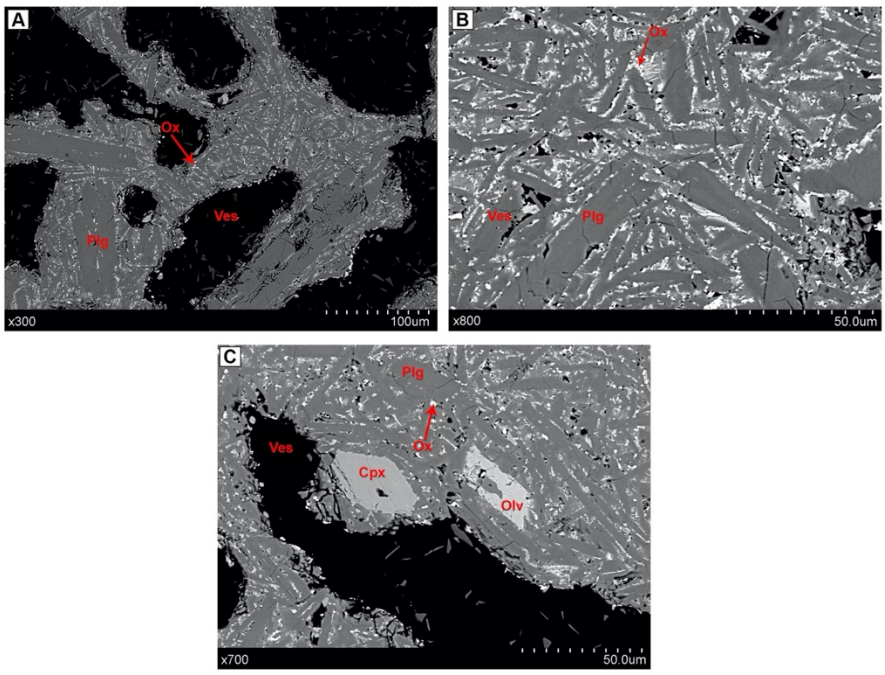

Figure 4.33: *BSE images of **A,B)** plagioclase, olivine, and Fe-Ti oxide groundmass in the type 3 lithic clasts. **C)** Subhedral clinopyroxene and olivine crystal in a plagioclase groundmass.*

Lithic Clast - Type 4:

The fourth type of lithic clasts are orange-red, aphanitic and non-vesicular. The groundmass is hypocrystalline (30 area% crystals: 70 area% glass) and consists of plagioclase (<50 μm in diameter) and Fe-Ti oxides (<10 μm in diameter) **(figure 4.34a, b)**. Plagioclase crystals are subhedral to anhedral, tabular, acicular or skeletal. ~10% exhibit resorbed exteriors and they do not contain inclusions. Fe-Ti oxides are sub-rounded or dendritic and form a coating over the glass.

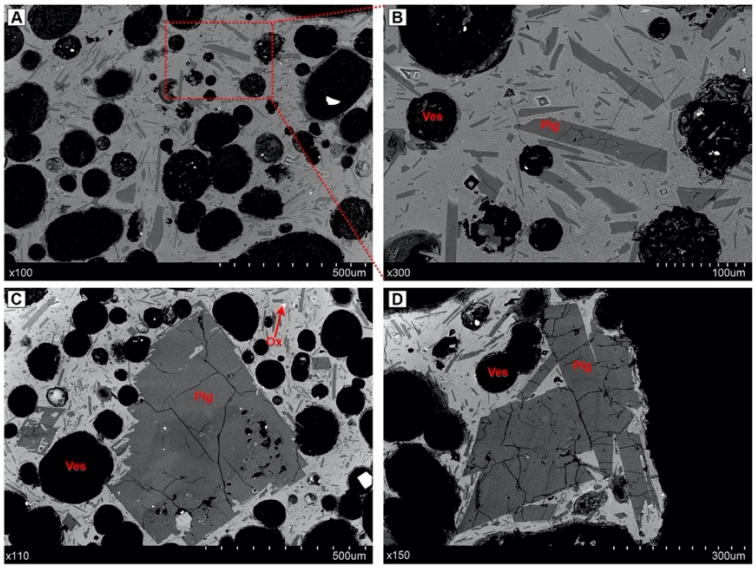

Figure 4.34: *BSE images of **A,B)** Hypocrystalline groundmass. **C)** Partially resorbed plagioclase crystal. **D)** Plagioclase glomerocryst.*

The microphenocryst assemblage is dominated by plagioclase (~6 area%). Phenocrysts of olivine and clinopyroxene are do not occur.

Plagioclase

Plagioclase microphenocrysts are subhedral to anhedral, tabular and 100-500 μm in diameter. ~90 area% have been resorbed and ~5 area% exhibit sieve textures **(figure 4.34c)**. ~10 area% exhibit reverse zoning and 3 area% exhibit normal zoning. ~15 area% contain elongate and amoeboid Fe-Ti oxide inclusions. Glomerocrysts, up to 350 μm in diameter, occur and are composed of tabular, partially resorbed and reverse zoned plagioclase **(figure 4.34d)**. Their structures are open and closed with embedded and point contacts.

Altered Plagioclase Crystals

The defining characteristic between the grey and red lithic clasts is the presence of heavily altered plagioclase microphenocrysts in the red, oxidised lithic clasts. They are dominantly seen in lithic clasts types 2 and 4 but occur in type 1 and are rare in type 3 **(figure 4.35a-c)**. They are anhedral, tabular and up to 200 μm in diameter. They exhibit external resorption and ~10 area% are embayed. Fe-Ti oxides form around the rims, enhancing their shapes, and form at almost 90° across the crystals. ~95 area% of the crystals exhibit pore space behind the Fe-Ti oxide bands and ~5 area% retain the plagioclase crystals **(figure 4.35d)**.

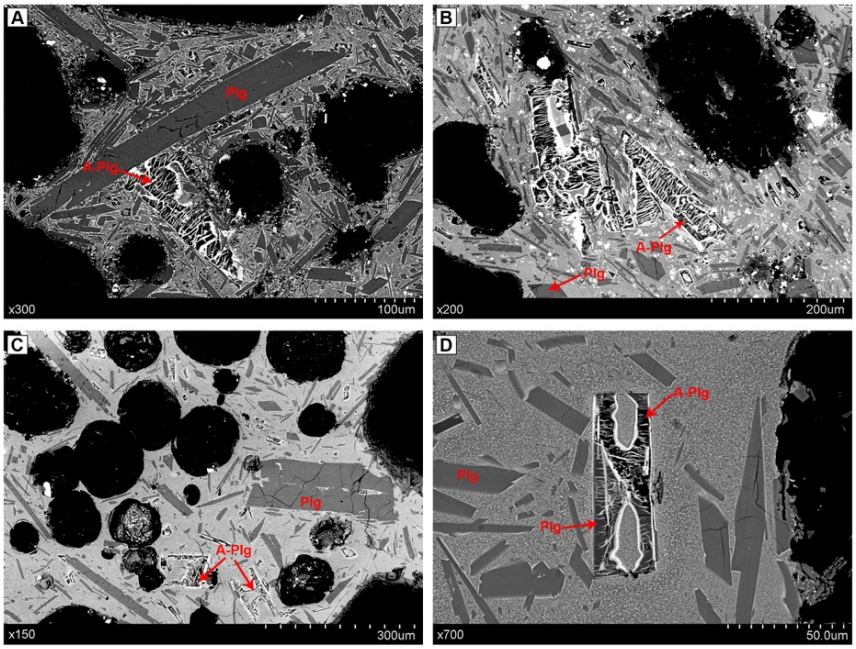

Figure 4.35: *Photomicrographs of the altered plagioclase crystals.* ***A)*** *Altered plagioclase crystals in type 2.* ***B,C)*** *Altered plagioclase crystals in type 4.* ***D)*** *Crystal exhibiting half plagioclase and half pore space.*

Lithic Clast – Type 5

The fifth type of lithic clasts are dark grey, aphanitic and non-vesicular. The groundmass is hypocrystalline (~95 area% crystals: 5 area% glass) and consists of plagioclase (<100 μm in diameter), olivine (<60 μm in diameter), clinopyroxene (<40 μm in diameter) and Fe-Ti oxides (<50 μm in diameter) **(figure 4.36a, b)**. Plagioclase crystals are subhedral, acicular and skeletal. <5 area% contain spherical and elongate glass and Fe-Ti oxide inclusions. ~30 area% exhibit resorbed exteriors. Olivine crystals are anhedral, tabular and ~85 area% contain spherical or elongate volcanic glass inclusions. ~20 area% have been resorbed and <5 area% have been embayed. Clinopyroxene crystals are subhedral, angular, tabular and resorbed. Spherical glass inclusions occur but are very rare. Fe-Ti oxides are subhedral, elongate and sub-rounded. <5 area% contain spherical volcanic glass inclusions.

The microphenocryst assemblage is dominated by plagioclase (~3 area%), followed by olivine (~2 area%). Clinopyroxene and Fe-Ti oxide microphenocrysts are not present.

Plagioclase

Plagioclase microphenocrysts are solitary, subhedral, tabular and 50-100 μm in diameter. ~5 area% have been resorbed and <5 area% contain amoeboid and spherical, glass and Fe-Ti oxide inclusions. No zoning is present.

Olivine

Olivine microphenocrysts are anhedral, tabular and 100-400 μm in diameter **(figure 4.36a)**. ~90% have been resorbed and they contain spherical and elongate volcanic glass and Fe-Ti oxide inclusions. <5 area% exhibit normal zoning with an Mg-rich core and Fe-rich rim.

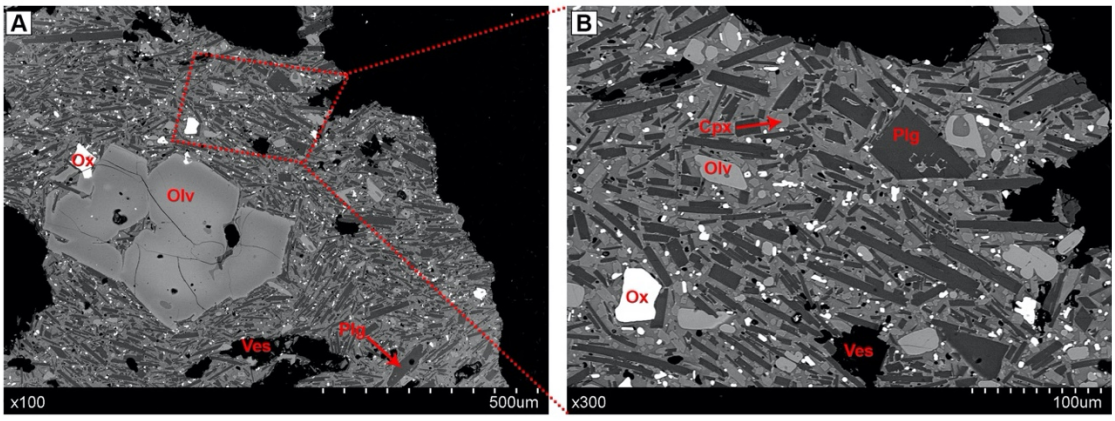

Figure 4.36: *BSE images of **A,B)** hypocrystalline groundmass containing plagioclase, olivine, clinopyroxene and Fe-Ti oxides.*

4.4.4 Grain Size Distribution

The grain size distributions of the proximal and medial sequences are unimodal, with the coarsest layers found in the lower subunit **of the sequence**.

In the proximal deposit P1a is the coarsest bed with a median grain size (Md_ϕ) of -3.2ϕ, whilst P9 is the finest bed with an Md_ϕ of -0.45ϕ **(figure 4.10c,d)**. The beds of ragged scoria (P1a, P1b, P2, P3, P12) have an Md_ϕ range of -3.2ϕ to -1ϕ. The bed of equant, 'ash-coated' scoria (P13) has an Md_ϕ of -0.5ϕ. The beds of ash (P4, P9) have an Md_ϕ range of -1.4ϕ to -0.45ϕ. The sequence begins moderately sorted and gradually becomes poorly sorted with the sorting coefficient (σ_ϕ) ranging from 0.85σ to 1.4σ **(figure 4.10e)**. The massive beds (P1, P2, P3, P12) are moderate to poorly sorted with a σ_ϕ range of 0.85σ to 1.33σ. The stratified bed (P13) is poorly sorted with σ_ϕ of 1.15σ. The beds of ash (P4, P9) are poorly sorted with a σ_ϕ range of 1.1σ to 1.4σ.

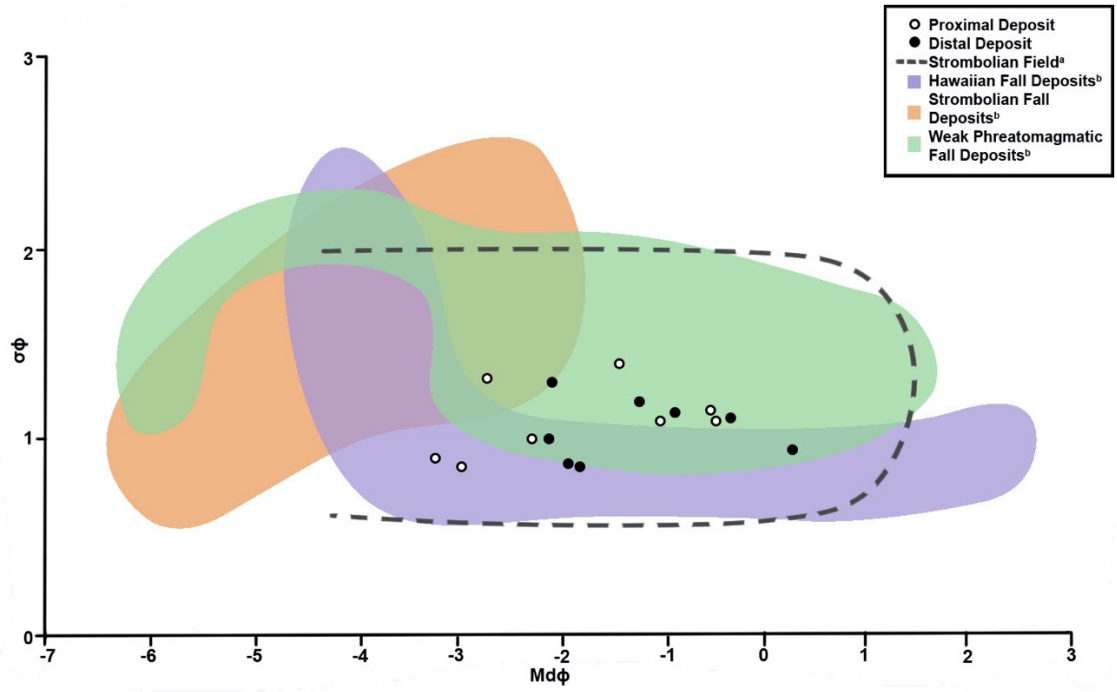

Figure 4.37*: Md_ϕ vs σ_ϕ graph. Hollow circles represent the proximal deposit and filled circles the distal deposit. The dashed line represents the Strombolian field defined by Walker and Croasdale (1972) and the orange, green and purple fields define the Strombolian fall, weakly Phreatomagmatic and Hawaiian fall deposits field, respectively from Houghton and Carey (2015).*

In the medial deposit M2 is the coarsest bed with an Md_ϕ of -2.1ϕ, whilst M7 is the finest bed with an Md_ϕ of 0.3ϕ **(figure 4.11c,d)**. The beds of ragged scoria (M1, M2, M4, M6) have an Md_ϕ range of -2.1ϕ to -0.85ϕ. The beds of equant, 'ash-coated' scoria (M3, M8) have an Md_ϕ range of -1.9ϕ to -1.2ϕ. The beds of ash (M5, M7) have an Md_ϕ range of -0.3ϕ to 0.3ϕ. The sequence starts off moderately sorted and progressively becomes poorly

sorted **(figure 4.11e)**, with σ_ϕ ranging from 0.85σ to 1.3σ. The massive beds (M2, M3, M4) are moderately sorted with a σ_ϕ ranging from 0.85σ to 1σ. The stratified bed is poorly sorted and has σ_ϕ of 1.2σ. The ash layers are moderately/poorly sorted with σ_ϕ ranging from 0.95σ to 1.13σ.

When Md_ϕ is plotted against σ_ϕ (Inman, 1952), the samples all plot within the Strombolian field defined by Walker and Croasdale (1972). The lower units also sit within the Hawaiian/weakly Phreatomagmatic fields, whilst the upper units sit within the weakly phreatomagmatic field (Houghton and Carey, 2015) **(figure 4.37)**. There is a minor trend, showing that as Md_ϕ decreases up section, the degree of sorting decreases. The trend is obvious within the proximal section, but fluctuates within the medial section, as D7 is moderately sorted and D2 is moderate-poorly sorted.

4.4.5 Vesicularity

Vesicularity measurements were taken from the type 2 pyroclasts in the lower subunit. The distribution of data is unimodal and narrow, with a mean density of 0.46 g/cm^3, corresponding to a vesicularity index of 82%. The main peak is at 0.4-0.5 g/cm^3 with few clasts in the 0.7-0.8 g/cm^3 and 0.8-0.9 g/cm^3 ranges **(Figure 4.38)**. The density range is 0.28-0.9 g/cm^3, corresponding to a vesicularity range of 65-89%.

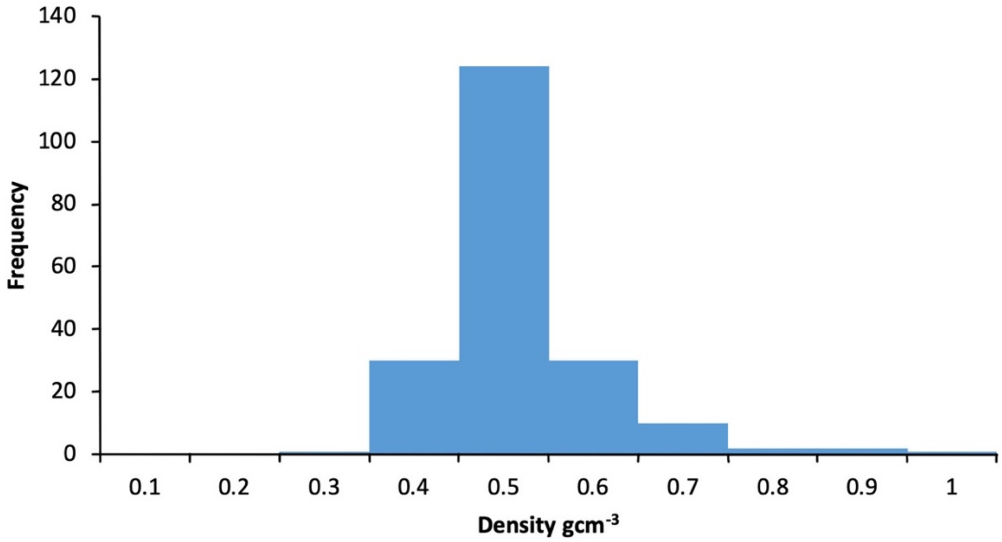

Figure 4.38: *Histogram showing the clast density distribution from the lower subunit*. n = 100.

4.5 Tephra Volume and Distribution

4.5.1 Unit 3 Tephra Volume and Distribution

The Unit 3 scoria was generally dispersed west/north-west of the vent. There is a slight variation in the dispersal axis over the course of the eruptions, with few thicker deposits distributed south of the vent and fewer thin deposits distributed to the south-west.

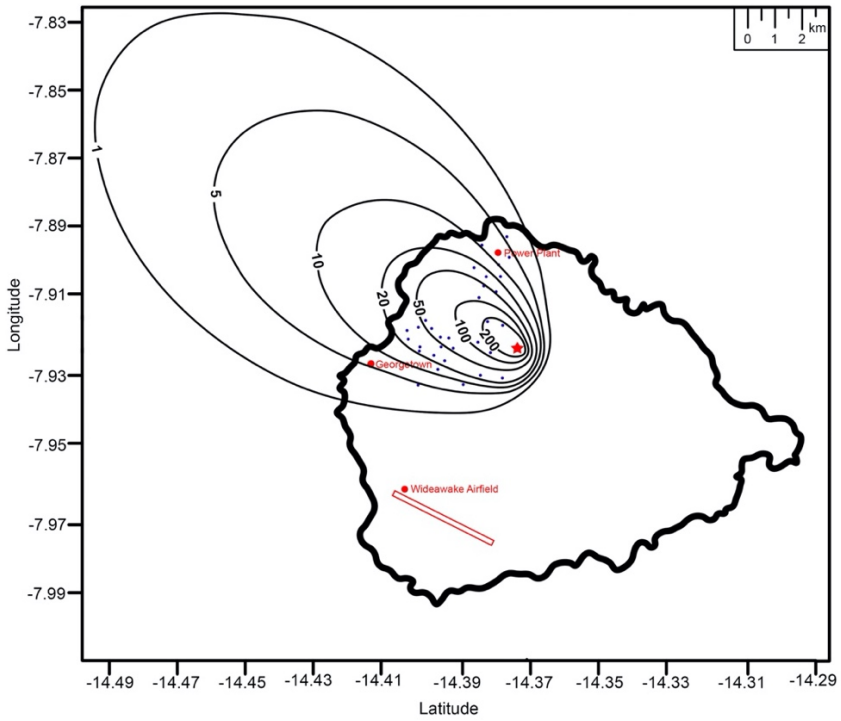

Figure 4.39: *Isopach map of the Unit 3 scoria. Blue dots represent sample sites and red star is vent location. Isopachs are in cm.*

The eruptions covered a minimum of 24 km^2 on land and extended further into the sea. The deposit is 354 cm thick, 1.24 km from the vent: the thinnest preserved deposit is 4.5 cm, to the left of the dispersal axis, 3.25 km from the vent. The 5 cm isopach encloses an area of 32.9 km^2 on land and in the sea **(figure 4.39)**. The volume of the Unit 3 scoria was estimated from the plot of ln(thickness) vs (isopach area)$^{1/2}$ using the exponential method from Pyle (1989). The field data fits well with the exponential thinning relationship (Pyle, 1989) **(figure 4.40)** and the resulting volume of the deposit is 4.9 x 10^5 m^3. The volume was converted to

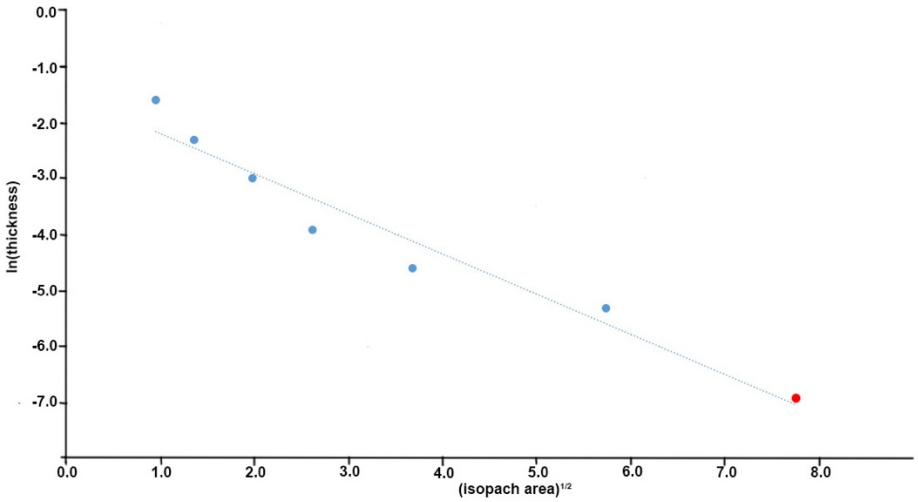

Figure 4.40: *ln(thickness) vs (isopach area)$^{1/2}$ for the Unit 2 eruption. The data shows a weak exponential thinning away from the vent. This could be due to lack of data in the frontal section of the cone and the associated uncertainties connecting isopachs. The red dot represents the 1cm isopach, defined from extending the trend line.*

a DRE of 7.6 x 10^4 m^3 with an erupted mass of 2.03 x 10^8 kg (assuming a deposit density of 400 kg/m^3). This represents a VEI 1 eruption and is consistent with a small Hawaiian/Strombolian eruption.

4.5.2 Maximum Clast Size

Isopleth maps can be a more reliable indicator of vent location, as it is expected that one would find the coarsest clasts within close proximity to the vent. However, isopleths from scoria clasts are less reliable than isopleths of pumice clasts and lithic clasts because scoria is fragile and breaks up easily (Bonadonna et al, 2013).

Scoria clasts of up to 26.5 mm were found in the most proximal deposit and up to 9 mm in the most distal, on land deposit. The 25 mm isopleths disperse to the south-west of the vent before elongating north-west towards the coast, whilst the 10-, 15-, 20- and 30 mm isopleths only elongate north-west towards the coast **(Figure 4.41a-e)**.

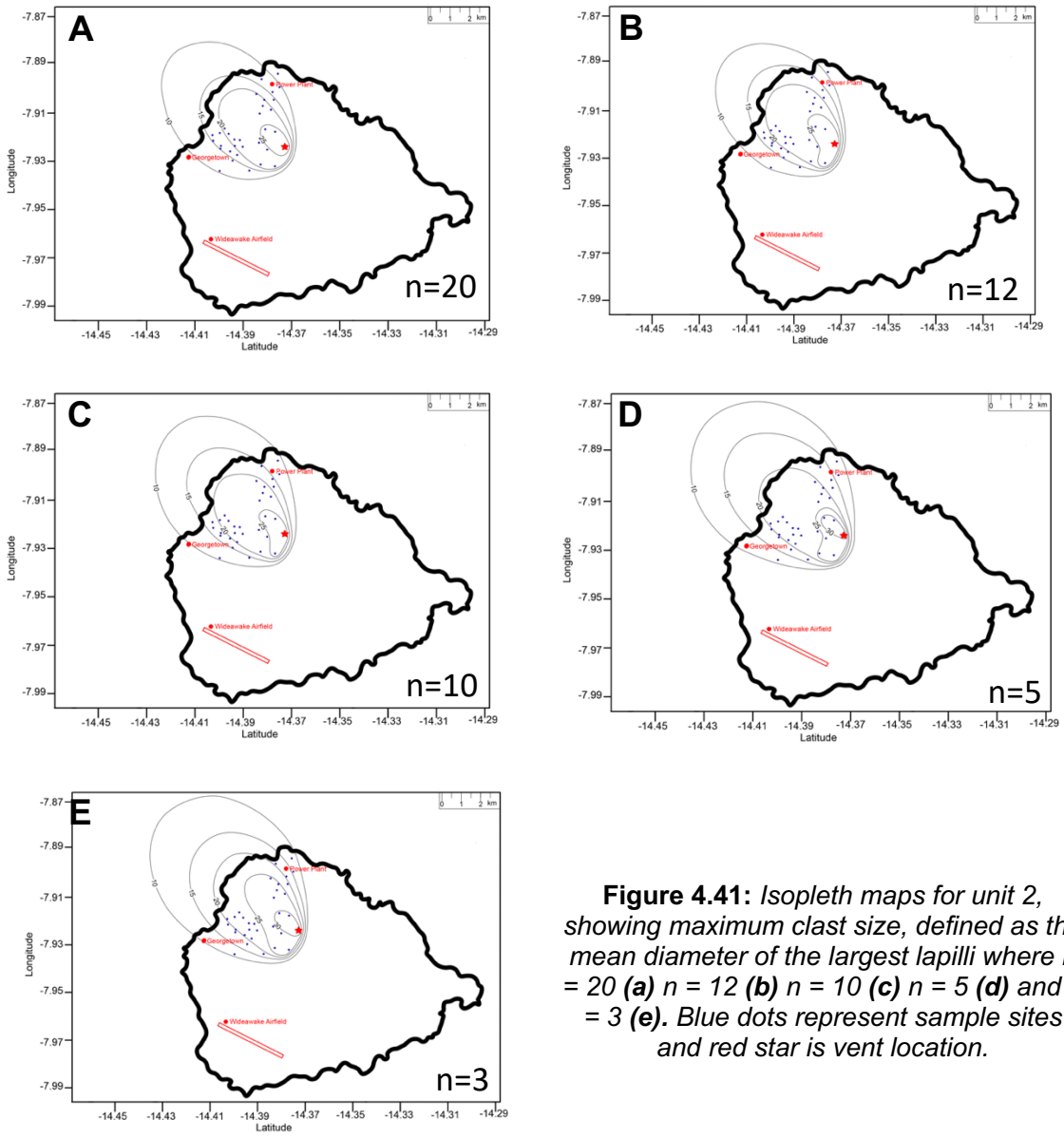

Figure 4.41: *Isopleth maps for unit 2, showing maximum clast size, defined as the mean diameter of the largest lapilli where n = 20* ***(a)*** *n = 12* ***(b)*** *n = 10* ***(c)*** *n = 5* ***(d)*** *and n = 3* ***(e).*** *Blue dots represent sample sites and red star is vent location.*

4.5.3 Modelled Tephra Distribution

The original erupted mass calculated from the isopach data **(table 4.2)** was used as an input parameter for the TephraProb model (Biass et al, 2016) but failed to produce dispersal maps that displayed thicknesses within a suitable range of the measured field data. This could be caused by an inaccurate total thickness and tephra volume inferred from the drawn isopachs or a deposit density that was too low. However, the shape of the isopachs fit with the modelled outputs. In order to overcome this, the erupted mass was increased to model a VEI 2 event **(table 4.2)**. This was done because it was assumed the original volume, calculated to have a mass equivalent to a VEI 1 eruption **(table 4.2)**, was too small to represent the eruption. The resulting maps from these inputs correlated more accurately with the field data but still showed a slight variation. The maps also show the deposit is dispersed to the north west/west.

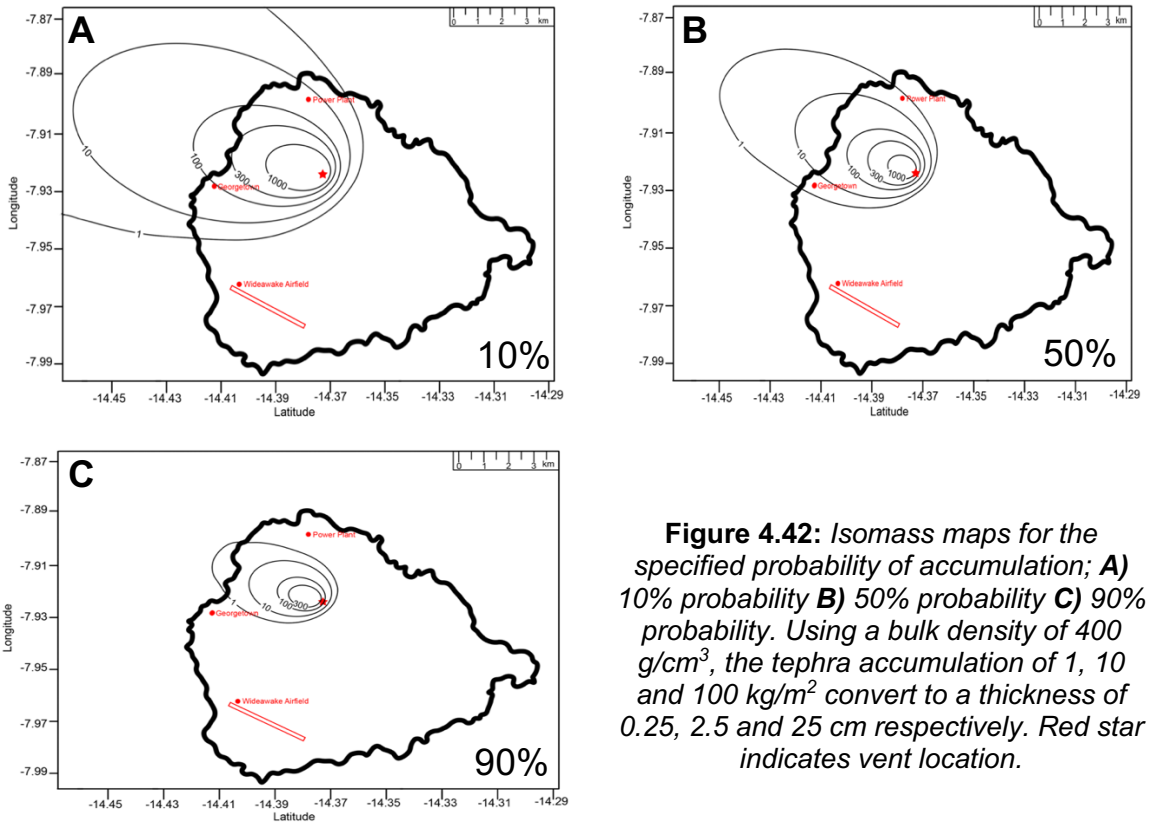

Figure 4.42: *Isomass maps for the specified probability of accumulation;* ***A)*** *10% probability* ***B)*** *50% probability* ***C)*** *90% probability. Using a bulk density of 400 g/cm^3, the tephra accumulation of 1, 10 and 100 kg/m^2 convert to a thickness of 0.25, 2.5 and 25 cm respectively. Red star indicates vent location.*

TephraProb maps display the dispersal data in two ways. The first is an isomass map for a specified probability of accumulation (**figure 4.42a-c)**, and the second is a probability map that shows the probability (0 to 1) for a specified threshold of tephra accumulation (**figure 4.43a, b)**. The accumulations on the maps are conditional on the occurrence of the modelled scenario (Biass et al, 2017).

In an attempt to increase the accuracy of the modelled maps, the field data was run through the Tephra2 Inversion code (Connor and Connor, 2006), and the results were used for TephraProb. This is more accurate as it takes the measured thickness points and

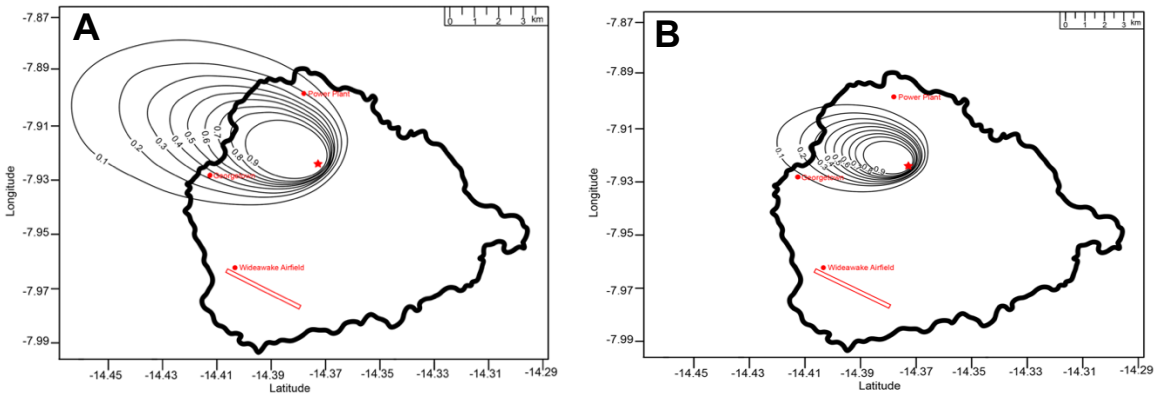

Figure 4.43: *Probability maps or the specified threshold of tephra accumulation at 50% probability;* ***A)*** *10 kg/m^2* ***B)*** *100 kg/m^2. Using a bulk density of 400 g/cm^3, the tephra accumulation of 10 and 100 kg/m^2 convert to a thickness of 2.5 and 25 cm respectively. Red star indicates vent location.*

calculates the eruption parameters required to deposit the specific thickness at each point, rather than using eruption parameters calculated by an individual. From the 16068 runs by the inversion model, the following data was acquired: (1) column height of 1377 m asl; (2) total erupted mass of 5.5 x 10^9 kg; (3) DRE volume of 1.4 x 10^7 m^3 (assuming a deposit density of 400 kg/m^3). However, the TephraProb maps produced were still not fully representative of the measured values.

	Volume (m^3)	Erupted Mass (kg)	DRE (m^3)	Column Height (m)	VEI
Isopachs	4.9 x 10^5	2.03 x 10^8	7.6 x 10^4	-	1
TephraProb	5 x 10^6 – 5 x 10^7	2 x 10^9 – 2 x 10^{10}	7.7 x 10^5 – 7.7 x 10^6	1000-5000	2
Tephra2 Inversion	8.9 x 10^7	5.5 x 10^9	1.4 x 10^7	1377	3

Table 4.2: *Table comparing the volume, erupted mass and DRE from the measured isopachs and modelled dispersal maps.*

4.6 Petrography of other Sisters Scoria cone complex products

The petrography of tephra from different eruptions at the SSCC were studied and compared with lava samples, also sourced from the SSCC, in an attempt to correlate individual fall deposits and lava flows. The tephra samples described below were sourced from Unit 1, Unit 2 **(figure 4.4)** and Unit 4 **(figure 4.5).**

4.6.1 Sisters Tephra

Unit 1 Scoria

Unit 1 clasts are medium brown sideromelane glass with areas of dark brown, devitrified glass around the rim and within the clast **(figure 4.44a)**. Clasts are highly vesicular with a heterogeneous vesicle distribution of small, ovoid vesicles (<150 μm in diameter) and large, irregular vesicles (<1500 μm in diameter). Plagioclase microphenocrysts are subhedral, tabular and <1000 μm in diameter. They exhibit resorbed exteriors and sieve textures **(figure 4.44b)**. Olivine microphenocrysts are rare and anhedral. The hypocrystalline groundmass has microlitic crystals of acicular plagioclase and rare olivine. Opaque minerals are small (<200 μm in diameter). Hypocrystalline clasts containing microlitic crystals of plagioclase are attached to the exterior of the clasts **(figure 4.44c)**. Aphanitic clasts containing microlitic crystals of plagioclase and olivine form bands or patches, with trachytic textures, are attached to the interior of the clasts **(figure 4.44d)**.

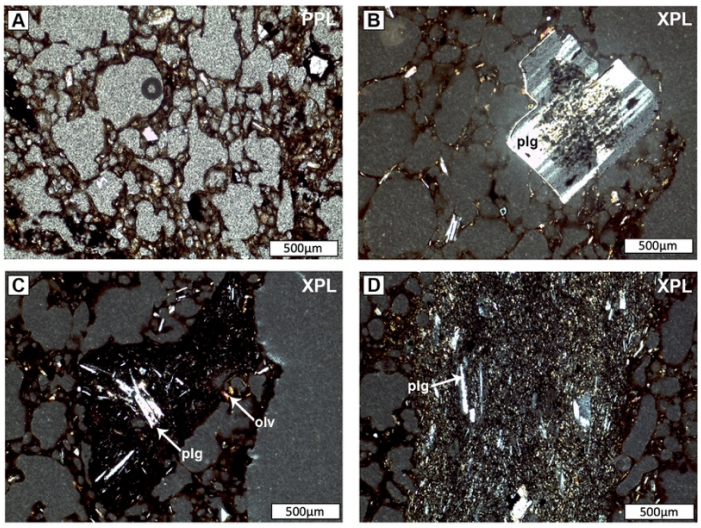

Figure 4.44: *Photomicrographs of the Unit 1 scoria.* ***A)*** *Medium brown sideromelane glass with ovoid vesicles.* ***B)*** *Plagioclase exhibiting sieve textures.* ***C)*** *Hypocrystalline clast with plagioclase microlites.* ***D)*** *Aphanitic band of plagioclase and olivine microlites.*

Unit 2 Scoria

Unit 2 clasts are light brown sideromelane glass with areas of dark brown, devitrified glass. Clasts are highly vesicular and exhibit small, ovoid vesicles (<450 μm in diameter) in their rims and large, irregular vesicles (<2000 μm in diameter) in their centres **(figure 4.45a)**. Plagioclase microphenocrysts are euhedral, tabular and <1500 μm in diameter. A few exhibit sieve textures **(figure 4.45b)**. Olivine microphenocrysts are rare. They are euhedral with small (<50 μm in diameter) opaque mineral inclusions. The hypocrystalline groundmass has microlitic crystals of acicular plagioclase and rare olivine **(figure 4.45c)**. Opaque minerals are rare and <100 μm in diameter.

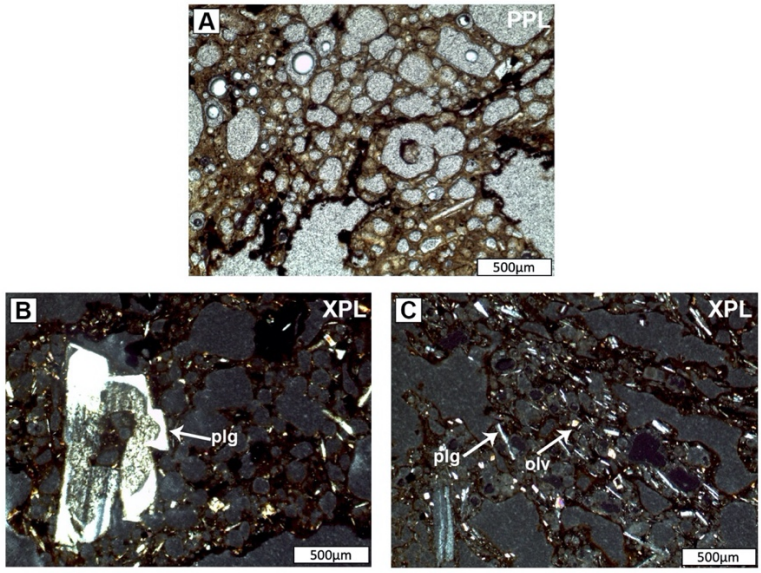

Figure 4.45: *Photomicrographs of the Unit 2 scoria.* ***A)*** *Medium brown sideromelane glass exhibiting heterogeneous vesicle shapes.* ***B)*** *Plagioclase exhibiting sieve textures.* ***C)*** *Groundmass of acicular plagioclase and olivine.*

Unit 4 Scoria

Unit 4 clasts are light brown sideromelane glass with areas of dark brown, devitrified glass around their rims **(figure 4.46a)**. Clasts are highly vesicular and exhibit small, sub-rounded vesicles (<300 µm in diameter) in their rims and larger, irregular vesicles (<1000 µm in diameter) in their centres. Plagioclase microphenocrysts are euhedral, acicular and <500 µm in diameter. Olivine microphenocrysts are euhedral and <1000 µm with small (<100 µm in diameter) opaque mineral inclusions **(figure 4.46b)**. Glomerocrysts, 600 µm in diameter, occur and are comprised of olivine, plagioclase and Fe-Ti oxides with closed structures **(figure 4.46c)**. The hypocrystalline groundmass has microlitic crystals of acicular plagioclase and olivine. Opaque minerals are small (<100 µm in diameter).

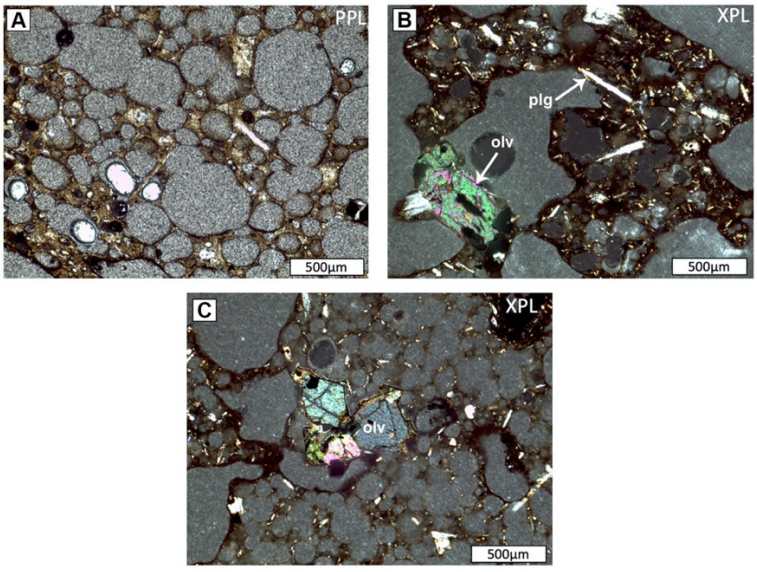

Figure 4.46: *Photomicrographs of the Unit 4 scoria.* ***A)*** *Medium brown sideromelane glass with sub-rounded vesicles.* ***B)*** *Acicular plagioclase in a glassy groundmass and a subhedral olivine with an elongate, opaque inclusion.* ***C)*** *Olivine glomerocryst.*

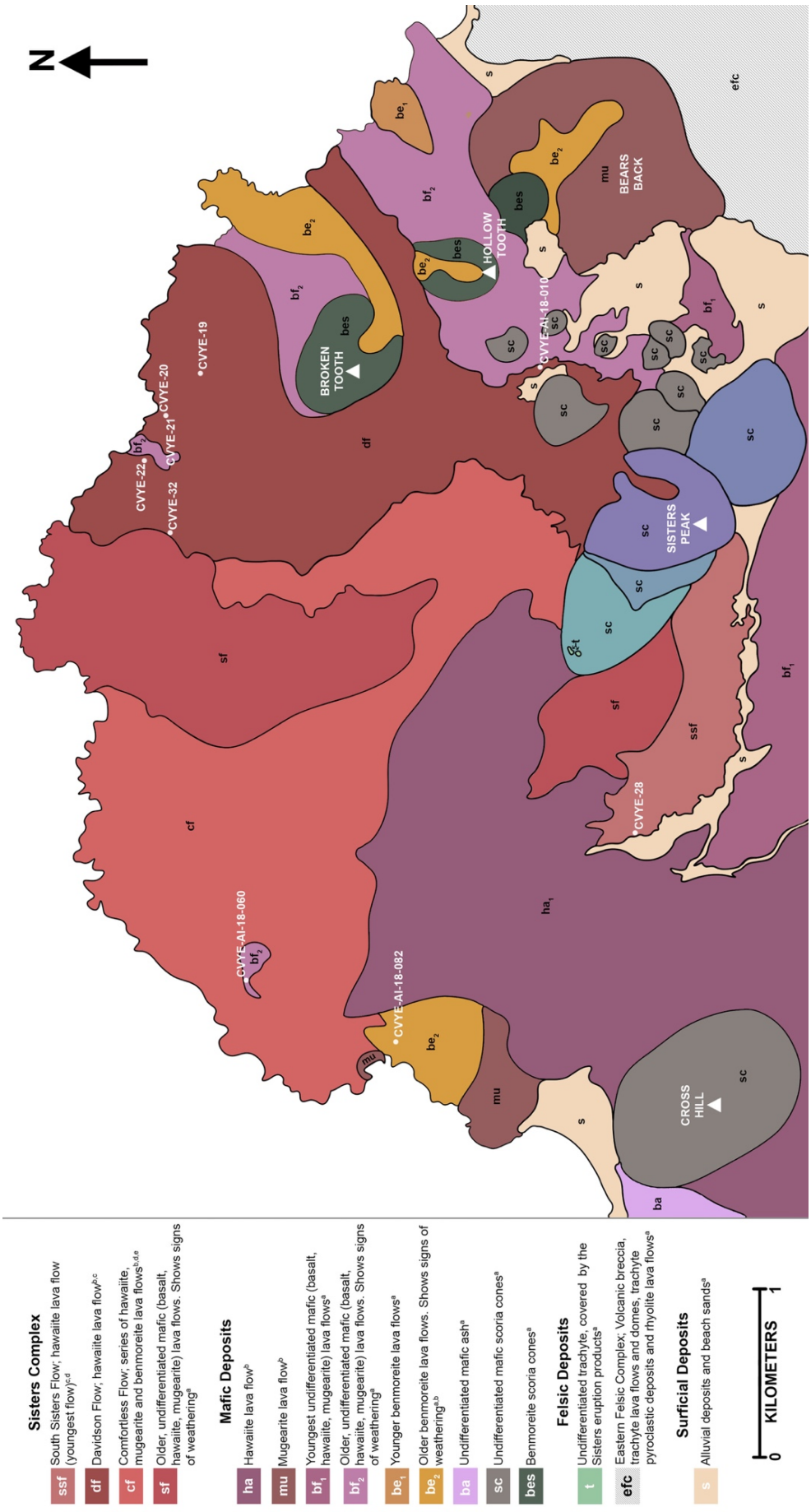

Figure 4.47: *Geological map of the Sisters scoria cone complex. [a]Nielson and Sibbett, 1996, [b]Jicha et al, 2013, [c]Preece et al, 2018, [d]Chamberlain et al, 2016, [e]Weaver et al, 1996.*

4.6.2 Sisters Lava

Nine lava samples were analysed in an attempt to use petrography to link the different lava flows around Sisters to the scoria deposits and to catalogue the petrographic variation in the lavas around Sisters. The different flows and sample locations can be seen in **figure 4.47.**

The Davidson Flow

The Davidson Flow (named in Preece et al (2018)) has been split into proximal and distal sections. The flow is a hawaiite a'a flow, emplaced north-east of Sisters. It was derived from a vent in the crater of Sisters Peak, has a DRE volume of ~6.8 x 10^7 m^3 and extends 3 km towards the coast. It has been dated at 1.64 ± 0.37 ka (Preece et al, 2018).

Distal Samples

Samples CVYE-21, CVYE-22 and CVYE-32 were collected ~2.5 km from the vent and within 0.7 km of each other. The lavas are medium-dark grey, aphanitic to fine-grained phaneritic and exhibit a range of vesicularity values: CVYE-21 and CVYE-32 are incipiently vesicular and CVYE-22 is poorly vesicular. The samples contain <2 area% plagioclase phenocrysts, up to 4 mm in diameter.

The groundmass of CVYE-21 is hypocrystalline and CVYE-22 and CVYE-32 is microcrystalline. It consists of plagioclase (<500 μm in diameter), olivine (<350 μm in diameter), clinopyroxene (<200 μm in diameter) and Fe-Ti oxides (<400 μm in diameter). Plagioclase crystals are euhedral to subhedral, acicular and ~45 area% have spherical or elongate, opaque inclusions. In CVYE-22 only, ~10 area% exhibit resorbed exteriors and ~40 area% exhibit sieve textures. CVYE-21 and CVYE-22, exhibit a trachytic texture. Olivine crystals are euhedral to subhedral, prismatic or tabular and contain spherical opaque inclusions. Clinopyroxene crystals are euhedral to subhedral, rounded, rarely seen under the petrological microscope and do not contain inclusions. Fe-Ti oxides are sub-rounded or dendritic and form around the rims of phenocrysts.

The phenocryst and microphenocryst assemblage are dominated by plagioclase (~7 area%), followed by olivine (~4 area%). Clinopyroxene microphenocrysts do not occur.

Plagioclase

Plagioclase phenocrysts are subhedral, tabular and 2000-3900 μm in diameter. They exhibit resorbed exteriors and contain elongate and amoeboid opaque inclusions. Plagioclase microphenocrysts are euhedral to subhedral, tabular, acicular or stumpy **(figure 4.48a)** and 500-2000 μm in diameter. ~60 area% have been resorbed and <40 area% exhibit sieve textures **(figure 4.48b,c)**. ~25 area% contain elongate, opaque inclusions. Plagioclase glomerocrysts, up to 300 μm in diameter occur in CVYE-32. Their crystals are

subhedral and acicular with no resorption and their structures are mainly closed with planar contacts.

Olivine

Olivine microphenocrysts are subhedral to anhedral, tabular and 400-1200 μm in diameter. ~60 area% have been resorbed and ~45 area% contain spherical, opaque inclusions **(figure 4.48d)**. Glomerocrysts, up to 1700 μm in diameter, occur and are composed of olivine and tabular plagioclase **(figure 4.48e, f)**. Their structures are open with embedded and planar contacts.

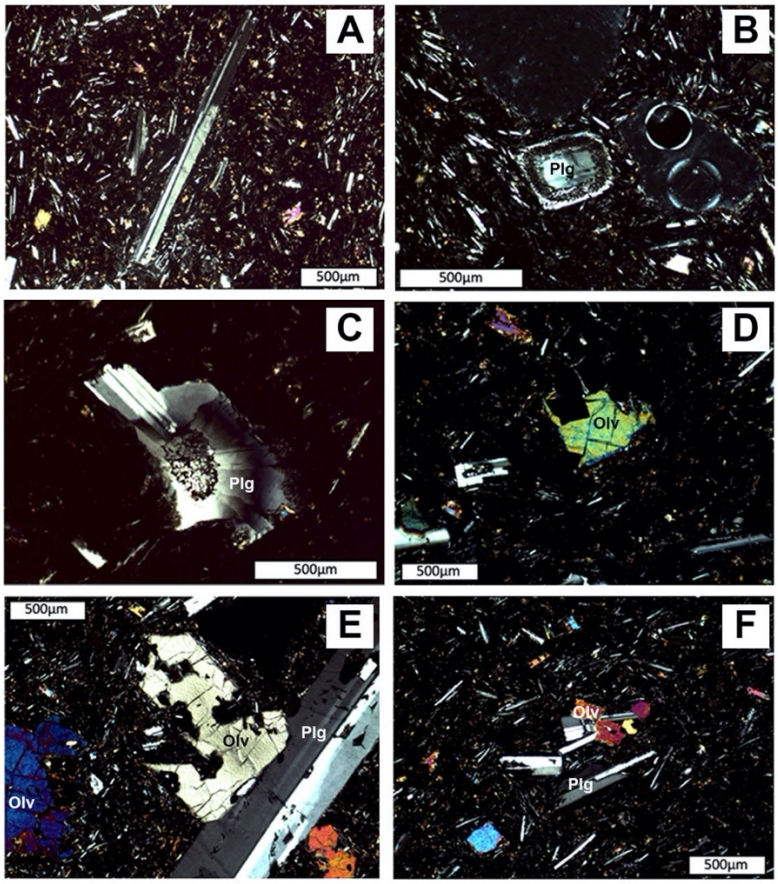

Figure 4.48: *Photomicrographs of the distal Davidson Flow**. A)** Acicular plagioclase in a microcrystalline groundmass. **B,C)** Plagioclase exhibiting a sieve texture. **D)** Olivine crystal with an angular inclusion. **E)** Glomercryst of tabular plagioclase and skeletal olivine, with amoeboid inclusions. **F)** Glomercryst of tabular/acicular plagioclase, subhedral plagioclase and sub-rounded Fe-Ti oxides in a microcrystalline groundmass.*

Proximal Samples

Sample CVYE-AI-18-010 was collected ~1 km from the vent, where the flow diverted around an older, breached scoria cone. The lava is dark grey, sparsely porphyritic and poorly vesicular. The samples contain <1 area% plagioclase phenocrysts, up to 2.3 mm in diameter.

The groundmass is microcrystalline and consist of plagioclase (<400 µm in diameter), olivine (<300 µm in diameter), clinopyroxene (<100 µm in diameter) and Fe-Ti oxides (<500 µm in diameter). Plagioclase crystals are euhedral to subhedral, acicular or skeletal and exhibit a trachytic texture. ~12 area% exhibit resorbed exteriors and they do not contain inclusions. Olivine crystals are euhedral, prismatic and contain spherical opaque inclusions. Clinopyroxene crystals are euhedral to subhedral, rounded, rarely seen under the petrological microscope and do not contain inclusions **(figure 4.49a, b)**. Fe-Ti oxides are mainly sub-rounded and rarely angular.

The phenocryst and microphenocryst assemblage are dominated by plagioclase (~15 area%), followed by olivine (~5 area%). Clinopyroxene microphenocrysts do not occur.

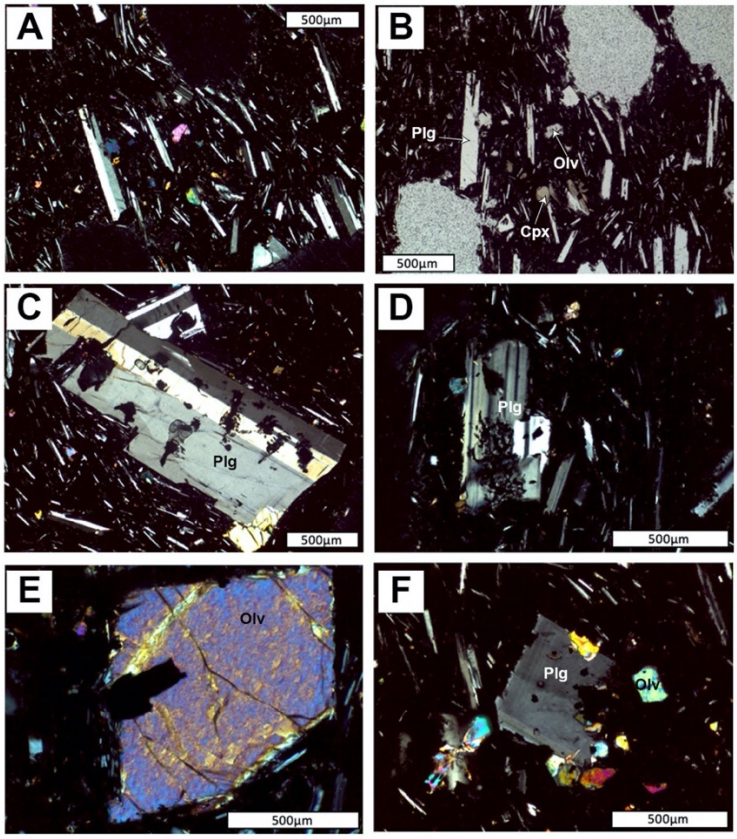

Figure 4.49: *Photomicrographs of the proximal Davidson Flow.* ***A,B)*** *Microcrystalline groundmass of plagioclase, olivine, clinopyroxene and Fe-Ti oxides.* ***C)*** *Subhedral plagioclase with amoeboid inclusions.* ***D)*** *Anhedral plagioclase glomercryst exhibiting a sieve texture.* ***E)*** *Olivine crystal with angular inclusions.* ***F)*** *Glomercryst of tabular/stumpy plagioclase, subhedral plagioclase and sub-angular Fe-Ti oxides in a microcrystalline groundmass.*

Plagioclase

Plagioclase phenocrysts are subhedral, tabular and 1700-2300 µm in diameter **(figure 4.49c)**. ~95 area% have been resorbed and contain elongate and dendritic opaque inclusions. Microphenocrysts are subhedral, acicular and 1200-1700 µm in diameter. ~25 area% exhibit resorbed exteriors and ~15 area% exhibit sieve textures. ~45 area% contain spherical and elongate opaque inclusions. Glomerocrysts, up to 1100 µm in diameter, occur

and are composed of acicular or tabular and externally resorbed plagioclase **(figure 4.49d)**. Their structures are closed with planar contacts.

Olivine

Olivine microphenocrysts are euhedral to subhedral, equant and 300-1100 μm in diameter **(figure 4.49e)**. ~15 area% have been resorbed and they contain spherical opaque inclusions. Glomerocrysts, up to 600 μm in diameter, occur and are composed of olivine, acicular or tabular plagioclase and Fe-Ti oxides **(figure 4.49f)**. Their structures are closed with planar contacts.

North Sisters Flow

Samples CVYE-19 and CVYE-20 were collected from an a'a lava flow, emplaced north-east of Sisters and underlying the Davidson Flow. The extent of the flow and vent location is unknown.

The lavas are dark grey, aphanitic and exhibit a range of vesicularity values: CVYE-19 is incipiently vesicular and CVYE-20 is moderately vesicular. The samples contain <4 area% plagioclase phenocrysts, up to 3 mm in diameter, and <1 area% olivine phenocrysts, up to 2 mm in diameter.

The groundmass is microcrystalline and consists of plagioclase (<400 μm in diameter), olivine (<150 μm in diameter), and Fe-Ti oxides (<300 μm in diameter). Plagioclase crystals are euhedral, acicular or skeletal and exhibit a trachytic texture **(figure 4.50a)**. ~10 area% exhibit resorbed exteriors and opaque inclusions are rare. Olivine crystals are euhedral, prismatic and contain spherical opaque inclusions. In CVYE-20, ~75% of the crystals show partial alteration to iddingsite. Fe-Ti oxides are sub-rounded or sub-elongate and dendritic around the rims of microphenocrysts and microlites.

The phenocryst and microphenocryst assemblage are dominated by plagioclase (~4 area%), followed by olivine (~3 area%).

Plagioclase

Plagioclase phenocrysts are anhedral, resorbed and 1400-3000 μm in diameter **(figure 4.50b)**. They exhibit resorbed exteriors, sieve textures, and contain spherical opaque inclusions. Plagioclase microphenocrysts are euhedral, tabular or stumpy and 500-1300 μm in diameter. ~40 area% exhibit resorbed exteriors and ~50 area% exhibit sieve textures **(figure 4.50c)**. ~50 area% contain amoeboid and spherical opaque inclusions.

Olivine

Olivine microphenocrysts are anhedral, equant and 300-100 μm in diameter **(figure 4.50d)**. ~10 area% have been resorbed and ~40 area% contain spherical opaque

inclusions. In CVYE-20, ~60 area% exhibit alteration to iddingsite around their rims and through cracks **(figure 4.50e)**. Microphenocrysts rarely occur in clusters of anhedral and angular crystals **(figure 4.50f)**. Glomerocrysts, up to 550 µm in diameter, occur and are composed of tabular plagioclase and Fe-Ti oxides **(figure 4.50g)**. Their structures are closed with planar contacts.

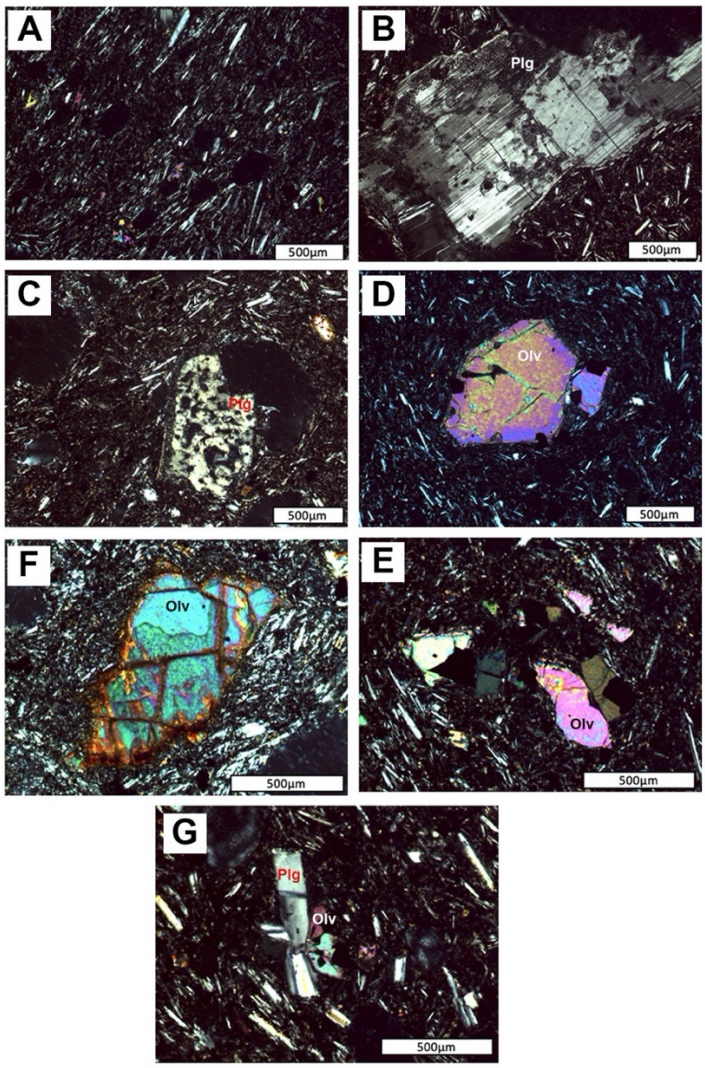

Figure 4.50: *Photomicrographs of the North Sister's Flow**. A)** Trachytic, microcrystalline groundmass. **B,C)** Anhedral plagioclase phenocryst exhibiting sieve textures. **C)** Anhedral plagioclase microphenocryst exhibiting a sieve texture. **D)** Olivine crystal with sub-rounded inclusions. **E)** Anhedral olivine with iddingsite rims and cracks. **F)** Cluster of subhedral to anhedral olivine crystals. **G)** Glomercryst of tabular plagioclase, subhedral plagioclase and sub-angular Fe-Ti oxides in a microcrystalline groundmass.*

South Sisters Flow

Sample CVYE-28 is derived from hawaiite a'a lava flow, named in Preece et al (2018), emplaced south-west of Sisters (Preece et al, 2018; Chamberlain et al, 2019). The flow has a DRE volume of 2.28 x 10^5 m^3 and extends 1.5 km from the base of Sisters peak. It has been dated at 0.51 ± 0.18 ka (Preece et al, 2018) and is the youngest dated lava flow on the island.

The lava flow is medium-dark grey, aphanitic and incipiently vesicular. The samples contain <1 area% plagioclase phenocrysts up to 4 mm in diameter.

The groundmass is microcrystalline and consists of plagioclase (<500 µm in diameter), olivine (<100 µm in diameter), clinopyroxene (<150 µm in diameter) and Fe-Ti oxides (<300 µm in diameter). Plagioclase crystals are euhedral, acicular or skeletal and exhibit a trachytic texture. ~45 area% contain spherical or elongate opaque inclusions. ~10 area% exhibit resorbed exteriors and <15 area% exhibit sieve textures. Olivine crystals are euhedral, prismatic or tabular and contain spherical opaque inclusions. Clinopyroxene crystals are euhedral to subhedral, rarely seen under the petrological microscope and do not contain inclusions. Fe-Ti oxides are sub-rounded or dendritic and form around the rims of microphenocrysts.

Microphenocrysts are rare but the assemblage is dominated by plagioclase (~3 area%), followed by olivine (~1 area%) and Fe-Ti oxides (<1 area%). Clinopyroxene microphenocrysts do not occur.

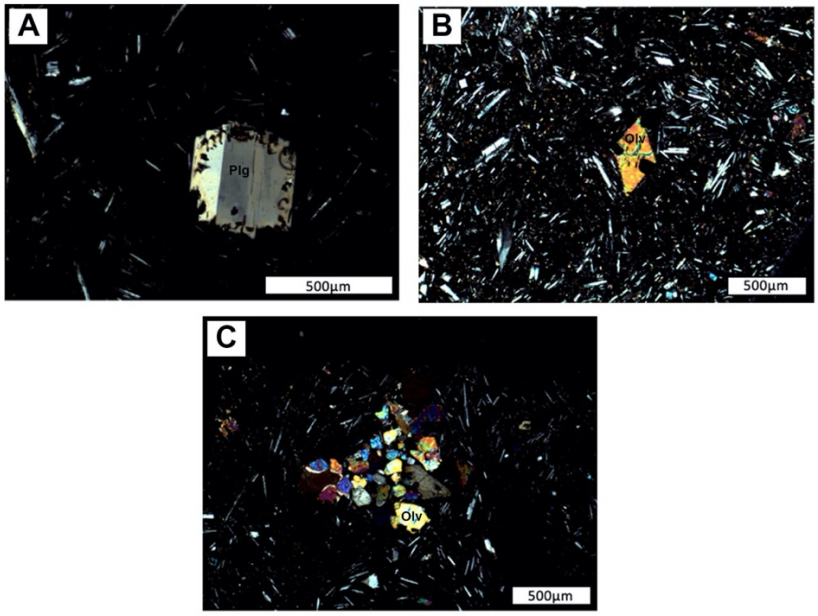

Figure 4.51: *Photomicrographs of the South Sisters Flow. **A)** Anhedral plagioclase with inclusions and exhibiting a sieve texture. **B)** Euhedral olivine with sub-angular, opaque inclusions in a microcrystalline groundmass. **C)** Cluster of subhedral to anhedral olivine crystals.*

Plagioclase

Plagioclase microphenocrysts are euhedral to subhedral, acicular or skeletal and 500-750 µm in diameter. ~55 area% exhibit external resorption and ~15 area% exhibit sieve textures **(figure 4.51a)**. ~55 area% contain elongate and spherical opaque inclusions.

Olivine

Olivine microphenocrysts are subhedral, tabular and 100-700 μm in diameter. ~10 area% have been resorbed and they contain elongate and amoeboid, opaque inclusions **(figure 4.51b)**. Microphenocrysts rarely occur in clusters of sub-rounded crystals **(figure 4.51c)**. Glomerocrysts, up to 200 μm in diameter, occur and are composed of olivine, acicular plagioclase and Fe-Ti oxides. Their structures are closed with planar contacts.

Fe-Ti oxides

Fe-Ti oxide microphenocrysts are angular, skeletal and 300-800 μm in diameter. They contain spherical opaque inclusions.

Comfortless Cove Flow

Samples CVYE-AI-18-060 and CVYE-AI-18-082 are derived from hawaiite a'a lava flow (Chamberlain et al, 2019), named by Weaver et al (1996), emplaced west of Sisters. The flow extends 4 km towards the coast, following old lava channels, and is partially covered by younger tephra fall deposits.

The lavas are medium-dark grey, aphanitic and exhibit a range of vesicularity values: CVYE-AI-18-060 is poorly vesicular and CVYE-AI-18-072 is incipiently vesicular. The samples contain <5 area% plagioclase phenocrysts, up to 8 mm in diameter.

The groundmass is microcrystalline and consists of plagioclase (<500 μm in diameter), olivine (<200 μm in diameter), clinopyroxene (<100 μm in diameter) and Fe-Ti oxides (<500 μm in diameter). Plagioclase crystals are euhedral, acicular, stumpy or skeletal and exhibit trachytic textures **(figure 4.52a)**. ~50 area% have been resorbed and ~40 area% exhibit sieve textures. ~15 area% contain spherical or elongate, opaque inclusions. Olivine crystals are solitary, euhedral, prismatic or tabular. ~80 area% exhibit resorbed exteriors and contain spherical, opaque inclusions. Clinopyroxene crystals are euhedral to subhedral, rarely seen under the petrological microscope and do not contain inclusions. Fe-Ti oxides are subhedral, sub-angular or skeletal and do not contain inclusions.

The microphenocryst assemblage is dominated by plagioclase (~2 area%). Olivine and clinopyroxene microphenocrysts do not occur.

Plagioclase

Plagioclase microphenocrysts are euhedral to subhedral, tabular or acicular and 600-2200 μm in diameter. ~80 area% exhibit resorbed exteriors **(figure 4.52b)** and ~5 area% exhibit sieve textures **(figure 4.52c)**. ~40 area% contain spherical, opaque inclusions.

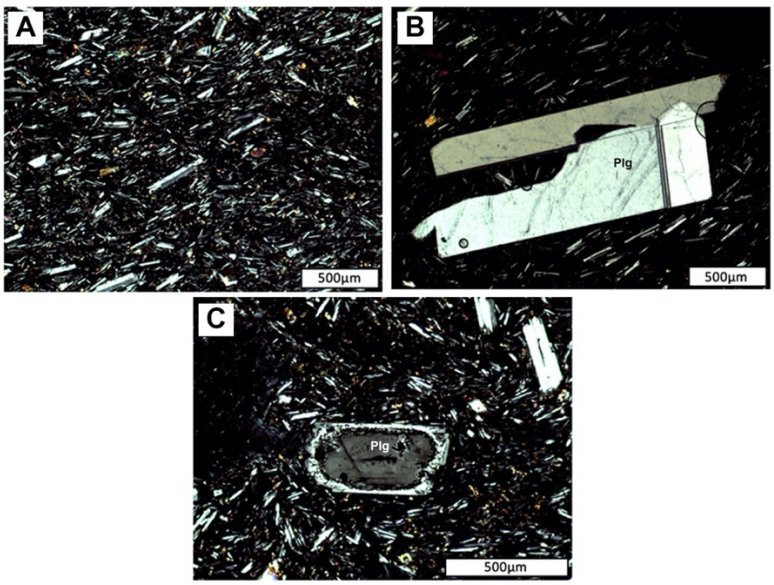

Figure 4.52*: Photomicrographs of the Comfortless Cove Flow.* ***A)*** *Microcrystalline groundmass of plagioclase, olivine, clinopyroxene and Fe-Ti oxides.* ***B)*** *Subhedral, partially resorbed plagioclase.* ***C)*** *Anhedral plagioclase exhibiting a sieve texture.*

Sample		Phenocryst Assemblage	Groundmass Assemblage	Groundmass Textures	Other Features
Unit 1		Plg, Olv	Plg, Olv, Opq	h-xtl	Entrained lithic clasts (<10 area%)
Unit 2		Plg, Olv	Plg, Olv, Opq	h-xtl	
Unit 3 - Pyroclasts	***T1***	Plg, Olv	Plg, Olv, Opq	h-xtl	Entrained lithic clasts (>10 area%)
	T2	Plg, Olv	Plg, Olv, Opq	h-xtl	Entrained lithic clasts (<10 area%)
	T3	Plg, Olv	Plg, Olv, Opq	h-xtl	
Unit 3 – Lithic Clasts	***T1***	Plg, Olv, Opq	Plg, Olv, Cpx, Opq	m-xtl	Plg-Plg G, Plg-Olv G
	T2	Plg, Olv, Opq	Plg, Olv, Cpx, Opq	m-xtl	Plg-Ov G
	T3	Plg, Olv, Cpx	Plg, Olv, Opq	m-xtl	
	T4	Plg	Plg, Opq	h-xtl	Plg-Plg G
	T5	Plg, Olv	Plg, Olv, Cpx, Opq	h-xtl	
Unit 4		Plg, Olv	Plg, Olv, Opq	h-xtl	Plg-Olv G
Davidson Flow (proximal)		Plg, Olv	Plg, Olv, Cpx, Opq	m-xtl, h-xtl trachytic	Plg-Plg G, Plg-Olv G
Davidson Flow (distal)		Plg, Olv	Plg, Olv, Cpx, Opq	m-xtl	Plg-Olv G
North Sisters Flow		Plg, Olv	Plg, Olv, Opq	m-xtl trachytic	Olv alteration
South Sisters Flow		Plg, Olv, Opq	Plg, Olv, Cpx, Opq	m-xtl, trachytic	Plg-Olv G
Comfortless Cove Flow		Plg	Plg, Olv, Cpx, Opq	m-xtl	

Table 4.3: *For comparison and summarising the petrographic properties of the Sisters tephra and lava flows. T – type, Plg – Plagioclase, Olv – Olivine, Cpx – Clinopyroxene, Opq – Opaque minerals, h-xtl – hypocrystalline, m-xtl – microcrystalline. G – glomerocryst.*

5. Interpretations

5.1 Unit 3 evolution

5.1.1 Type 3 pyroclasts

The type 3 pyroclasts **(figure 4.8c)** are golden brown, highly vesicular and are inferred to have formed in the centres of Hawaiian lava fountains, where their exteriors quenched while their interiors expanded and increased the vesicularity. The presence of microlite-poor (<5%) sideromelane glass indicates that the magma rose rapidly to the point of fragmentation and therefore contains a lower proportion of microlites and expanding bubbles (Taddeucci et al, 2004; Lautze and Houghton, 2007; Ginibre et al, 2007). Their morphologies are inferred to represent ductile deformation (e.g. Lautze and Houghton, 2005; Di Traglia et al, 2009; Kósik et al, 2016).

5.1.2 Type 2 pyroclasts

The type 2 pyroclasts **(figure 4.8b)** are inferred to have formed in the margins and lower parts of Hawaiian lava fountains and/-or in Strombolian explosions. Their thin, black, glassy exteriors imply rapid quenching and their high internal vesicularity implies rapid bubble nucleation and expansion. The presence of microlites (~35%) infers the magma ascended slowly and allowed more time for cooling (Polacci et al, 2006). Their morphologies are inferred to represent ductile deformation during ejection (e.g. Lautze and Houghton, 2005; Di Traglia et al, 2009; Kósik et al, 2016). The stretched filaments and vesicles observed in some type 2 pyroclasts are inferred to represent shearing due to magma ascending close to the conduit margins (Romero et al, 2018).

Vesicularity

The type 2 and 3 pyroclasts exhibit higher vesicularity values than typical Strombolian tephra (e.g. Polacci et al, 2006; Lautze and Houghton, 2007; Di Traglia et al, 2009) and sit in the higher bounds of Hawaiian tephra fall deposits (e.g. Houghton and Wilson, 1989; Polacci et al, 2006; Di Traglia et al, 2009). The high vesicularity suggests the magma underwent rapid bubble nucleation and expansion, with rapid quenching, as seen during fountaining events (e.g. Polacci et al, 2006; Parcheta et al, 2013).

The vesicularity range observed in low viscosity, basaltic magmas is expected to be broad due to the ease of mobility of bubbles (Houghton and Wilson, 1989). Type 2 and type 3 pyroclasts exhibit a narrow range, implying moderate to high fountaining events, where the bubbles were unable to migrate through the magma due to rapid ascent rates (Houghton and Wilson, 1989; Parcheta et al, 2013).

5.1.3 Type 1 pyroclasts

The type 1 pyroclasts are different from the type 2 and 3 pyroclasts. They have dull, granular and wrinkled surfaces and a prolate shape **(figure 4.8a)**. The presence of mineral precipitates, adhering ash particles and lithic clasts covering the majority of the surfaces implies the presence of liquid water (Dellino et al, 2001). Therefore, it is inferred that the pyroclasts formed during weak phreatomagmatic activity. The equant and platy shapes of the pyroclasts imply that they formed over a larger bubble that burst rapidly and became partially folded and wrinkled during transportation. The irregular shaped vesicles infers rapid degassing of the magma prior to eruption and a longer residence in the conduit for vesicles to coalesce (Lautze and Houghton, 2005; Parcheta et al, 2013).

The presence of plagioclase, olivine, clinopyroxene and Fe-Ti oxides in the microlite-rich domains, compared to plagioclase, minor olivine and Fe-Ti oxides in the microlite-poor domains (e.g. **figure 4.17)** implies the tephra contains clasts of lithic fragments that became entrained in the magma during ascent, most likely from the conduit walls (Houghton et al, 2004). These lithic fragments exhibit almost identical textures to the lava textures described previously. Therefore, it is implied that they are wall rock fragments that were incorporated into the pyroclasts during a more energetic eruption, which I infer to be of a weakly phreatomagmatic origin.

One hypothesis for the formation of the precipitates and attached clasts on the surface of the pyroclasts is that they impacted and became stuck or welded. However, for this to happen, there must have been a change in the eruption conditions that included an increase in energy, allowing the pyroclasts to collide at greater speeds.

An alternate hypothesis is that the precipitates formed in the plume, and the adhering particles are stuck via electrostatic forces or hydrostatic forces (e.g Dellino et al, 2001; Sánchez et al, 2015; Mueller et al, 2016; Mueller et al, 2017; Colombier et al, 2019). Electrostatic bonds are weak (Mueller et al, 2016) and the particles were not removed by washing in an ultrasonic bath. Thus, electrostatic forces can be dismissed. Instead, I infer that the particles adhered via interstitial precipitation of various minerals during the evaporation of liquid coatings (Mueller et al, 2016).

However, it might be expected that the precipitates and adhered clasts would form on top of the Pele's hair, which forms from intense gas bursts or at the edges of fire fountains (Sánchez et al, 2015). For these pyroclasts, this is not the case; Pele's hair shows a variation of rigid attachments and semi-molten attachments **(figure 4.15b,c)** which means they must have been semi-molten at the time of impact, and therefore adhered within or extremely close to the vent and not in the plume. Therefore, it is inferred that the adhered clast formed as follows: Magma fragmented during weak water-magma interaction. The water acted as a catalyst for precipitate formation and minerals began to precipitate on the adhered clasts due to diffusion of Na and Ca out of the volcanic ash and reactions with HCl

and SO_2 in the gas column. At the same time, smaller clasts stuck to the surfaces of the larger clasts due to interstitial precipitation of minerals during evaporation of liquid bonds (e.g. Mueller et al, 2016). Pele's hair was simultaneously produced from intense gas bursts and adhered to the pyroclasts. As the pyroclasts entered the plume, precipitates formed on top of the Pele's hair and on the pyroclast surface.

5.1.4 Lithic clasts

The lithic clasts are petrographically similar to lava flows around the SSCC. They are inferred to have two origins: The first is from the conduit walls, where remnants of a previous magma batch cooled before an explosive eruption caused it to fragment and become entrained into the exploding gas column (e.g. Houghton et al, 2004). The second is from vent clearing events, following collapses of the inner cone walls which block the vent (e.g. Houghton and Schmincke, 1989).

The abundance of Fe-Ti oxides in the lithic clasts and lithic fragments implies that the pyroclasts have been reheated (D'oriano et al, 2014). The dendritic oxides around crystal edges formed by heterogeneous nucleation under high oxidising conditions (D'oriano et al, 2014). The heavily altered plagioclase textures in the red lithic clasts **(figure 4.35)** have not yet been described in the literature. I infer that these textures are the products of pseudomorphic mineral replacement reactions due to hydrothermal alteration (e.g. Xia et al, 2009), however, further research into these textures and their formation is needed.

5.1.5 Eruption scenario for Unit 3

The Unit 3 deposit begins as a massive and coarse-grained deposit and transitions upwards to a stratified and poorly-sorted deposit **(figure 4.6a)**. It also shows vertical variation in the abundance of the different clast types **(figure 4.9a,b).** From the stratigraphy it is possible to split the eruption into three distinct phases represented by 3 sub subunits (lower, middle and upper).

The Unit 3 deposit is dispersed towards the north/ north-west and has a volume of 4.9×10^5 m^3. However, the extent of tephra dispersal into the sea is unknown, therefore the volume of the Unit 3 deposit could be larger than originally thought.

The lower subunit is locally dispersed to the north-west, reaches ~0.9 km from the vent and is inferred to represent a lava fountaining phase. The middle subunit is most widely dispersed towards the north and north-west and reaches more than 3.6 km from the vent. The upper subunit is only dispersed to the west and reaches up to 2.2 km from the vent.

The varying dispersal between subunits implies that the eruption intensity varied and that the wind direction showed weak variation over the duration of the eruption.

Lower subunit

The coarse-grained, highly vesicular, fluidal-shaped and well-sorted beds that dominate the lower subunit are inferred to represent an episode of open-vent, Hawaiian fountaining **(figure 5.1a)**, with low rates of inertial fragmentation driven by rapid vesiculation (e.g. Mangan and Cashman, 1996; Houghton and Gonnerman, 2008; Namiki and Manga, 2008; Liu et al, 2017). This implies that the magma ascended rapidly (Parfitt and Wilson, 1995)**.** The limited dispersal of this subunit suggests that the fountain reached no higher than 500 m (e.g. Mueller et al, 2018). This was still high enough for highly vesicular pyroclasts to form in the centre (e.g. Stovall et al, 2011). The appearance of red lithic clasts, the decrease in grain size of the type 2 pyroclasts, the decrease in the abundance of type 3 pyroclasts, and the change to moderately sorted beds at the top of the subunit implies the fountain heights decreased before transitioning from Hawaiian fountaining to Strombolian explosions.

Middle subunit

The middle subunit is characterised by medium- to coarse-grained, fluidal-shaped pyroclasts and moderately sorted beds that record a transition from lava fountaining to open-vent Strombolian activity **(figure 5.1b)** (e.g. Houghton and Schmincke, 1989). This indicates that the speed of magma ascent lowered but the discharge rate remained high, allowing the rising bubbles to coalesce and form gas slugs (Verginolle and Jaupart, 1986; Parfitt and Wilson, 1995; Parfitt, 2004). It also indicates that the fragmentation efficiency increased in response to the higher decompression rates (e.g. Di Traglia et al, 2009). Thin layers of coarse and ragged ash are inferred to represent short breaks in eruptive activity that allowed fine material to settle. Thin and poorly sorted layers of fine lapilli and coarse ash are inferred to represent a weakening eruption and decline in the mass discharge rates.

The appearance of type 1 pyroclasts in the middle of the subunit represents a change in conditions at the point of fragmentation. This is inferred to be intermittent interaction with small volumes of groundwater.

Upper subunit

In the third section, the stratified, fine-grained, poorly-sorted, ash-rich beds are inferred to represent a series of closely spaced, weak and impulsive, phreatomagmatic explosions **(figure 5.1c)**. The presence of ash particles implies elevated fragmentation efficiencies which are commonly observed during magma-water interactions (Sheridan and Wohletz, 1981; Houghton and Hackett, 1984; Wohletz, 1986; Liu et al, 2017). This is due to the brittle breakage in response to higher rates of thermal to mechanical energy transfer

when the magma and water interact (Di Traglia et al, 2009; Liu et al, 2017). The abundance of lithic clasts at the base of the phreatomagmatic subunits and the non-systematic, heterogeneous componentry of juvenile and lithic clasts, also imply the onset of more explosive activity. I infer that as the magma discharge rate declined, a limited amount of water was able to access the conduit and explosively interact with the magma (e.g Houghton and Schmincke, 1989; Alvardo and Schmincke, 2013). The layer of fine-medium lapilli separating the two stratified subunits is inferred to represent a new influx of magma that increased the mass discharge rate and led to a short period of Strombolian explosions before decreasing again.

The upwards change from massive to stratified beds is also consistent with phreatomagmatic activity and records a transition to unsteady eruption dynamics. Unsteadiness is a strong indicator of phreatomagmatic activity as magma-water interaction is typically pulsatory (Houghton et al, 2015). During lava fountain events, the mass discharge rate is high, preventing water and magma interacting. However, after lava fountain events, the magma discharge decreases (e.g. Bertagnini et al, 1991), lowering the pressure in the conduit and allowing an influx of water (Houghton and Schmincke, 1989; Alvardo and Schmincke, 2013). Partial collapse of the vent walls after Strombolian explosions or strong lava fountains can also cause a drop in the discharge rate (Bertagnini et al, 1991, Guttmann, 2002; Alvardo and Schmincke, 2013). These actions cause the pressure in the conduit to drop below the hydrostatic pressure in the aquifer, allowing an influx of water (Alvardo and Schmincke, 2013). Unsteadiness can also be caused by the weakening of the eruption or by gas segregation and upward gas migration in the conduit, which causes the magma-gas mixture to alternate between a stable and the two-phase flow regime (Pioli et al, 2008). However, it is unclear how this mechanism could lead to the changes in pyroclast textures identified in Unit 3.

Strong evidence for a change in the eruption style can be seen in the alternating, cm scale, layers of type 1 and 2 pyroclasts. Therefore, the difference in surface textures, clast morphology, lithic clasts, abundance and initial vesicle shapes suggests that the eruption transitioned from magmatic to phreatomagmatic.

5.2 Other Sisters tephra deposits

Four tephra samples record Hawaiian, Strombolian and weakly phreatomagmatic activity that dispersed tephra over the north/ north-west of the island. Stratigraphy from Units 2 and 4 imply the eruption sequences followed similar processes to that described for Unit 3 **(figure 4.6),** and that the scoria cones were built up from Strombolian explosions and sustained Hawaiian lava fountains.

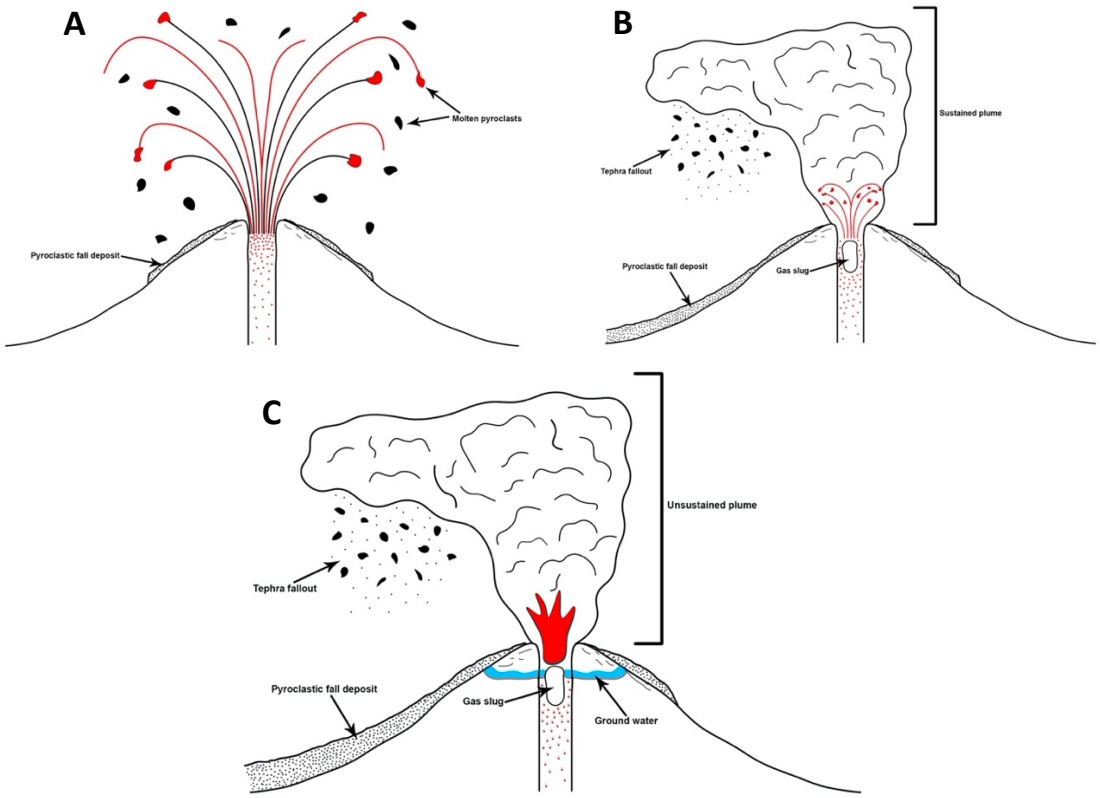

Figure 5.1: *Schematic diagrams of the three eruptive phases during the Unit 3 eruption.* ***A)*** *Hawaiian lava fountaining.* ***B)*** *Strombolian explosions with a sustained plume.* ***C)*** *Weakly phreatomagmatic eruptions with an un-sustained plume.*

Based on stratigraphy only, Unit 2 **(figure 4.4)** is inferred to have begun with Strombolian explosions, separated by short periods where ash was able to settle. The normal grading of the middle and upper beds suggests the intensity of the eruption began to wane, and the stratified appearance suggests the eruption or plume dynamics became unsteady. Fine lapilli and ash beds at the top of the sequence infer the end of the eruptive phase.

The lower section of unit 4 **(figure 4.5)** contains abundant lithic clasts and alternates between fine scoria and ash, suggesting that the influx of water observed towards the end of Unit 3 still played a critical role in driving the eruption, as has been inferred elsewhere (e.g. Houghton and Schmincke, 1989). Inverse grading half-way up the sequence suggests that the eruption increased in intensity, and the presence of dense lithic clasts and ash coated clasts suggests the presence of water triggered the increase in intensity. The sudden decrease in lithic clasts and the increase in ragged scoria clasts, implies the eruption transitioned from a phreatomagmatic to a magmatic origin. Beds of massive and medium lapilli scoria infer Strombolian explosions, separated by short time periods where ash layers were able to settle. The decreasing lapilli size and increasing ash content at the top of the sequence infers the eruption began to wane before ending completely. The lack of soil development between the individual units cannot be used as an indicator for breaks in eruptions because the island's arid environment inhibits rapid soil development.

6. Discussion

6.1 Sisters scoria cone complex

The SSCC is formed of a number of scoria cones and lava flows. The cones are aligned on E-W trending structures which allowed multiple dyke propagations to the surface. Two lavas from the SSCC have been dated at 1.64 ± 0.37 ka and 0.51± 0.18 ka (Preece et al, 2018), implying that they were not erupted synchronously, and therefore must represent temporally separate magmatic events.

Scoria cone 1 is considered to be the oldest due to its orangey-red colour, weathered appearance and abundant vegetation. **(figure 4.1)**. The cone has two craters, indicating that volcanic activity was focused at two vents during its active period. Lava flows have not yet been identified for this cone, and the eruption may not have had an effusive phase.

Scoria cone 2 formed ~800 m west of the crater of cone 1 **(figure 4.1a)**. The asymmetrical north-western flank of the cone suggests that the tephra deposition was strongly influenced by prevailing south-easterly winds. At least two lava flows originated from vents at the northern and western base of the cone **(figure 6.1a)**.

Scoria cone 3 was constructed by an eruption that occurred within the crater of cone 2 **(figure 6.1b)**. A lava flow is inferred to have originated from the base of its southern flank. Cone 3 is inferred to have been similar in size to cone 2 but was mostly destroyed or buried by scoria cone 4, therefore, the exact location of the cone 3 vent is not known.

Scoria cone 4 was constructed over the lower flanks of cones 2 and 3 and covered the western flank of cone 1. Two lava flows are linked to cone 4. The first originated from a vent within the crater **(figure 4.3)** and flowed down the north flank, causing a breach, before it diverted around an older scoria cone. The second originated from a vent at the base of the southern flank **(figure 6.1c)**. This flow is believed to be the last lava flow produced at Sisters and represents the most recent activity on the Island (Preece et al, 2018).

The tephra fall deposits and lava flows are petrographically similar **(table 4.3),** and it is not yet possible to correlate individual fall deposits with the lava flows or scoria cones.

It is inferred that the eruptions from the SSCC were of similar size. The scoria cone volumes range from 1.7 - 6 x 10^7 m^3, which is at the larger end of scoria cone sizes and is within the same order of magnitude as Red Mountain and Sunset Crater scoria cones (e.g. Riggs and Duffield, 2008). However, the scoria cone 4 volume (with no cone overlap) is within the same order of magnitude as scoria cones from Mt Etna, Cerro Negro and Izu-Oshima (e.g. Hill et al, 1998; Sumner, 1998; Fornaciai et al, 2010) which are more common scoria cone sizes (Németh and Kereszturi, 2015; Pyle, 2015). The lava flows range in volume from 4.6 x 10^5 – 1.18 x 10^7 m^3 which are similar to scoria cone lava flows on Mt

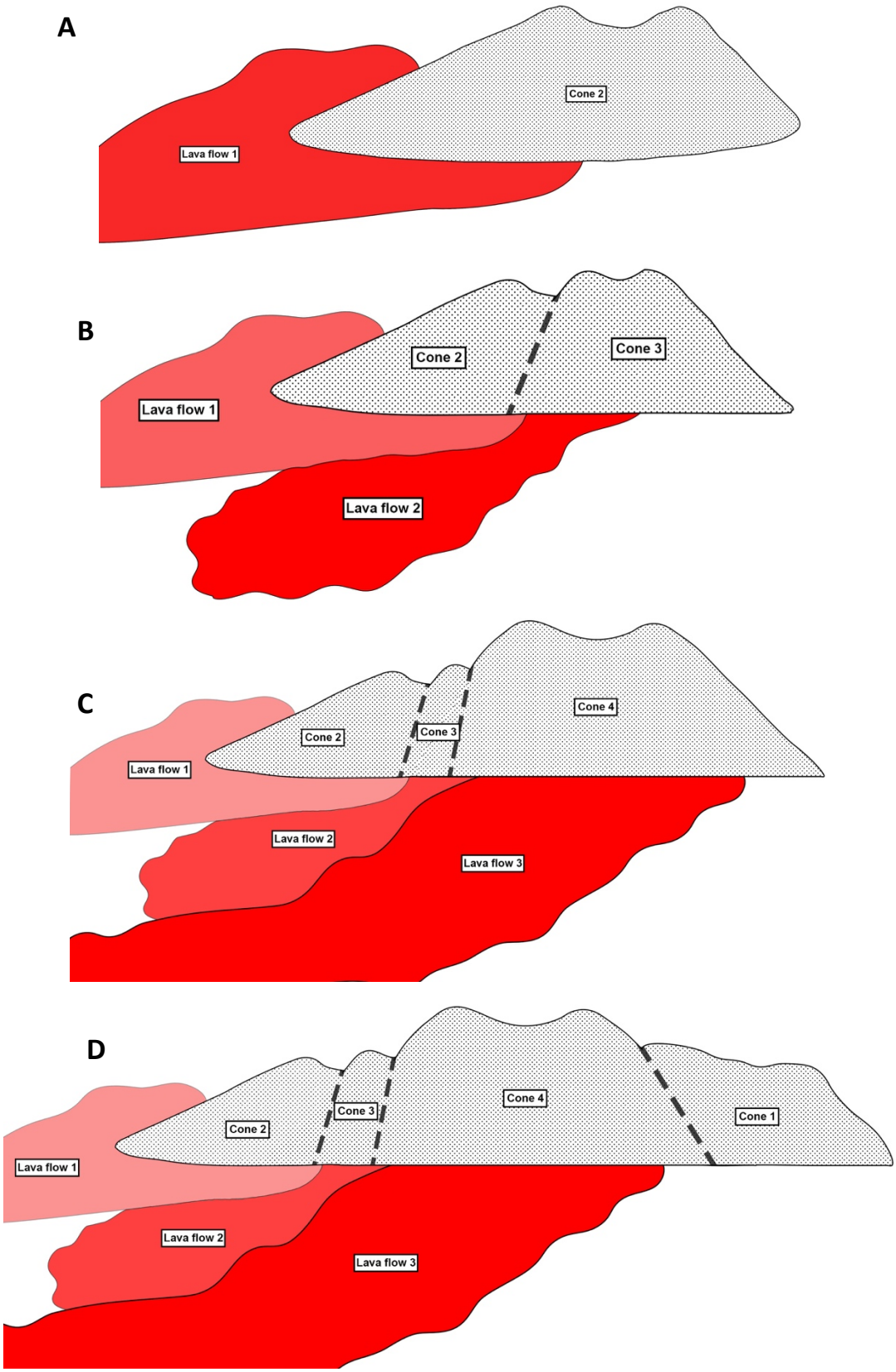

Figure 6.1: *Schematic diagrams showing the evolution of the Sisters scoria cone complex, including scoria cone development and lava flow distribution. Looking north.* ***A)*** *Stage 1: growth of scoria cone 2 and the first lava flow.* ***B)*** *Stage 2: growth of scoria cone 3 through the crater of scoria cone 2 and the second lava flow.* ***C)*** *Stage 3: growth of scoria cone 4 through the crater of scoria cone 2/3 and a further lava flow.* ***D)*** *The Sisters scoria cone complex and associated lava flows, with scoria cone 1 present to show its relationship with scoria cone 4.*

Etna (e.g. Stevens et al, 1999) but up to two orders of magnitude smaller than lava flows from scoria cones at Lathrop Wells and Los Morados (e.g. Valentine et al, 2005; Németh et al, 2011). The volume of Unit 3 tephra is similar to eruptions from Mt Etna and Cerro Negro (e.g. Hill et al, 1998; Andronico et al, 2008; Fornaciai et al, 2010), but is an order of magnitude smaller than eruptions from the Azores, Auckland Volcanic Field and Croscat scoria cone (e.g. Booth et al, 1978; Magill et al, 2006; Di Traglia et al, 2009).

The erupted DRE volumes are within the same order of magnitude (10^6 m^3) as other monogenetic basaltic eruptions (e.g. Di Traglia et al, 2009; Paulick et al, 2009; Fornaciai et al, 2010; Mattsson, 2012). This converts to a total erupted tephra volume of 0.001 km^3 and a VEI magnitude of 1 (Newhall and Self, 1982).

The close proximity of the vents and the continuous activity along the fissure to form the overlapping scoria cones could represent the onset of the development of a composite volcano.

6.2 Phreatomagmatic activity at Sisters

Phreatomagmatic eruptions result in a range of features and deposits depending on the amount and location of water involved in explosions (Walker, 1973; Sheridan and Wohletz, 1983; Wohletz and Sheridan, 1983; Houghton and Schmincke, 1989; Houghton et al, 2015; Kósik et al, 2016). It can be difficult to infer phreatomagmatic activity based only on features of the eruptive products and commonly, multiple lines of evidence need to be assembled (White and Valentine, 2016). I infer that the upper subunit of Unit 3 records only very limited interaction of magma with ground water i.e., the explosions were only weakly phreatomagmatic. To my knowledge, this is the first time that such feeble activity has been recognised and I have yet to find documentation of comparable deposits.

Phreatomagmatic eruptions of basaltic magma typically construct tuff rings, tuff cones or maar volcanoes (Walker, 1973; Sheridan and Wohletz, 1983; Kósik et al, 2016). Their deposits are generally poorly sorted and contain abundant fine ash due to an increased fragmentation efficiency of magma-water interaction (Walker, 1973; Sheridan and Wohletz, 1983; Barberi et al, 1989; Koyaguchi and Wood, 1996; Liu et al, 2017; Swanson and Houghton, 2018). The ash layers are 'wet', cohesive and can contain abundant ash aggregates (Walker, 1973; Sheridan and Wohletz, 1983; Kósik et al, 2016). The deposits are also characterised by an abundance of lithic clasts (60-90 wt%) (Houghton and Smith, 1993) and ballistics due to the destruction of the aquifer (Sheridan and Wohletz, 1983; Koyaguchi and Wood, 1996). Pyroclastic density currents (PDC's) are commonly associated with phreatomagmatic deposits due to dense water and lithic clast-rich plumes collapsing (Walker, 1973; Koyaguchi and Wood, 1996; Houghton et al, 2015).

Many phreatomagmatic eruptions are modifications of explosive eruptions that would have occurred in the absence of external water (Houghton et al, 2015). The interaction with water can be intermittent and the degree of water interaction can vary, with some eruptions triggered by water entering through fractures within the wall rocks and some by water trapped in porous and permeable frameworks (e.g. Wohletz and Sheridan, 1983; McPhie et al, 1990; Dzurisin et al, 1995; Houghton et al, 2015). Monogenetic basaltic eruptions can have phases of magmatic activity and phreatomagmatic activity or can transition from one to the other over time (e.g. Houghton and Hackett, 1984; Houghton and Schmincke, 1989; Houghton et al, 1996; Di Traglia et al, 2009; Mattsson and Höskuldsson, 2011).

The deposits that are inferred to be phreatomagmatic in Unit 3 do not exhibit evidence for strong phreatomagmatic activity, as outlined above. Instead, they exhibit (1) a change from massive, coarse-grained and well sorted scoria to stratified, fine-grained and poorly-sorted scoria, (2) an upwards increase in lithic clasts, (3) a change in surface textures of the pyroclasts and (4) the presence of the inclusions of lithic clasts within type 1 pyroclasts. I interpret these to represent very minimal phreatomagmatic activity: there are no other reasonable changes in the eruption dynamics that could account for the changes in bedding, sorting, grain-size, clast textures and lithic clast inclusions.

At the SSCC, it is inferred that the phreatomagmatic activity was limited in size and occurred during lulls in the magmatic activity. Whilst magma was actively vesiculating and discharging from the vent, the role of external water was minor and restricted to occasionally increasing the degree of fragmentation and explosivity during ‘dry’ eruptions (e.g. Houghton and Schmincke, 1986; Houghton et al, 1999).

This lower end of phreatomagmatic activity in basaltic eruptions has, to the best of my knowledge, not yet been inferred for basaltic eruptions. The criteria currently used for distinguishing magmatic from phreatomagmatic activity mainly focuses on a particular set of clast characteristics, which is problematic because sometimes the characteristics can result from other processes (White and Valentine, 2016). Therefore, it is recommended that future work into basalt eruptions look for features in the eruption sequence and pyroclasts that could represent minimal water-magma interaction.

6.3 Tephra dispersal and hazards

SSCC is the youngest volcanic centre on the island (Preece et al, 2018). The data presented in this thesis enables a more complete assessment of the hazards from future eruptions at SSCC.

Analysis of the Unit 3 deposit within this thesis infer that the deposit represents an explosive, basaltic eruption, with styles varying from Hawaiian lava fountains, Strombolian

explosions and weak phreatomagmatic explosions. The Unit 3 deposits are dispersed to the west and northwest of the vent and cover a minimum 24 km^2 of the island. The deposit thins away from the vent, and slight changes in thickness closer to the vent represent a variation in the dispersal axis. However, the true extent of the dispersal is unknown due to the proximity to the coast.

The greatest hazard imposed from a similar eruption from SSCC is tephra fall out. Wind data **(figure 6.2)** shows that the prevailing winds on Ascension Island exhibit little variations in wind direction. Therefore, it is expected that tephra would be dispersed towards the north-west, following the south-east to north-west prevailing winds.

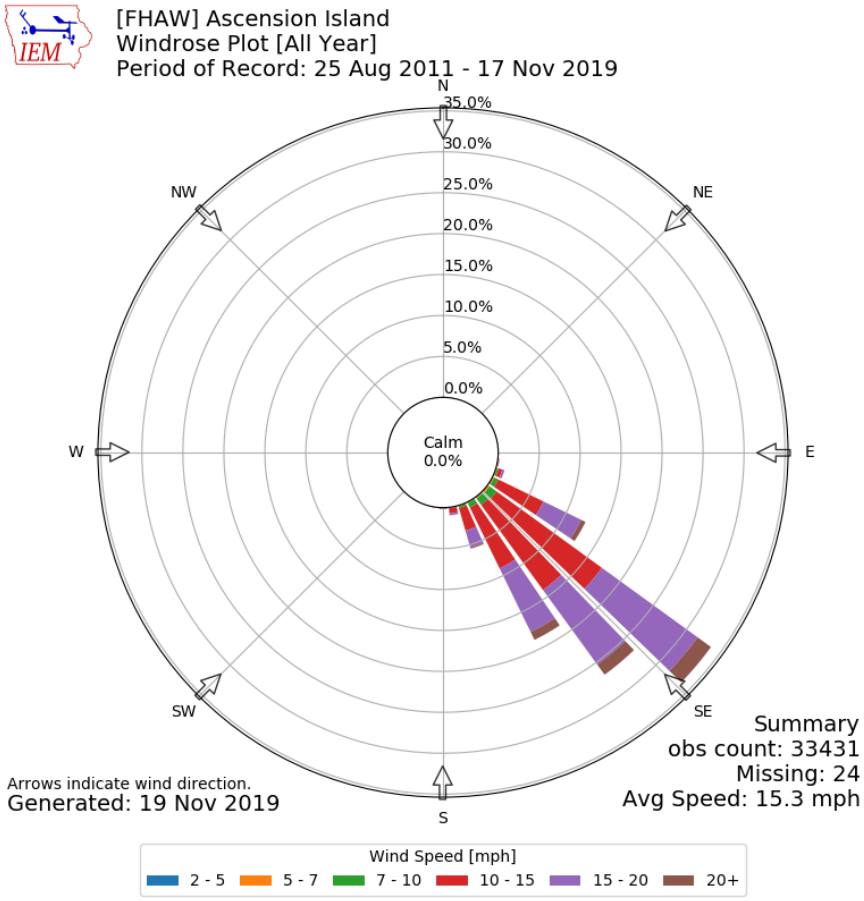

Figure 6.2: *Rose diagram showing the yearly distribution of the prevailing winds on Ascension Island. Wind data from 25-Aug-2011 00-00-00 to 17-Nov-2019 00-00-00 (Herzmann, 2019).*

The models **(figure 4.41, 4.42)** estimate that, at worst case scenario, Georgetown could receive between 25-75 cm of ash accumulation (100-300 kg/m^2). However, measured data **(figure 4.39)** showed that the previous eruption deposited ash up to 10 cm thick (40 kg/m^2). Tephra fallout on buildings requires clean up actions when the accumulation exceeds ~1 kg/m^2 (Biass et al, 2017). Thicker accumulations of tephra (>100 kg/m^2) will cause ash infiltration and roof collapse (Jenkins et al, 2015**;** Biass et al, 2017), whilst accumulations of 3-6 kg/m^2 will cause electrical insulators to collapse and increases the risk of flashovers (Wardman et al, 2012).

Scoria cone eruptions can range in duration from hours to months and sometimes years (e.g. Wood, 1980; Houghton and Nairn, 1991; Hill et al, 1998; Neal et al, 2019).The duration of the eruptions from the SSCC is unknown, however, dating of three flows within ~1000 years of each other (Preece et al, 2018) implies that the eruptions occurred in a closely spaced time period. Longer eruption periods would lead to an increase in tephra fallout and ash accumulation on infrastructure due to changing wind directions (e.g. Houghton et al, 1987). However, long eruptive periods do not always mean that the area presents the greatest volcanic hazard (e.g. Simkin and Siebert, 1981; Blong, 2013) because short duration eruptions can be strongly fed and produce large magma volumes (between 40 – 78 x 10^6 m^3) (e.g. Andronico and Lodato, 2005).

Previous eruptions have led to the build-up of a new scoria cones, so it must be considered that a new eruption has the potential to create a new cone. Two Boats village is 0.9 km from the SSCC which means there is the possibility of future scoria cone growth in the area. There is also a possibility that if eruptions continue to be focused in within the SSCC it will build-up into a composite volcano.

The presence of fresh lava, with no historical observations, heightens the risk from volcanic eruptions on Ascension Island (Preece et al, 2018) and due to the critical military infrastructure on Ascension Island, and the proximity of towns and local amenities to Sisters, there is a great need to better understand the rates of accumulation on the surrounding areas and make mitigation plans to reduce negative impacts relating to tephra fall.

Lava flows mainly originate from the base of the scoria cones with at least one originating within a cone. They vary in volume, from 4.6 x 10^{-4} to 1.19 x 10^{-2} km^3, and flow up to 3.5 km to the north-west coastline. The youngest flows are inferred to have a random flow orientation, whilst some of the older flows flowed down channels. The flows have similar composition (Nielson and Sibbett, 1996; Weaver et al, 1996; Jicha et al, 2013; Preece et al, 2018; Chamberlain et al, 2019) and so it is inferred that they had similar effusion rates. Therefore, it is not possible to predict an exact flow path and volume of a future lava flow from the SSCC. However, considering previous eruptions, it is inferred that Georgetown and Two Boats are within safe distances from future lava flows, but the island's powerplant is at risk.

Phreatomagmatic eruptions are dangerous and can happen with very little warning due to the mixing of ground water and magma (Lorenz, 1987). Two Boats village is ~0.9 km from the vent **(figure 2.3)** and is at greatest risk from ballistic fallout. Ballistic clasts can reach up to 1 km from the vent and impact at high velocities (e.g. Houghton et al, 1987; Dellino et al, 2011). The impact energies of the ballistics range from ~10^6 J in areas up to 0.3 km from the vent and ~10^5 J up to 1 km from the vent (e.g. Dellino et al, 2011). These energies suggest that any building within this vicinity will sustain major damage (Houghton et al, 1987; Dellino et al, 2011).

7. Further study

In order to fully understand how this complex evolved further study is recommended.

- It is suggested that each tephra fall deposit is mapped and measured, in order to calculate volumes and understand any dispersal patterns.
- Correlating lavas to tephra and tephra layers to scoria cones is not yet possible, based on data presented in this thesis. Major and trace element geochemistry of the tephra deposits and lavas is needed to try and do this.
- Radiometric dating of the lava samples (e.g. Preece et al, 2018) and tephra would aid in the correlation and the understanding of the time-scales involved in the evolution of the SSCC.
- Geochemical analysis of the mineral precipitates would determine their composition and aid in understanding the mechanisms of their formation.

8. Conclusions

This study carried out a detailed analysis of a scoria fall deposit (Unit 3) from the SSCC and provided a preliminary insight into the growth of the SSCC. Granulometry, componentry and textural studies indicate that the Unit 3 eruption began with sustained Hawaiian lava fountains, before transitioning into Strombolian eruptions and alternating, weak phreatomagmatic activity due to a decrease in mass discharge rates towards the end of the eruptive phase. The different eruption styles resulted in contrasting deposits:

1. Hawaiian style eruptions: well sorted, coarse-grained tephra composed of fluidal-shaped, stretched, light-brown and black glassy, highly vesicular scoria.
2. Strombolian style eruptions: moderately well sorted, medium-grained tephra, composed predominantly of fluidal, stretched, black glassy and highly vesicular pyroclasts and <5% lithic clasts.
3. Weakly phreatomagmatic eruptions: poorly sorted, fine-grained and stratified tephra, containing equant, platy, ash-coated scoria and abundant lithic clasts (>10%).

Tephra was dispersed to the north-west of the island. Probability maps show that Georgetown has a 10% chance of up to 75 cm of ash accumulation, but a 90% chance of < 2.5 mm of ash accumulation from a similar eruption in the future.

The SSCC is composed of the products of a number of monogenetic, Hawaiian and Strombolian style eruptions. These eruptions constructed scoria cones and produced lava flows and tephra fall deposits. Due to petrographic similarities between tephra samples and the lava samples, it was not possible to correlate individual fall deposits with its associated lava flow, using only textural analysis.

Appendices

Appendix 1

Input Parameter	Sister's Peak	Input Parameter	Sister's Peak
Vent		*Wind*	
Vent Easting	569309	Number of wind files	14608
Vent Northing	9123916	Wind start	01-Jan-2005 00:00:00
Vent UTM zone	-28		
Vent Height (m asl)	413		
		Winds per day	4
		Seasonality	0
		Wind start rainy	
		Wind start dry	
Eruption		*Tephra2 Model*	
Minimum total erupted mass (kg)	$2x10^9$	Eddy constant m^2 s^{-1}	0.04
Maximum total erupted mass (kg)	$2x10^{10}$	Diffusion coefficient m^2 s^{-1}	500
Minimum height column (m asl)	1000	Fall time threshold (s)	3600
Maximum height column (m asl)	5000	Lithic density (kg m^{-3})	2600
Minimum duration (hours)	1	Pumice density (kg m^{-3})	450
Maximum duration (hours)	2	Integration steps	100
		Alpha	1
		Beta	0.4
Grain Size Distribution			
Maximum grain size ϕ	-6		
Minimum grain size ϕ	6		
Maximum median phi ϕ	-3.3		
Minimum median phi ϕ	0		
Maximum standard deviation ϕ	2.5		
Minimum standard deviation ϕ	1.5		
Maximum aggregation	0.5		
Minimum aggregation	0.1		
Maximum aggregation diameter	4		

Table of the input parameters required, and ones used, to generate dispersal maps via the programme TephraProb.

References

- Alvarado, G.E. and Schmincke, H.U., 2013. The 1723 AD violent strombolian and phreatomagmatic eruption at Irazú Volcano, Costa Rica. *Revista Geológica de América Central*, (48), pp.41-61.
- Ammon, K., Dunai, T.J., Stuart, F.M., Meriaux, A.S. and Gayer, E., 2009. Cosmogenic 3He exposure ages and geochemistry of basalts from Ascension Island, Atlantic Ocean. *Quaternary Geochronology*, *4*(6), pp.525-532.
- Andronico, D. and Lodato, L., 2005. Effusive activity at Mount Etna volcano (Italy) during the 20th century: A contribution to volcanic hazard assessment. *Natural Hazards*, *36*(3), pp.407-443.
- Arzilli, F., La Spina, G., Burton, M.R., Polacci, M., Le Gall, N., Hartley, M.E., Di Genova, D., Cai, B., Vo, N.T., Bamber, E.C. and Nonni, S., 2019. Magma fragmentation in highly explosive basaltic eruptions induced by rapid crystallization. *Nature Geoscience*, *12*(12), pp.1023-1028.
- Atkins, F.B., Baker, P.E., Bell, J.D. and Smith, D.G.W., 1964. Oxford expedition to Ascension Island, 1964. *Nature*, *204*(4960), pp.722-724.
- Barberi, F., Cioni, R., Rosi, M., Santacroce, R., Sbrana, A. and Vecci, R., 1989. Magmatic and phreatomagmatic phases in explosive eruptions of Vesuvius as deduced by grain-size and component analysis of the pyroclastic deposits. *Journal of Volcanology and Geothermal Research*, *38*(3-4), pp.287-307.
- Bertagnini, A., Landi, P., Santacroce, R. and Sbrana, A., 1991. The 1906 eruption of Vesuvius: from magmatic to phreatomagmatic activity through the flashing of a shallow depth hydrothermal system. *Bulletin of Volcanology*, *53*(7), pp.517-532.
- Biass, S., Bonadonna, C., Connor, L. and Connor, C., 2016. TephraProb: a Matlab package for probabilistic hazard assessments of tephra fallout. *Journal of Applied Volcanology*, *5*(1), p.10.
- Biass, S., Todde, A., Cioni, R., Pistolesi, M., Geshi, N. and Bonadonna, C., 2017. Potential impacts of tephra fallout from a large-scale explosive eruption at Sakurajima volcano, Japan. *Bulletin of Volcanology*, *79*(10), p.73.
- Blackburn, E.A., Wilson, L. and Sparks, R.J., 1976. Mechanisms and dynamics of strombolian activity. *Journal of the Geological Society*, *132*(4), pp.429-440.
- Blake, S., 1984. Volatile oversaturation during the evolution of silicic magma chambers as an eruption trigger. *Journal of Geophysical Research: Solid Earth*, *89*(B10), pp.8237-8244.
- Bonadonna, C., Cioni, R., Pistolesi, M., Connor, C., Scollo, S., Pioli, L. and Rosi, M., 2013. Determination of the largest clast sizes of tephra deposits for the characterization of explosive eruptions: a study of the IAVCEI commission on tephra hazard modelling. *Bulletin of volcanology*, *75*(1), p.680.
- Booth, B., and Croasdale, R., Walker, G.P.L., 1978. A quantitative study of five thousand years of volcanism on Sao Miguel, Azores. *Philosophical Transactions of the Royal Society of London. Series A, Mathematical and Physical Sciences*, *288*(1352), pp.271-319.
- Brozena, J.M., 1986. Temporal and spatial variability of seafloor spreading processes in the northern South Atlantic. *Journal of Geophysical Research: Solid Earth*, *91*(B1), pp.497-510.
- Burton, M., Allard, P., Muré, F. and La Spina, A., 2007. Magmatic gas composition reveals the source depth of slug-driven Strombolian explosive activity. *Science*, *317*(5835), pp.227-230.
- Carey, R.J., Houghton, B.F. and Thordarson, T., 2010. Tephra dispersal and eruption dynamics of wet and dry phases of the 1875 eruption of Askja Volcano, Iceland. *Bulletin of Volcanology*, *72*(3), pp.259-278.

- Cashman, K.V., and Mangan, M.T., 1994. Physical aspects of magmatic degassing II. Constraints on vesiculation processes form textural studies of eruptive products. *Rev. Mineral*, *30*, pp.447-478.
- Cashman, K.V. and Scheu, B., 2015. Magmatic fragmentation. In *The Encyclopedia of Volcanoes* (pp. 459-471). Academic Press.
- Cashman, K.V. and Sparks, R.S.J., 2013. How volcanoes work: A 25-year perspective. *GSA bulletin*, *125*(5-6), pp.664-690.
- Chamberlain, K.J., Barclay, J., Preece, K., Brown, R.J. and Davidson, J.P., 2016. Origin and evolution of silicic magmas at ocean islands: Perspectives from a zoned fall deposit on Ascension Island, South Atlantic. *Journal of Volcanology and Geothermal Research*, *327*, pp.349-360.
- Chamberlain, K.J., Barclay, J., Preece, K.J., Brown, R.J. and Davidson, J.P., 2019. Lower Crustal Heterogeneity and Fractional Crystallisation Control Evolution of Small Volume Magma Batches at Ocean Island Volcanoes (Ascension Island, South Atlantic). *Journal of Petrology, (in press)*.
- Colò, L., Ripepe, M., Baker, D.R. and Polacci, M., 2010. Magma vesiculation and infrasonic activity at Stromboli open conduit volcano. *Earth and Planetary Science Letters*, *292*(3-4), pp.274-280.
- Colombier, M., Mueller, S.B., Kueppers, U., Scheu, B., Delmelle, P., Cimarelli, C., Cronin, S.J., Brown, R.J., Tost, M. and Dingwell, D.B., 2019. Diversity of soluble salt concentrations on volcanic ash aggregates from a variety of eruption types and deposits. *Bulletin of Volcanology*, *81*(7), p.39.
- Connor, L., C. Connor, C. Bonadonna, L. Courtland, "Tephra2," http://vhub.org/contribtool/tephra2.
- Daly, R. (1925). The Geology of Ascension Island. *Proceedings of the American Academy of Arts and Sciences, 60*(1), pp 3-80.
- Del Carlo, P. and Pompilio, M., 2004. The relationship between volatile content and the eruptive style of basaltic magma: the Etna case. *Annals of Geophysics*, *47*(4).
- Dellino, P., De Astis, G., La Volpe, L., Mele, D. and Sulpizio, R., 2011. Quantitative hazard assessment of phreatomagmatic eruptions at Vulcano (Aeolian Islands, Southern Italy) as obtained by combining stratigraphy, event statistics and physical modelling. *Journal of Volcanology and Geothermal Research*, *201*(1-4), pp.364-384.
- Dellino, P., Isaia, R. and Orsi, G., 2001. Statistical analysis of textural data from complex pyroclastic sequences: implications for fragmentation processes of the Agnano-Monte Spina Tephra (4.1 ka), Phlegraean Fields, southern Italy. *Bulletin of Volcanology*, *63*(7), pp.443-461.
- Di Traglia, F., Cimarelli, C., De Rita, D. and Torrente, D.G., 2009. Changing eruptive styles in basaltic explosive volcanism: examples from Croscat complex scoria cone, Garrotxa Volcanic Field (NE Iberian Peninsula). *Journal of Volcanology and Geothermal Research*, *180*(2-4), pp.89-109.
- D'oriano, C., Bertagnini, A., Cioni, R. and Pompilio, M., 2014. Identifying recycled ash in basaltic eruptions. *Scientific reports*, *4*, p.5851.
- Eychenne, J. and Le Pennec, J.L., 2012. Sigmoidal particle density distribution in a subplinian scoria fall deposit. *Bulletin of volcanology*, *74*(10), pp.2243-2249.
- Faneros, G. and Arnold, F., 2003, September. Geomorphology of two seamounts offshore Ascension Island, South Atlantic Ocean. In *Oceans 2003. Celebrating the Past... Teaming Toward the Future (IEEE Cat. No. 03CH37492)* (Vol. 1, pp. 39-49). IEEE.
- Ginibre, C., Wörner, G. and Kronz, A., 2007. Crystal zoning as an archive for magma evolution. *Elements*, *3*(4), pp.261-266.
- Gonnermann, H.M. and Manga, M., 2007. The fluid mechanics inside a volcano. *Annual Review of Fluid Mechanics*, *39*, pp.321-356.

- Guilbaud, M.N., Siebe, C. and Agustín-Flores, J., 2009. Eruptive style of the young high-Mg basaltic-andesite Pelagatos scoria cone, southeast of México City. *Bulletin of volcanology*, *71*(8), p.859.
- Gurioli, L., Harris, A.J.L., Houghton, B.F., Polacci, M. and Ripepe, M., 2008. Textural and geophysical characterization of explosive basaltic activity at Villarrica volcano. *Journal of Geophysical Research: Solid Earth*, *113*(B8).
- Gutmann, J.T., 2002. Strombolian and effusive activity as precursors to phreatomagmatism: eruptive sequence at maars of the Pinacate volcanic field, Sonora, Mexico. *Journal of Volcanology and Geothermal Research*, *113*(1-2), pp.345-356.
- Harris, C., 1983. The petrology of lavas and associated plutonic inclusions of Ascension Island. *Journal of Petrology*, *24*(4), pp.424-470.
- Harris, C., Bell, J.D. and Atkins, F.B., 1982. Isotopic composition of lead and strontium in lavas and coarse-grained blocks from Ascension Island, South Atlantic. *Earth and Planetary Science Letters*, *60*(1), pp.79-85.
- Head III, J.W. and Wilson, L., 1989. Basaltic pyroclastic eruptions: influence of gas-release patterns and volume fluxes on fountain structure, and the formation of cinder cones, spatter cones, rootless flows, lava ponds and lava flows. *Journal of Volcanology and Geothermal Research*, *37*(3-4), pp.261-271.
- Heiken, G., 1972. Morphology and petrography of volcanic ashes. *Geological Society of America Bulletin*, *83*(7), pp.1961-1988.
- Heiken, G., 1978. Characteristics of tephra from cinder cone, Lassen volcanic national park, California. *Bulletin Volcanologique*, *41*(2), pp.119-130.
- Heiken, G., and Wohletz, K., 1992. Volcanic Ash. *University of California Press.*
- Hobson, K.E., 2001. The Pyroclastic Deposits and Eruption History of Ascension Island: A Palaeomagnetic and Volcanological Study (Doctoral dissertation) University of Oxford.
- Houghton, B. and Carey, R.J., 2015. Pyroclastic fall deposits. In *The Encyclopedia of Volcanoes* (pp. 599-616). Academic Press.
- Houghton, B.F. and Gonnermann, H.M., 2008. Basaltic explosive volcanism: constraints from deposits and models. *Chemie der Erde-Geochemistry*, *68*(2), pp.117-140.
- Houghton, B.F. and Hackett, W.R., 1984. Strombolian and phreatomagmatic deposits of Ohakune Craters, Ruapehu, New Zealand: a complex interaction between external water and rising basaltic magma. *Journal of volcanology and geothermal research*, *21*(3-4), pp.207-231.
- Houghton, B.F., Latter, J.H. and Hackett, W.R., 1987. Volcanic hazard assessment for Ruapehu composite volcano, Taupo volcanic zone, New Zealand. *Bulletin of volcanology*, *49*(6), pp.737-751.
- Houghton, B.F. and Schmincke, H.U., 1986. Mixed deposits of simultaneous strombolian and phreatomagmatic volcanism: Rothenberg volcano, east Eifel volcanic field. *Journal of Volcanology and Geothermal Research*, *30*(1-2), pp.117-130.
- Houghton, B.F. and Schmincke, H.U., 1989. Rothenberg scoria cone, East Eifel: a complex Strombolian and phreatomagmatic volcano. *Bulletin of Volcanology*, *52*(1), pp.28-48.
- Houghton, B.F., Taddeucci, J., Andronico, D., Gonnermann, H.M., Pistolesi, M., Patrick, M.R., Orr, T.R., Swanson, D.A., Edmonds, M., Gaudin, D. and Carey, R.J., 2016. Stronger or longer: Discriminating between Hawaiian and Strombolian eruption styles. *Geology*, *44*(2), pp.163-166.
- Houghton, B., White, J.D. and Van Eaton, A.R., 2015. Phreatomagmatic and related eruption styles. In *The Encyclopedia of Volcanoes* (pp. 537-552). Academic Press.
- Houghton, B.F. and Wilson, C.J.N., 1989. A vesicularity index for pyroclastic deposits. *Bulletin of volcanology*, *51*(6), pp.451-462.

- Houghton, B.F., Wilson, C.J.N., Del Carlo, P., Coltelli, M., Sable, J.E. and Carey, R., 2004. The influence of conduit processes on changes in style of basaltic Plinian eruptions: Tarawera 1886 and Etna 122 BC. *Journal of Volcanology and Geothermal Research*, *137*(1-3), pp.1-14.
- Houghton, B.F., Wilson, C.J.N. and Smith, I.E.M., 1999. Shallow-seated controls on styles of explosive basaltic volcanism: a case study from New Zealand. *Journal of Volcanology and Geothermal Research*, *91*(1), pp.97-120.
- Inman D.L., 1952. Measures for describing the size distributions of sediments. *Journal of Sedimentary Research*, 22(3). pp 125-145.
- Jenkins, S.F., Wilson, T.M. and Magill, C., 2015. Volcanic ash fall hazard and risk. In *Global Volcanic Hazards and Risk* (pp 173-222). Cambridge University Press.
- Jicha, B.R., Singer, B.S. and Valentine, M.J., 2013. 40Ar/39Ar geochronology of subaerial Ascension Island and a re-evaluation of the temporal progression of basaltic to rhyolitic volcanism. *Journal of Petrology*, *54*(12), pp.2581-2596.
- Jutzeler, M., White, J.D., Proussevitch, A.A. and Gordee, S.M., 2016. Vesiculation and fragmentation history in a submarine scoria cone-forming eruption, an example from Nishiizu (Izu Peninsula, Japan). *Bulletin of Volcanology*, *78*(2), p.7.
- Kar, A., 1997. A comprehensive geological, geochemical, and petrogenetic study of hotspot related oceanic basalt-rhyolite series rocks from Ascension Island, South Atlantic Ocean (Doctoral dissertation) University of Oklahoma.
- Kar, A., Weaver, B., Davidson, J. and Colucci, M., 1998. Origin of differentiated volcanic and plutonic rocks from Ascension Island, South Atlantic Ocean. *Journal of Petrology*, *39*(5), pp.1009-1024.
- Kervyn, M., Ernst, G.G.J., Carracedo, J.C. and Jacobs, P., 2012. Geomorphometric variability of “monogenetic” volcanic cones: evidence from Mauna Kea, Lanzarote and experimental cones. *Geomorphology*, *136*(1), pp.59-75.
- Klingelhöfer, F., Minshull, T.A., Blackman, D.K., Harben, P. and Childers, V., 2001. Crustal structure of Ascension Island from wide-angle seismic data: implications for the formation of near-ridge volcanic islands. *Earth and Planetary Science Letters*, *190*(1-2), pp.41-56.
- Kósik, S., Németh, K., Kereszturi, G., Procter, J.N., Zellmer, G.F. and Geshi, N., 2016. Phreatomagmatic and water-influenced Strombolian eruptions of a small-volume parasitic cone complex on the southern ringplain of Mt. Ruapehu, New Zealand: facies architecture and eruption mechanisms of the Ohakune Volcanic Complex controlled by an unstable fissure eruption. *Journal of Volcanology and Geothermal Research*, *327*, pp.99-115.
- Lautze, N.C. and Houghton, B.F., 2005. Physical mingling of magma and complex eruption dynamics in the shallow conduit at Stromboli volcano, Italy. *Geology*, *33*(5), pp.425-428.
- Lautze, N.C. and Houghton, B.F., 2007. Linking variable explosion style and magma textures during 2002 at Stromboli volcano, Italy. *Bulletin of Volcanology*, *69*(4), pp.445-460.
- Liu, E.J., Cashman, K.V., Rust, A.C. and Höskuldsson, A., 2017. Contrasting mechanisms of magma fragmentation during coeval magmatic and hydromagmatic activity: the Hverfjall Fires fissure eruption, Iceland. *Bulletin of Volcanology*, *79*(10), p.68.
- Lorenz, V., 1987. Phreatomagmatism and its relevance. *Chemical Geology*, *62*(1-2), pp.149-156.
- Magill, C.R., Hurst, A.W., Hunter, L.J. and Blong, R.J., 2006. Probabilistic tephra fall simulation for the Auckland Region, New Zealand. *Journal of volcanology and geothermal research*, *153*(3-4), pp.370-386.

- Mangan, M.T. and Cashman, K.V., 1996. The structure of basaltic scoria and reticulite and inferences for vesiculation, foam formation, and fragmentation in lava fountains. *Journal of Volcanology and Geothermal Research*, *73*(1-2), pp.1-18.
- Mangan, M.T., Cashman, K.V. and Swanson, D.A., 2014. The dynamics of Hawaiian-style eruptions: a century of study. *Characteristics of Hawaiian volcanoes. US Geological Survey*, pp.323-354.
- Mattsson, H.B., 2012. Rapid magma ascent and short eruption durations in the Lake Natron–Engaruka monogenetic volcanic field (Tanzania): a case study of the olivine melilititic Pello Hill scoria cone. *Journal of Volcanology and Geothermal Research*, *247*, pp.16-25.
- Melnik, O., Barmin, A.A., Sparks, R.S.J., 2005. Dynamics of magma flow inside volcanic conduits with bubble over- pressure buildup and gas loss through permeable magma. *Journal of Volcanology and Geothermal Research,* 143, pp. 53–68.
- Metrich, N., Bertagnini, A., Landi, P., Rosi, M., 2001. Crystal- lization driven by decompression and water loss at Stromboli volcano (Aeolian Islands, Italy). *Journal of Perology,* 42, pp. 1471–1490.
- Minshull, T.A., Ishizuka, O. and Garcia-Castellanos, D., 2010. Long-term growth and subsidence of Ascension Island: Constraints on the rheology of young oceanic lithosphere. *Geophysical Research Letters*, *37*(23).
- Moritra, P., Gonnermann, H.M., Houghton, B.F., Giachetti, T., 2013. Relating vesicles shapes in pyroclasts to eruption styles. *Bulletin of Volcanology*. 75 (2), 691.
- Moitra, P., Gonnermann, H.M., Houghton, B.F. and Tiwary, C.S., 2018. Fragmentation and Plinian eruption of crystallizing basaltic magma. *Earth and Planetary Science Letters*, *500*, pp.97-104.
- Mueller, S.B., Ayris, P.M., Wadsworth, F.B., Kueppers, U., Casas, A.S., Delmelle, P., Taddeucci, J., Jacob, M. and Dingwell, D.B., 2017. Ash aggregation enhanced by deposition and redistribution of salt on the surface of volcanic ash in eruption plumes. *Scientific reports*, *7*, p.45762.
- Mueller, S.B., Houghton, B.F., Swanson, D.A., Fagents, S.A. and Klawonn, M., 2018. Intricate episodic growth of a Hawaiian tephra deposit: case study of the 1959 Kīlauea Iki eruption. *Bulletin of Volcanology*, *80*(10), p.73.
- Mueller, S.B., Kueppers, U., Ayris, P.M., Jacob, M. and Dingwell, D.B., 2016. Experimental volcanic ash aggregation: Internal structuring of accretionary lapilli and the role of liquid bonding. *Earth and Planetary Science Letters*, *433*, pp.232-240.
- Namiki, A. and Manga, M., 2008. Transition between fragmentation and permeable outgassing of low viscosity magmas. *Journal of Volcanology and Geothermal Research*, *169*(1-2), pp.48-60.
- Németh, K. and Kereszturi, G., 2015. Monogenetic volcanism: personal views and discussion. *International Journal of Earth Sciences*, *104*(8), pp.2131-2146.
- Németh, K., Risso, C., Nullo, F. and Kereszturi, G., 2011. The role of collapsing and cone rafting on eruption style changes and final cone morphology: Los Morados scoria cone, Mendoza, Argentina. *Central European Journal of Geosciences*, *3*(2), pp.102-118.
- Nielson, D.L. and Sibbett, B.S., 1996. Geology of Ascension Island, South Atlantic Ocean. *Geothermics*, *25*(4-5), pp.427-448.
- Nielson, D.L. and Stiger, S.G., 1996. Drilling and evaluation of Ascension# 1, a geothermal exploration well on Ascension Island, South Atlantic Ocean. *Geothermics*, *25*(4-5), pp.543-560.
- Parcheta, C.E., Houghton, B.F. and Swanson, D.A., 2013. Contrasting patterns of vesiculation in low, intermediate, and high Hawaiian fountains: a case study of the 1969 Mauna Ulu eruption. *Journal of Volcanology and Geothermal Research*, *255*, pp.79-89.

- Pardo, N., Cronin, S.J., Németh, K., Brenna, M., Schipper, C.I., Breard, E., White, J.D., Procter, J., Stewart, B., Agustín-Flores, J. and Moebis, A., 2014. Perils in distinguishing phreatic from phreatomagmatic ash; insights into the eruption mechanisms of the 6 August 2012 Mt. Tongariro eruption, New Zealand. *Journal of Volcanology and Geothermal Research*, *286*, pp.397-414.
- Parfitt, E.A., 2004. A discussion of the mechanisms of explosive basaltic eruptions. *Journal of Volcanology and Geothermal Research*, *134*(1-2), pp.77-107.
- Parfitt, E.A. and Wilson, L., 1995. Explosive volcanic eruptions—IX. The transition between Hawaiian-style lava fountaining and Strombolian explosive activity. *Geophysical Journal International*, *121*(1), pp.226-232.
- Parfitt, E.A. and Wilson, L., 1999. A Plinian treatment of fallout from Hawaiian lava fountains. *Journal of Volcanology and Geothermal Research*, *88*(1-2), pp.67-75.
- Parfitt, E.A., Wilson, L. and Head, J.W., III, 1993. Basaltic magma reservoirs: factors controlling their rupture characteristics and evolution. *Journal of Volcanology Geothermal Research*, 55, pp. 1-14.
- Pioli, L., Erlund, E., Johnson, E., Cashman, K., Wallace, P., Rosi, M. and Granados, H.D., 2008. Explosive dynamics of violent Strombolian eruptions: the eruption of Parícutin Volcano 1943–1952 (Mexico). *Earth and Planetary Science Letters*, *271*(1-4), pp.359-368.
- Polacci, M., Baker, D.R., Bai, L. and Mancini, L., 2008. Large vesicles record pathways of degassing at basaltic volcanoes. *Bulletin of Volcanology*, *70*(9), pp.1023-1029.
- Polacci, M., Baker, D.R., Mancini, L., Favretto, S. and Hill, R.J., 2009. Vesiculation in magmas from Stromboli and implications for normal Strombolian activity and paroxysmal explosions in basaltic systems. *Journal of Geophysical Research: Solid Earth*, *114*(B1).
- Polacci, M., Corsaro, R.A. and Andronico, D., 2006. Coupled textural and compositional characterization of basaltic scoria: Insights into the transition from Strombolian to fire fountain activity at Mount Etna, Italy. *Geology*, *34*(3), pp.201-204.
- Preece, K., Mark, D.F., Barclay, J., Cohen, B.E., Chamberlain, K.J., Jowitt, C., Vye-Brown, C., Brown, R.J. and Hamilton, S., 2018. Bridging the gap: 40Ar/39Ar dating of volcanic eruptions from the 'Age of Discovery'. *Geology*, *46*(12), pp.1035-1038.
- Pyle, D.M., 1989. The thickness, volume and grainsize of tephra fall deposits. *Bulletin of Volcanology*, 51(1). pp 1-15.
- Pyle, D.M., 2015. Sizes of volcanic eruptions. In *The encyclopedia of volcanoes* (pp. 257-264). Academic Press.
- Riggs, N.R. and Duffield, W.A., 2008. Record of complex scoria cone eruptive activity at Red Mountain, Arizona, USA, and implications for monogenetic mafic volcanoes. *Journal of Volcanology and Geothermal Research*, *178*(4), pp.763-776.
- Risso, C., Németh, K., Combina, A.M., Nullo, F. and Drosina, M., 2008. The role of phreatomagmatism in a Plio-Pleistocene high-density scoria cone field: Llancanelo Volcanic Field (Mendoza), Argentina. *Journal of Volcanology and Geothermal Research*, *169*(1-2), pp.61-86.
- Romero, J.E., Vera, F., Polacci, M., Morgavi, D., Arzilli, F., Alam, M.A., Bustillos, J.E., Guevara, A., Johnson, J.B., Palma, J.L. and Burton, M., 2018. Tephra from the 3 March 2015 sustained column related to explosive lava fountain activity at Volcán Villarrica (Chile). *Frontiers in Earth Science*, *6*, p.98.
- Ross, P.S. and White, J.D., 2012. Quantification of vesicle characteristics in some diatreme-filling deposits, and the explosivity levels of magma–water interactions within diatremes. *Journal of Volcanology and Geothermal Research*, *245*, pp.55-67.
- Sable, J.E., Houghton, B.F., Del Carlo, P., Coltelli, M., 2006. Changing conditions of magma ascent and fragmentation during the Etna 122 BC basaltic Plinian eruption:

evidence from clast microtextures. *Journal of Volcanology and Geothermal Research.* 158, pp. 333–354.

- Sánchez, M.C., Sarrionandia, F., Arostegui, J. and Ibarguchi, J.G., 2015. Silicate glass micro and nanospherules generated in explosive eruptions of ultrabasic magmas: implications for the origin of pelletal lapilli. *Journal of Volcanology and Geothermal Research*, *293*, pp.13-24.
- Schilling, J.G., Thompson, G., Kingsley, R. and Humphris, S., 1985. Hotspot—migrating ridge interaction in the South Atlantic. *Nature*, *313*(5999), p.187.
- Schmith, J., Höskuldsson, Á. and Holm, P.M., 2017. Grain shape of basaltic ash populations: implications for fragmentation. *Bulletin of Volcanology*, *79*(2), p.14
- Shea, T., Houghton, B.F., Gurioli, L., Cashman, K.V., Hammer, J.E. and Hobden, B.J., 2010. Textural studies of vesicles in volcanic rocks: an integrated methodology. *Journal of Volcanology and Geothermal Research*, *190*(3-4), pp.271-289.
- Shea, T., Gurioli, L., Houghton, B.F., Cioni, R. and Cashman, K.V., 2011. Column collapse and generation of pyroclastic density currents during the AD 79 eruption of Vesuvius: the role of pyroclast density. *Geology*, *39*(7), pp.695-698.
- Shea T., 2016. *FOAMS textural analysis software*. Shea T., viewed 29 May 2020, *http://www.soest.hawaii.edu/GG/FACULTY/tshea/foams/downloads.html*
- Sheridan, M.F. and Wohletz, K.H., 1983. Hydrovolcanism: basic considerations and review. *Journal of Volcanology and Geothermal Research*, *17*(1-4), pp.1-29.
- Simkin, T., Siebert, L., McClelland, L., Bridge, D., Newhall, C. and Latter, J.H., 1981. *Volcanoes of the world: a regional directory, gazetteer, and chronology of volcanism during the last 10,000 years*. US Hutchinson Ross Publishing.
- Sparks, R.S.J., 1978. The dynamics of bubble formation and growth in magmas: a review and analysis. *Journal of Volcanology and Geothermal Research*, *3*(1-2), pp.1-37.
- Sparks, R.S.J. and Pinkerton, H., 1978. Effect of degassing on rheology of basaltic lava. *Nature*, *276*, pp.385-386.
- Stevens, N.F., Wadge, G. and Murray, J.B., 1999. Lava flow volume and morphology from digitised contour maps: a case study at Mount Etna, Sicily. *Geomorphology*, *28*(3-4), pp.251-261.
- Stovall, W.K., Houghton, B.F., Gonnermann, H., Fagents, S.A. and Swanson, D.A., 2011. Eruption dynamics of Hawaiian-style fountains: the case study of episode 1 of the Kīlauea Iki 1959 eruption. *Bulletin of Volcanology*, *73*(5), pp.511-529.
- Stovall, W.K., Houghton, B.F., Hammer, J.E., Fagents, S.A. and Swanson, D.A., 2012. Vesiculation of high fountaining Hawaiian eruptions: episodes 15 and 16 of 1959 Kīlauea Iki. *Bulletin of volcanology*, *74*(2), pp.441-455.
- Sumner, J.M., 1998. Formation of clastogenic lava flows during fissure eruption and scoria cone collapse: the 1986 eruption of Izu-Oshima Volcano, eastern Japan. *Bulletin of Volcanology*, *60*(3), pp.195-212.
- SutawIdjaja, I.S. and Sukhyar, R., 2009. Cinder cones of Mount Slamet, Central Java, Indonesia. *Indonesian Journal on Geoscience*, *4*(1), pp.57-75.
- Swanson, D.A. and Houghton, B.F., 2018. Products, processes, and implications of Keanakāko ʻi volcanism, Kīlauea Volcano, Hawai ʻi. *Field Volcanology: A Tribute to the Distinguished Career of Don Swanson: Geological Society of America Special Paper*, *538*, pp.159-190.
- Taddeucci, J., Edmonds, M., Houghton, B., James, M.R. and Vergniolle, S., 2015. Hawaiian and Strombolian eruptions. In *The encyclopedia of volcanoes* (pp. 485-503). Academic Press.
- Taddeucci, J., Pompilio, M. and Scarlato, P., 2004. Conduit processes during the July–August 2001 explosive activity of Mt. Etna (Italy): inferences from glass chemistry and

crystal size distribution of ash particles. *Journal of Volcanology and Geothermal Research*, *137*(1-3), pp.33-54.

- Valentine, G.A., Krier, D., Perry, F.V. and Heiken, G., 2005. Scoria cone construction mechanisms, Lathrop Wells volcano, southern Nevada, USA. *Geology*, *33*(8), pp.629-632.
- Vergniolle, S. and Jaupart, C., 1986. Separated two-phase flow and basaltic eruptions. *Journal of Geophysical Research: Solid Earth*, *91*(B12), pp.12842-12860.
- Walker, G.P., 1973. Explosive volcanic eruptions—a new classification scheme. *Geologische Rundschau*, *62*(2), pp.431-446.
- Walker, G.P., Croasdale, R., 1972. Characteristics of some basaltic pyroclasts*. Bulletin of Volcanology*, 35(2). pp 303-317.
- Wardman, J.B., Wilson, T.M., Bodger, P.S., Cole, J.W. and Johnston, D.M., 2012. Investigating the electrical conductivity of volcanic ash and its effect on HV power systems. *Physics and Chemistry of the Earth, Parts A/B/C*, *45*, pp.128-145.
- Weaver, B.L., 1991. The origin of ocean island basalt end-member compositions: trace element and isotopic constraints. *Earth and Planetary Science Letters*, *104*(2-4), pp.381-397.
- Weaver, B., Kar, A., Davidson, J. and Colucci, M., 1996. Geochemical characteristics of volcanic rocks from Ascension Island, south Atlantic Ocean. *Geothermics*, *25*(4-5), pp.449-470.
- Weaver, B.L., Wood, D.A., Tarney, J. and Joron, J.L., 1987. Geochemistry of ocean island basalts from the south Atlantic: Ascension, Bouvet, St. Helena, Gough and Tristan da Cunha. *Geological Society, London, Special Publications*, *30*(1), pp.253-267.
- Webster, J.D. and Rebbert, C.R., 2001. The geochemical signature of fluid-saturated magma determined from silicate melt inclusions in Ascension Island granite xenoliths. *Geochimica et Cosmochimica Acta*, *65*(1), pp.123-136.
- Wilkinson, D. (2003). The parable of Green Mountain: Ascension Island, ecosystem construction and ecological fitting. *Journal of Biogeography*, 31(1), pp.1-4.
- Wohletz, K.H., 1986. Explosive magma-water interactions: Thermodynamics, explosion mechanisms, and field studies. *Bulletin of Volcanology*, *48*(5), pp.245-264.
- Woods, A., Cardoso, S., 1997. Triggering basaltic volcanic eruptions by bubble-melt separation. *Nature* 385**,** pp. 518–520.
- Xia, F., Brugger, J., Chen, G., Ngothai, Y., O'Neil, B, Putnis, A. and Pring, A., 2009. Mechanism and kinetics of pseudomorphic mineral replacement reactions: A case study of the replacement of pentlandite by violarite. *Geochimica et Cosmochimica Acta, 73(7), p.1945.*
- Zimanowski, B., Büttner, R., Lorenz, V. and Häfele, H.G., 1997. Fragmentation of basaltic melt in the course of explosive volcanism. *Journal of Geophysical Research: Solid Earth*, *102*(B1), pp.803-814.